LOAN DOCUMENT

PHOTOGRAPH THIS SHEET

LEVEL

INVENTORY

DTIC ACCESSION NUMBER

AFRL-ML-TY-TR-2002-4517

DOCUMENT IDENTIFICATION

MAR 2002

DISTRIBUTION STATEMENT A
Approved for Public Release
Distribution Unlimited

DISTRIBUTION STATEMENT

HANDLE WITH CARE

ACCESSION FOR
NTIS GRA&I ☑
DTIC TRAC ☐
UNANNOUNCED ☐
JUSTIFICATION

BY

DISTRIBUTION/

AVAILABILITY CODES

DISTRIBUTION	AVAILABILITY AND/OR SPECIAL	
A-1		

DISTRIBUTION STAMP

DATE ACCESSIONED

DATE RETURNED

20020325 086

DATE RECEIVED IN DTIC

REGISTERED OR CERTIFIED NUMBER

PHOTOGRAPH THIS SHEET AND RETURN TO DTIC-FDAC

DTIC FORM 70A JUN 90

DOCUMENT PROCESSING SHEET

PREVIOUS EDITIONS MAY BE USED UNTIL STOCK IS EXHAUSTED.

LOAN DOCUMENT

AFRL-ML-TY-TR-2002-4517

Negative Ion Sensors for Real-Time Downhole DNAPLs Detection

Gregory D. Gillispie

Dakota Technologies, Inc.
2201-A 12th Street N.
Fargo, ND 58102

AIR FORCE RESEARCH LABORATORY
MATERIALS & MANUFACTURING DIRECTORATE
AIR EXPEDITIONARY FORCES TECHNOLOGIES DIVISION
139 BARNES DRIVE, STE 2
TYNDALL AFB FL 32403-5323

NOTICES

USING GOVERNMENT DRAWINGS, SPECIFICATIONS, OR OTHER DATA INCLUDED IN THIS DOCUMENT FOR ANY PURPOSE OTHER THAN GOVERNMENT PROCUREMENT DOES NOT IN ANY WAY OBLIGATE THE US GOVERNMENT. THE FACT THAT THE GOVERNMENT FORMULATED OR SUPPLIED THE DRAWINGS, SPECIFICATIONS, OR OTHER DATA DOES NOT LICENSE THE HOLDER OR ANY OTHER PERSON OR CORPORATION; OR CONVEY ANY RIGHTS OR PERMISSION TO MANUFACTURE, USE, OR SELL ANY PATENTED INVENTION THAT MAY RELATE TO THEM.

THIS REPORT IS RELEASABLE TO THE NATIONAL TECHNICAL INFORMATION SERVICE
5285 PORT ROYAL RD.
SPRINGFIELD VA 22 161
TELEPHONE 703 487 4650; 703 4874639 (TDD for the hearing-impaired)
E-MAIL orders@ntis.fedworld.gov
WWW http://www.ntis.gov/index.html

AT NTIS, IT WILL BE AVAILABLE TO THE GENERAL PUBLIC, INCLUDING FOREIGN NATIONS.

THIS TECHNICAL REPORT HAS BEEN REVIEWED AND IS APPROVED FOR PUBLICATION.

MICHAEL J. CALIDONNA, Capt, USAF
Program Manager

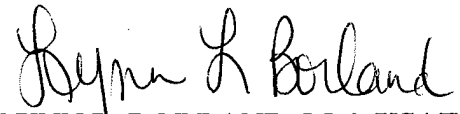

LYNN L. BORLAND, Maj, USAF, BSC
Chief, Weapons Systems Logistics Branch

DONALD R. HUCKLE, JR., Colonel, USAF
Chief, Air Expeditionary Forces Technologies Division

Do not return copies of this report unless contractual obligations or notice on a specific document requires its return.

REPORT DOCUMENTATION PAGE

Form Approved
OMB No. 0704-0188

1. AGENCY USE ONLY *(Leave blank)*	2. REPORT DATE	3. REPORT TYPE AND DATES COVERED
	March 2002	Final Report 12 May 1998 - 11 May 2001

4. TITLE AND SUBTITLE
Negative Ion Sensor for Real-Time Downhole DNAPLs Detection

5. FUNDING NUMBERS
PE - 63716D
C - F08637-98-C-6009
JON - 3904B88B

6. AUTHOR(S)
Gregory D. Gillispie

7. PERFORMING ORGANIZATION NAME(S) AND ADDRESS(ES)
Dakota Technologies, Inc.
2201-A 12th Street N
Fargo, ND 58102-1803

8. PERFORMING ORGANIZATION REPORT NUMBER

9. SPONSORING/MONITORING AGENCY NAME(S) AND ADDRESS(ES)
Air Force Research Laboratory
Air Expeditionary Forces Technologies Division (AFRL/MLQ)
139 Barnes Drive, Suite 2
Tyndall AFB FL 32403-5323

10. SPONSORING/MONITORING AGENCY REPORT NUMBER
AFRL-ML-TY-TR-2002-4517

11. SUPPLEMENTARY NOTES

12a. DISTRIBUTION AVAILABILITY STATEMENT
Distribution Unlimited; Approved for Public Release

12b. DISTRIBUTION CODE
A

13. ABSTRACT *(Maximum 200 words)*

This final report summarizes the findings of a three-year R&D project aimed at improved methodology for locating chlorinated solvent contamination in the subsurface. Current subsurface sampling methods (soil cores, split spoon) provide widely spaced data points for economic considerations and may be less than accurate because of the volatility of some species. Direct detection of subsurface contamination alleviates many of these negative factors, but itself brings additional difficulties such as contending with the water table. Direct push technology offers a promising alternative to the conventional approaches and has proven very useful in characterizing subsurface hydrocarbon contamination using laser induced fluorescence technology. The effort reported here employs a patented Membrane Interface Probe (MIP) to allow mass transfer across the MIP from the soil matrix to a carrier gas internal to the cone penetrometer. Placing the detector downhole allows immediate detection of the volatile compound requiring only the electrical signal to be transferred to the surface. During this effort three technologies were demonstrated for subsurface detection, a halogen specific detector (XSD), a photoionization detector (PID), and a photoemissive electron capture detector (PE-ECD). Each was demonstrated at known contaminated sites with favorable results.

14. SUBJECT TERMS
DNAPL, Sensor, ionization, cone penetrometry, electron capture detector, halogen

15. NUMBER OF PAGES
104

16. PRICE CODE

17. SECURITY CLASSIFICATION OF REPORT	18. SECURITY CLASSIFICATION OF THIS PAGE	19. SECURITY CLASSIFICATION OF ABSTRACT	20. LIMITATION OF ABSTRACT
UNCLASS	UNCLASS	UNCLASS	UL

GENERAL INSTRUCTIONS FOR COMPLETING SF 298

The Report Documentation Page (RDP) is used in announcing and cataloging reports. It is important that this information be consistent with the rest of the report, particularly the cover and title page. Instructions for filling in each block of the form follow. It is important to ***stay within the lines*** to meet ***optical scanning requirements.***

Block 1. Agency Use Only *(Leave blank)*.

Block 2. Report Date. Full publication date including day, month, and year, if available (e.g. 1 Jan 88). Must cite at least the year.

Block 3. Type of Report and Dates Covered. State whether report is interim, final, etc. If applicable, enter inclusive report dates (e.g. 10 Jun 87 - 30 Jun 88).

Block 4. Title and Subtitle. A title is taken from the part of the report that provides the most meaningful and complete information. When a report is prepared in more than one volume, repeat the primary title, add volume number, and include subtitle for the specific volume. On classified documents enter the title classification in parentheses.

Block 5. Funding Numbers. To include contract and grant numbers; may include program element number(s), project number(s), task number(s), and work unit number(s). Use the following labels:

C - Contract	**PR** - Project
G - Grant	**TA** - Task
PE - Program Element	**WU** - Work Unit Accession No.

Block 6. Author(s). Name(s) of person(s) responsible for writing the report, performing the research, or credited with the content of the report. If editor or compiler, this should follow the name(s).

Block 7. Performing Organization Name(s) and Address(es). Self-explanatory.

Block 8. Performing Organization Report Number. Enter the unique alphanumeric report number(s) assigned by the organization performing the report.

Block 9. Sponsoring/Monitoring Agency Name(s) and Address(es). Self-explanatory.

Block 10. Sponsoring/Monitoring Agency Report Number. *(If known)*

Block 11. Supplementary Notes. Enter information not included elsewhere such as: Prepared in cooperation with....; Trans. of....; To be published in.... When a report is revised, include a statement whether the new report supersedes or supplements the older report.

Block 12a. Distribution/Availability Statement. Denotes public availability or limitations. Cite any availability to the public. Enter additional limitations or special markings in all capitals (e.g. NOFORN, REL, ITAR).

- **DOD** - See DoDD 5230.24, "Distribution Statements on Technical Documents."
- **DOE** - See authorities.
- **NASA** - See Handbook NHB 2200.2.
- **NTIS** - Leave blank.

Block 12b. Distribution Code.

- **DOD** - Leave blank.
- **DOE** - Enter DOE distribution categories from the Standard Distribution for Unclassified Scientific and Technical Reports.
- **NASA** - Leave blank.
- **NTIS** - Leave blank.

Block 13. Abstract. Include a brief *(Maximum 200 words)* factual summary of the most significant information contained in the report.

Block 14. Subject Terms. Keywords or phrases identifying major subjects in the report.

Block 15. Number of Pages. Enter the total number of pages.

Block 16. Price Code. Enter appropriate price code *(NTIS only)*.

Blocks 17. - 19. Security Classifications. Self-explanatory. Enter U.S. Security Classification in accordance with U.S. Security Regulations (i.e., UNCLASSIFIED). If form contains classified information, stamp classification on the top and bottom of the page.

Block 20. Limitation of Abstract. This block must be completed to assign a limitation to the abstract. Enter either UL (unlimited) or SAR (same as report). An entry in this block is necessary if the abstract is to be limited. If blank, the abstract is assumed to be unlimited.

TABLE OF CONTENTS

LIST OF FIGURES

LIST OF TABLES

INTRODUCTION AND BACKGROUND

This final report summarizes the findings of a three-year R&D project aimed at improved methodology for locating chlorinated solvent contamination in the subsurface. Chlorinated solvents, such as trichloroethylene and perchloroethylene, tend to exist in the environment as dense non-aqueous phase liquids (DNAPLs). Unlike petroleum hydrocarbons, which are generally less dense than water, chlorinated solvent DNAPLs sink as they travel through the vadose zone and capillary fringe into the groundwater. In the process, they leave behind a trail of micro-globules in the soil matrix [Schwille (1988), Pankow and Cherry (1996)]. The heterogeneously distributed "free-product" phase can continue to contaminate large volumes of groundwater for decades to centuries (Feenstra et al., 1996).

The three-dimensional model of subsurface DNAPLs distribution provided by traditional drilling, discrete sampling, and laboratory analysis is often inadequate. For economic reasons, soil cores must be sampled at widely separated intervals (several feet is typical), which sometimes forces arbitrary decisions on which portion of the soil core is to be subsampled. Relatively volatile chlorinated substances can easily be lost during the subsampling process [Hewitt et al., 1995]. Split spoon samples collected below the water table are often poorly retained, owing to the flow of unconsolidated sands and silty soils. The strategy for locating DNAPLs source terms by the trial-and-error placement of monitoring wells is also notoriously inefficient. Direct detection of residual or free-phase DNAPL in groundwater can be maddeningly rare (Feenstra et al., 1996), even at intensely investigated DNAPL sites, where high dissolved phase concentrations strongly suggest DNAPLs are present. In principle, non-invasive geophysical techniques could "image" DNAPLs from the ground surface (Pankow and Cherry, 1996). However, success to date has been minimal and the efficacy of such non-intrusive detection schemes likely drops sharply as a function of contaminant depth.

Injection of solvents and/or surfactants can dissolve and mobilize DNAPLs, thereby complementing other remediation technologies such as steam thermal enhanced venting, sparging/venting, and in-well aeration. Similarly, partitioning inter-well tracer tests (PITT) can estimate the total contaminant mass. Removal efficiencies greater than 90% using surfactants at relatively homogenous sites, such as Hill AFB, have been reported (J. Fountain, 1998). But injection/extraction methodology is expensive and depends on *a priori* knowledge for design of the well field. As Fountain cautions, "Adequate site characterization is critical for evaluating the applicability of any DNAPL remediation technology and characterization of the DNAPL distribution is essential for both remediation design and performance evaluation... the ultimate level of clean up may be governed more by the hydrogeology than the technology."

Direct-push technology offers a promising alternative to the conventional approaches based on soil borings and monitoring wells. Direct push refers to soil probes that are either pushed with heavy-cone penetrometer trucks or are percussion hammered into the ground. Although cone penetrometry has been used to characterize the mechanical properties of soil for several decades, the adaptation for environmental site characterization of chemical contamination goes back only a little more than ten years. Much of the work has been conducted under Department of Defense-sponsored programs, the most significant being the program leading to development of the Site Characterization Analysis and Penetrometer System (SCAPS). The SCAPS philosophy of minimally invasive methods represents a major success story for Strategic Environmental Research and Development Program (SERDP) and Environmental Security Technology Certification Program (ESTCP). For example, the SCAPS laser-induced fluorescence (LIF) technology, commercialized as the Rapid Optical Screening Tool (ROST), has been applied at hundreds of fuel-contaminated sites. The ROST collects LIF data through a sapphire window interface as a cone penetrometer is advanced at a standard rate of 2 cm/s. The LIF method works well for screening bulk fuels (diesel, jet, gasoline) and other petroleum hydrocarbons, which contain highly fluorescent aromatic species.

Unfortunately, chlorinated solvents are not intrinsically luminescent, although DNAPLs have been successfully detected via indirect fluorescence. The indirect fluorescence is due to petroleum hydrocarbons dissolved in chlorinated solvents during degreasing or other processes. However, current LIF methods cannot differentiate dissolved phase from residual or stained material, and the quantitative response is severely affected by soil matrix effects.

Many researchers have attempted to detect chlorinated species via Raman spectroscopy, an optical technique compatible with real-time measurements through a sapphire-window interface. The crucial question for Raman spectroscopy is whether it can achieve sufficient sensitivity to benefit from its specificity advantages. Nearly every possible variation on the basic Raman spectroscopy theme (except Fourier Transform Raman) has been promoted as suitable for downhole implementation, including different wavelength laser sources, new developments in charged coupled detectors, surface or resonance enhancement techniques, time-resolution methods to discriminate the Raman signal from fluorescence background, and various forms of signal processing. However, the lack of any notable successes strongly suggests that Raman spectroscopy is not a viable technique for direct detection of DNAPLs at any reasonable cone penetration rate. Investigators of near-infrared absorbance/reflectance, another vibrational spectroscopy complementary to Raman, have reached similar negative conclusions.

Interest remains high in a direct push method that can definitively identify, verify, and quantify DNAPL-forming volatile organic compounds (VOCs) in situations ranging from dissolved phase near the maximum contaminant levels (MCLs) to high-resolution characterization/delineation of DNAPLs source zones. The inability of optical methods to satisfy these demands has directed attention to methods based on mass transfer. In other words, instead of directing light on the sample through a sapphire-window interface, one looks for a mass-transfer interface to sample the soil matrix more conventionally. Various samplers that can access the soil matrix through a direct push probe have been developed and are in commercial use. However, those based on delivering the groundwater to the surface through small diameter tubing aren't fast enough to allow continuous logging of contaminant profiles. About five years ago, Geoprobe Systems developed and patented (US Patent 5,639,956) the Membrane Interface Probe (MIP), which allows automatic and continuous sampling of VOCs in the soil matrix. The MIP is a key element of the technology described herein.

The MIP is usually used to bring vapors to the surface for conventional detection. This SERDP project dealt with the feasibility of moving the detector downhole to gain such advantages as lower limits of detection, better spatial resolution, and reduced susceptibility to carryover in transfer lines following a heavy hit. We also wanted to better understand the nature of the mass transfer process in the MIP, and to use this knowledge to develop better membrane interfaces.

Our work was aimed at developing a complete measurement system, in which all the components worked together smoothly. The halogen specific detector (XSD) clearly emerged as the detector of choice and it is given most of the emphasis in this report. Three independent field tests were undertaken with the XSD, including an extensive study at a DoD facility (Offutt AFB). Demonstration-validation of the XSD is going forward as an ESTCP project, in conjunction with the parallel testing of two optical detectors. The photoionization detector (PID) shows promise for potential use for general VOC detection, say for gasoline or methyl t-butyl ether (MTBE). The PID is also advantageous in that it is more amenable to percussion driving than is the XSD. The photoemissive electron capture detector does not appear to have a major role for downhole deployment, unless a breakthrough in managing the interfering oxygen is achieved. Nonetheless, good science was accomplished and the results may prove useful for various uphole measurements.

The remainder of the report is outlined as follows:

- The Membrane Interface Probe (MIP)
- Downhole XSD and PID Development
- Field Studies: XSD and PID
- Photoemissive Electron Capture Detector (PE-ECD)
- Appendix A – Hardware
- Appendix B – Offutt Data

THE MEMBRANE INTERFACE PROBE (MIP)

Concept and Sampling Considerations

The MIP (see Figure 1) is pushed or driven into the ground via a series of rods, each about one meter long. The heart of the MIP is a 6.35-mm diameter disk, which consists of fluorocarbon polymer material impregnated into a stainless steel support screen. A heater element (not shown) is embedded near the membrane. Electrical power is supplied to the heater to hold the MIP's temperature near or above the boiling point of water. Typically, the temperature fluctuates by about ± 10° C in a reasonably regular fashion around the set point. The hot surfaces of the MIP heat the surrounding soil, vaporizing volatile organic compounds adsorbed in the soil and dissolved in water. The subsurface VOCs, whether initially present as gaseous, dissolved, solid, or free product phases, pass through the MIP polymer membrane and are swept with a gas flow into the detector. There is no bulk flow of gases or liquids across the membrane. Movement of species across the thin, heated membrane into the probe is rapid (requiring < 1 second for light hydrocarbons). The small pore size of the MIP membrane prevents the passage of liquid and soil particles, thereby allowing efficient operation in both the vadose and saturated zones.

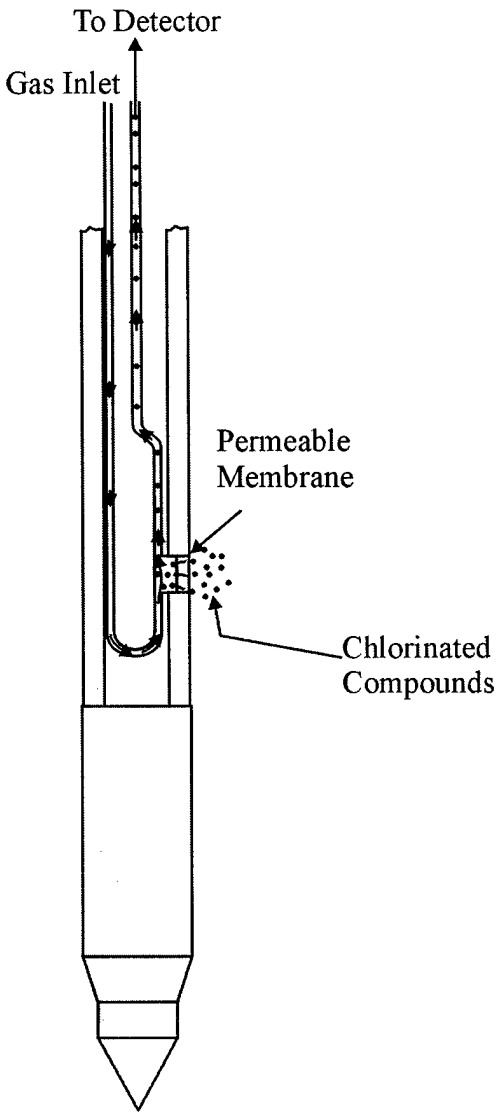

Figure 1. Schematic of the downhole sensor and membrane interface probe

The commercial version of the Geoprobe MIP system uses a return line of fluorinated ethylene propylene Teflon, typically 100 feet long, to transport VOCs to the surface for analysis. It takes approximately 35 seconds for vapor to reach the surface through 100 feet of $1/16^{th}$ inch tubing.

Motivations for Placing the Detector Downhole

Conventionally the vapors are moved to the surface for detection by gas chromatography (GC) detectors (flame ionization detector, photoionization, electron-capture) or mass spectrometers. Uphole detection gives entrée to the wide variety of well-developed and commercially available GC detectors. During the past three years, the Army Environmental Center and Waterways Experiment Station has evaluated ion trap mass spectrometers (ITMS) for uphole analysis. The ITMS provide sensitive and specific chemical analyses in a few minutes. Fast GC methods could also be used to rapidly analyze vapors returned to the surface. In the current uphole

configuration, an MIP system coupled with a flame ionization detector (FID) has a detection limit of approximately 5 mg/L of dissolved phase chlorinated VOCs.

There are several reasons for undertaking the challenge of placing the detector downhole in the soil probe. The disadvantages of drawing vapors to the surface include time lag, adsorption losses, and dilution. Careful control of gas flow rates and calibration can mitigate these effects, but the downhole detector approach is the only way to eliminate them.

Long tubing between the interface and sensor can attenuate the flow of analytes, limiting both sensitivity and the range of volatility of analyzable compounds. A more serious problem is that, after a heavy "hit," the tubing is contaminated, which can lead to severe memory effects. Imagine that the MIP has just passed through a zone of DNAPLs. A very large slug of trichloroethylene (TCE) or perchloroethylene (PCE) passes through the membrane. If the vapors are transferred to the surface for conventional detection, the entire inner surface of the transfer tubing presents a surface where the VOCs can adsorb or partition into. It may be several minutes before the VOCs have completely cleared out of the transfer lines. During this period, signals remain high. The risk is that the zone of contamination appears much thicker than it really is. Another serious limitation of drawing the vapors to the surface is poor vertical resolution. Step positioning the MIP at one-foot intervals leaves large gaps in the data, undesirable for delineating thin DNAPLs layers.

The potential advantages of performing chemically-specific downhole detection include; the near elimination of transit time lag, improved spatial resolution, and better sensitivity because of greatly reduced band broadening and loss of analyte. In the new approach, all surfaces that can contact analyte from the membrane to the downhole detector are made of inert and deactivated materials that can be heated.

MIP Characterization Studies

Mass transport across the MIP

Although it is known that bulk flow of liquid water across the membrane-sampling interface is negligible, the mechanism of mass transport across the MIP is not completely understood. Several studies were conducted during the course of this effort to better understand the mass transport of materials across the MIP. The results of these experiments are summarized in the following sections.

Membrane support material

The original MIP membranes were made of a course stainless steel mesh coated with a fluorocarbon polymeric material (Teflon). We tested a new design of Geoprobe's commercial MIP membranes based on sintered steel frits impregnated with the same polymeric material. Our finding, corroborated by independent experiments at Geoprobe, demonstrated that the frits have substantially lower mass transport than versions based on a steel mesh substrate. Based on these findings, the stainless steel mesh was reinstated as the material of choice.

Selectivity of MIP membrane

Originally, it was believed that the transport mechanism for VOCs was a combination of dissolution (of the organics in the membrane) and diffusion. If this mechanism were correct, VOCs in a VOC/water solution would pass through the membrane more efficiently than water. The experimental setup was to flow a controlled amount of 100-ppm TCE solution over the membrane using a custom designed flow cell. A SRI 8610 GC with a purge-and-trap (PAT) system was placed in line with the MIP carrier gas stream to quantify mass transport across the membrane. Organic vapors passing through the membrane were collected on the adsorbent in the trap and then injected into the GC via static heating and detected with a photoionization detector. Prior to injection of the sample, the amount of water vapor transported across the

membrane was determined by measuring the increase in the mass of the trap. The amount of water and TCE that passed across the membrane was determined to be 5 μg/sec and 0.5 ng/sec respectively. These values show that VOCs and water pass through the membrane with the same efficacy, indicating that the original mechanism is not correct. The transport mechanism now appears to be movement of the vapors through macroscopic pores rather than by dissolution and diffusion.

Water management across the MIP

As previously stated, the MIP membrane allows significant water to pass through it. Water vapor poses a significant risk for damage to our downhole sensors. The following sections describe the efforts and ultimate solution used to manage these water vapors.

Membrane coating material

The standard material Geoprobe uses to coat the membrane is Teflon. The Teflon coating process involves several steps. First, the stainless steel mesh is cleaned and baked at 600°F to drive off all solvents. Second, a thin layer of Teflon/solvent suspension is coated onto the mesh and baked again at 600°F. This process is repeated several times until the mesh is well covered. The unit is then baked at 750°F so the Teflon particles soften and anneal with their neighbors.

We identified an alternative form of Teflon (known as amorphous Teflon or Teflon AF) that is soluble in selected perfluorinated solvents. We felt that by using a solution rather than a particle suspension it would be possible to create a more uniform membrane that would be a better barrier to water. Several approaches for creating the membrane were tried: painting a viscous solution onto the stainless steel mesh substrate and allowing the solvent to evaporate, pulling a vacuum on one side of the stainless steel mesh to draw the solution through, and finally casting a film on a glass substrate and then placing the film on the mesh and annealing at high temperature. In all cases, the Teflon AF would not strongly adhere to the stainless steel so it was not possible to create a useful alternative membrane using a Teflon AF solution.

Water removal system (Nafion dryer)

The final solution for contending with the water passing through the membrane was to install a drying system between the MIP and the detectors. The drying system consisted of a length of Nafion tubing surrounded by Drierite desiccant. Nafion tubing is designed to specifically remove water vapor from a gas stream without affecting the other components. The surrounding Drierite desiccant adsorbs any water passing through the Nafion tubing. This system proved adequate for the XSD system but was modified for use with the PID system. Refer to PID – Development and Laboratory Results section for a complete discussion of the modifications made to the drying system.

Soil Probe Emulator

The goals of this project had significant qualitative and quantitative facets. The qualitative aspect relates to reliably locating the DNAPLs source terms; the quantitative aspect relates to how well one can track the dissolved phase plume emanating from the source terms.

One of the most challenging aspects of this project was the quantitative characterization of the MIP/downhole sensor system as it passes through the soil. We considered three strategies for characterizing the behavior of the sensor system during a push:

1. Measure what comes across the membrane under controlled conditions, e.g., water flowing over membrane. This approach does not take into account the impact of soil matrix and temperature effects.
2. Collect a lot of field data and analyze empirically – strategy applied by Bill Davis and Jed Costanza with ITMS uphole measurements.
3. Develop an emulator to mimic what happens downhole.

We employed a combination of the three strategies mentioned above. The first two strategies are discussed in more detail in the Downhole XSD and PID development and Field Studies sections respectively. The following sections focus on the construction and subsequent results obtained with the soil probe emulator.

Emulator Construction
A hydraulically controlled soil probe emulator was constructed (see Figure 2) to closely mimic conditions encountered by the MIP/sensor system in the field. The hydraulic system moves the sliding probe carrier back and forth. The measured maximum translational rates are 5.3 cm/sec in the forward direction (probing into the sample) and 1.22 cm/sec in the reverse (pulling out of the sample). These rates are consistent with the calculated rates. Force in the probing direction has been calculated at 2800 pounds, but not measured. An electronic control module (ECM) serves as the interface between the emulator and the data acquisition computer. The ECM supplies depth information from an optical encoder logged at the same time as the sensor signal. Adjustment of the probe rate to a constant value between 0 and 5.3 cm/sec relies on an intermittent toggle to an electronic hydraulic flow control. Constant probe rates are desired for uniform spacing of the data.

The chambers that hold the soil for testing are constructed from 12-inch sections of 3.8-in (i.d.) thick-walled plastic pipe. Up to four chambers can be held together by threaded aluminum sleeves that join one pipe to the next. Each sleeve has a baffle with a smaller diameter hole in its center to prevent soil from one chamber from passing into the next. Brackets were welded to the emulator to hold the soil sample unit in-place. With this configuration, four discrete soil units, each filled with a soil tainted at different contamination levels or species can be analyzed.

Much work went into finding a soil mixture and mixing protocol that reproduce a zone of homogeneously contaminated soil. Our initial approach was to fill an entire sample cylinder with about ten pounds of contaminated soil. We later discarded this approach in favor of smaller two-pound batches homogenized by kneading in Ziploc bags. This method produced the homogeneous soil samples we needed.

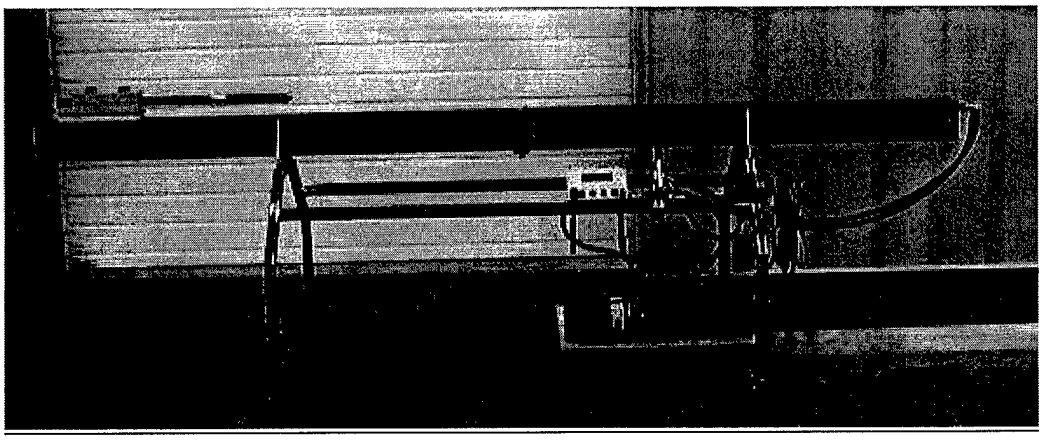

Figure 2. Soil probe emulator

The soil mixture containing sand, silt and clay was prepared according to the following recipe (by dry weight):

19% Old Hickory ball clay
25% ground silica - silt

37% fine silica sand
19% medium silica sand

Soil mixtures containing different amounts of water (14.2%, 12.5%, and 11% water by weight) were tested. The mixture with 14.2% water was too wet; the soil with the 11% water could readily be packed tightly into the sample cylinders but was very difficult to mix. The soil mixture with 12.5% moisture offered the most reasonable compromise.

Emulator Results
Results from duplicate emulator runs are shown in Figure 3. The standard procedure for filling the cylinders was to place approximately 2 pounds of soil into the cylinder and pack it down with a tamper. This procedure was repeated until the sample cylinders were filled. For these pushes, a 3-inch layer of contaminated soil (100 ppm TCE) was located at 1.4-1.7 feet. The sample cylinders were then screwed together and secured in place on the emulator. The probe was finally advanced through the soil at 0.5 cm/sec.

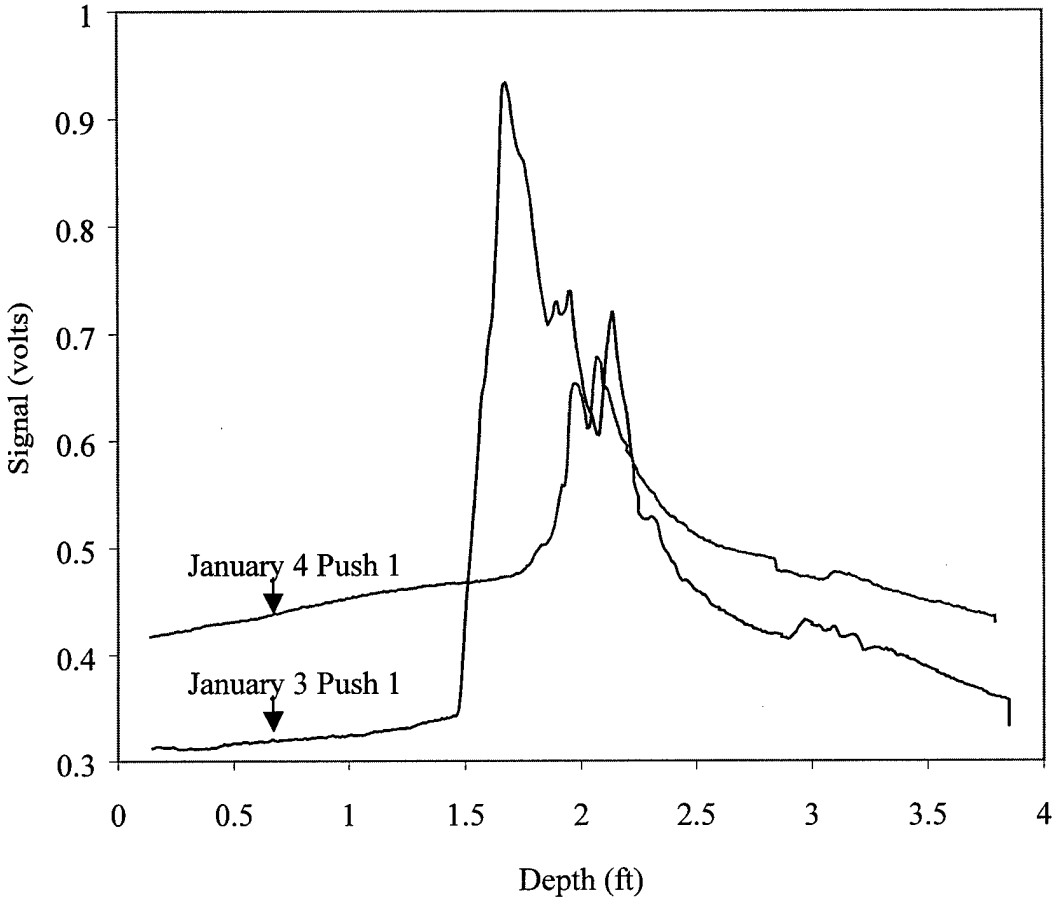

Figure 3. Emulator pushes (100 ppm TCE mixture placed from 1.4 to 1.7 feet) on different days

Three important features can be seen in these pushes. First, while the shapes of the contaminant signals are reasonably similar, the amplitudes differ by more than a factor of two. Secondly, the depths do not match well. Finally, the signal levels oscillate while the probe is in a contaminated cylinder. The signal level variability and the depth of the contaminant area both depended on how tightly the soil was packed into the cylinder. The oscillations were caused by sample inhomogeneity as a result of the "layering" method of the soil packing. All of these differences were caused by the inherent deficiencies of the soil packing procedure.

While the emulator did not yield the quantitative answers we had hoped, an important operational feature of the MIP was clarified. A common operational mode for MIP systems is to incrementally advance the probe. In the incremental advancement mode, the probe is advanced in discrete intervals (typically one foot once per minute), a sample is collected, and the probe advanced again. However, we typically operate, and have advocated, a continuous advancement approach (i.e. continually advance the probe only stopping for rod changes) because of the increased vertical resolution. During pushes with the emulator, another important reason for continuous advancement was noted. A common problem encountered during pushes was soil drying onto the membrane ("scabbing"), effectively blocking sample from crossing it. This problem was further exacerbated when the probe was stopped in the sample cylinders. While the pressure exerted on the MIP in the ground is greater than in the emulator, the results of the emulator tests proved to us that continual advancement was the best mode of operation.

DOWNHOLE XSD AND PID DEVELOPMENT

Gas chromatography literature provided an excellent guide to the detector options. Any detector that could suffice for downhole operation is probably represented in the GC literature. However, due to the unique characteristics of our problem the converse was definitely not true. Obviously, size is a major consideration. Ideally, one would like the detector to fit within standard size rods, as small as 0.75 in. (i.d.). We considered rods up to 1.5 in. (i.d.) but the larger the rod; the harder it is to push.

Most GC detectors are designed to work with a highly controlled carrier gas flow. We are using a carrier gas as well, but other gases can get into the carrier gas and may interfere with detector operation. As previously mentioned, the MIP passes a lot of water vapor. Oxygen also passes through the membrane in variable amounts. In the vadose zone, oxygen represents ca. 19% of the vapor present in the soil; this amount is decreased if biological action is present. In the saturated zone, the solubility of oxygen in water is about 8 mg/L, which is comparable to the amount of chlorinated species present at moderately to highly contaminated sites. Thus, the detector of choice must be immune to changes in water and oxygen levels or the water and oxygen must be removed prior to introduction into the detector.

A list of the most popular GC detectors is given in Table 1. We must take into account that many of the sites with chlorinated solvent contamination will also exhibit contamination by fuels, MTBE, and other species. Thus, the specificity of the detector is relevant.

Table 1: GC Detectors

PID	Photoionization detector
FID	Flame ionization detector
ECD	Electron capture detector
TCD	Thermal conductivity detector
NPD	Nitrogen phosphorus detector
XSD	Halogen specific detector

The ideal then is a small detector that responds specifically to chlorinated compounds with minimal interference from other hydrocarbons, water vapor, or oxygen.

Vision for the Project – ca. 1997
The essence of the proposed research was to identify, develop, and field test vapor detectors that could be operated downhole in close proximity to the MIP. Table 2 provides a qualitative description of the approach as envisioned at the start of the project and Table 3 summarizes the quantitative performance goals.

Table 2: Qualitative Description of the Approach

Need	Satisfaction
Innovative technology	Custom-developed thermionic sources, downhole implementations of ECD and IMS, photoemissive electron sources, Geoprobe's patented membrane interface
Minimally intrusive	Direct push deployment by CPT and Geoprobes
Detect and locate DNAPLs	Highly sensitive and specific for chlorinated hydrocarbons
Quantify DNAPLs	Gas phase measurements eliminate matrix effects
Map horizontal and vertical extent	Better depth resolution than techniques that draw vapors to surface
Real-time and easily interpretable	Directly provides log similar to those provided by LIF for fuels

Table 3: Performance Goals for the Sensors

Parameter	Goal
Sensor responsiveness	All significant organochlorine compounds, including TCE, PCE, and TCA
Vapor sensitivity	< 1 ppmv (corresponds to dissolved concentrations in the low µg/L range)
Selectivity	Greater than 5000 relative to non-chlorinated hydrocarbons (i.e., fuels)
Response time	< 3 seconds for 10% ↔ 90% response in both directions
Acquisition cost	Comparable to RCL sensor, lower than ion trap mass spectrometer
Operational requirements	Separate operator not required
Maintenance requirements	Routine, performed by technician

The first year of the project saw some major changes in the detectors investigated. In the initial proposal, we suggested three modified GC detectors: a thermionic ionization detector (TID), a photoemissive electron capture detector (PE-ECD), and a photoemissive ion mobility spectrometer (PE-IMS). Owing to budget restrictions, the PE-IMS was dropped from the project before it began. Early in the contract, our attention was directed to the XSD, which, like the TID, relies on a high temperature combustion process. However, the XSD is much less demanding of the carrier gas properties than the TID. In addition, our preliminary experiments showed that the TID performance tended to degrade fairly rapidly. Once we verified that the XSD was comparably sensitive (in fact, it is quite a bit more sensitive than the TID) and showed stable operation over several weeks, the decision to replace the TID with the XSD was an obvious one.

The classic detector for chlorinated substances is the electron capture detector (ECD). Our intention was to replace the conventional radioactive ECD source with a photoemissive (PE) source. We thought the PE source was attractive for several reasons. First, it avoids the issues of licensing and regulatory approval that radioactive sources incur. Secondly, DTI and our collaborators at North Dakota State University (NDSU) had substantial experience in processing the transient signals expected as the result of back-side irradiation of a gold-coated window with the output of a flashlamp. Finally, the PE-ECD source could serve as an entrée to the photoemissive ion mobility spectrometry concept from the original proposal.

We kept the faith on the PE-ECD, although it was never implemented in a full downhole configuration for field studies. Our collaborators at NDSU primarily conducted the PE-ECD studies.

The development of a downhole photoionization detector (PID) was not anticipated when the contract work began. The PID responds to a wide range of hydrocarbons and therefore does not meet the requirement for specific response to chlorinated organic compounds. However, we realized it presented several advantages for meeting the contract goal:

- The downhole PID was better suited to "working out the bugs" of features it had in common with other proposed detectors (e.g. XSD, PE-ECD, and TID), e.g., the downhole current-to-voltage amplifier and the use of Nafion for water management.
- The inexpensive nature of the PID sensor components (vacuum ultraviolet lamp and collector electrode) made it convenient for assessing test procedures, resolving integration issues, and field-testing the control and data acquisition software.
- PIDs are very commonly used for field screening soil cores at the surface. The downhole PID therefore provides a convenient basis for comparing results to those obtained by traditional approaches.

The following sections discuss the development and laboratory experiments of the XSD and PID. Refer to the Photoemissive Electron Capture Detector (PE-ECD) section of this report for a complete discussion of the PE-ECD development.

XSD –Concept and Principles of Operation

The halogen-specific detector is commercially available in a conventional GC detector package from OI Analytical. The detector has a dynamic range greater the $1x10^5$ and a linear range greater than $1x10^4$, 1 pg Cl/second sensitivity, and better than $1x10^4$ selectivity against non-chlorinated hydrocarbons. It requires a flow rate of 20-30 mL air per minute; ultra-high purity is specified. The stated applications include halogenated compounds, VOCs, pesticides, and PCBs. A picture of the XSD can be found on the web at http://www.oico.com/instxsd.htm.

OI's literature describes the XSD's principle of operation as: "The reactor is operated in an oxidative mode, which pyrolizes the effluent from a GC column. This oxidative pyrolysis efficiently converts compounds containing halogen to their oxidation products and free halogen atoms. The cathodic surface is activated by neutralization of alkali ions emitted from the anodic surface. The adsorption and reaction of free chlorine atoms with this alkali-sensitized cathodic surface yields an increased thermionic emission comprised of free electrons and halogen ions. The total cathodic current is measured by the Model 5360/5360A electrometer and converted to a 0-1 V or 0-10 V output signal, which can be readily coupled to a chromatographic data handling system."

The underlying principle for the XSD operation is the pyrolysis of the molecules in the carrier gas stream. Pyrolysis is a high temperature process in which compounds are "burned." Organochlorine species in the sample vapor undergo oxidative combustion as they enter the high temperature environment of a reactor core. The XSD is advantageous for our application in that the oxidant is simply air. In contrast, a FID or TID— originally envisioned for the project— requires hydrogen. The combustion products are carbon dioxide, water, and an equilibrium mixture of halogen atoms and halogen dimers. Because one of the combustion products is water, the XSD shows a good tolerance to water in the carrier gas.

Figure 4 shows the probe head assembly and the corresponding electrical circuit. The three functional components of the XSD probe head are; a beaded platinum cathode, a surrounding platinum spiral anode, and a support rod fabricated of an alkali metal-doped ceramic known as

mullite. The probe head assembly fits inside a reactor core surrounded by platinum heating wires (Figure 5). A ceramic material, known as Fiberfrax, is built up around the heating wires to insulate the reactor core.

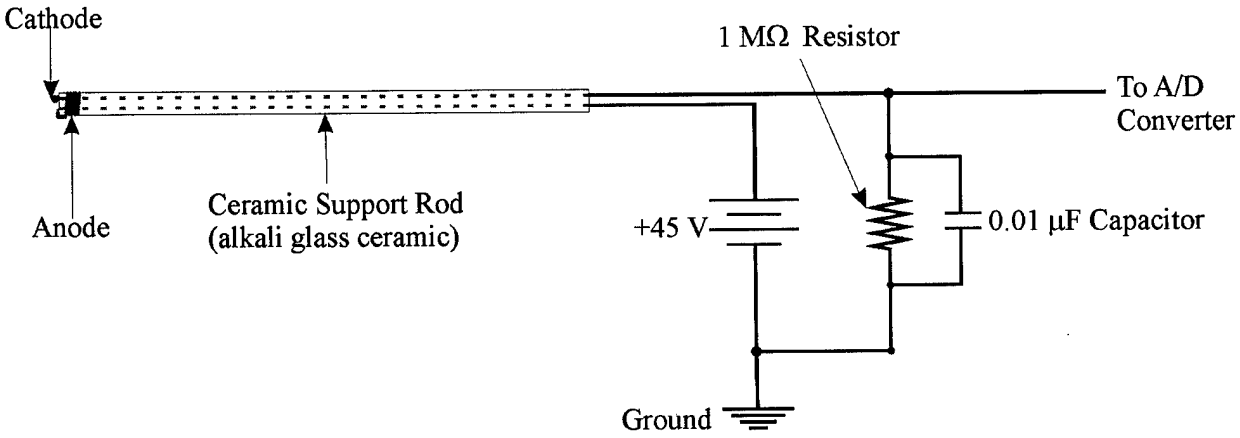

Figure 4. Downhole XSD circuit

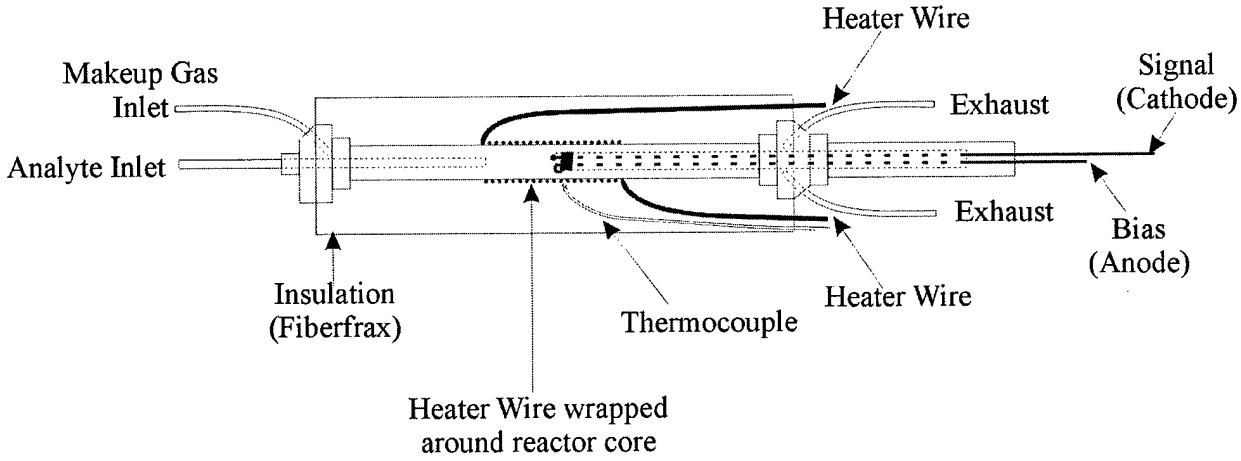

Figure 5. Schematic of downhole XSD components

The reactor core is operated at high temperatures, typically between 800-1100 °C. At these temperatures, alkali metal ions are emitted from the ceramic support rod and coat the surface of the platinum cathode, lowering its work function. The halogen atoms and dimers from the combustion process are then adsorbed onto the alkali-activated cathode surface as they come into contact with it and a current is generated.

There are three known mechanisms that could account for generation of electrical current in the halogen-specific detector: positive surface ionization (PSI), negative surface ionization (NSI), and thermionic electron emission (TEE). With the halogen-specific detector, only TEE can provide enough electrons to account for the current generated. TEE occurs when electrons are emitted from a negatively biased surface (cathode) into the gas phase. As the electron affinity

approaches the work function, the probability of a negative ion being created increases rapidly. If the electron affinity exceeds the work function of the cathode, the excess energy can be imparted to the surface resulting in an increase in TEE because of a local temperature increase (which lasts until the surface thermally equilibrates with the body of the cathode).

In the case of the halogen-specific detector, the cathode actually experiences enhanced thermionic electron emission (TEE). Two mechanisms are thought to contribute to the enhanced TEE: (1) the cathode work function is further reduced by the halogen adsorption above that associated with the alkali metal adsorption; and (2) that attachment of the halogen, with it's large negative electron affinity, increases the local temperature of the cathode.

Functional Description of Downhole XSD System

A conceptual drawing of the downhole XSD system is shown in Figure 6. The system consists of the downhole sensing apparatus tied by an umbilical cable to the uphole components. These uphole parts include power supplies, an analog-to-digital converter, a laptop computer for data logging, and a carrier gas supply. The downhole portion consists of the MIP that samples the soil matrix for VOCs, a Nafion drier to remove water vapor, the XSD sensor module, including electronics, and the water block. The uphole components include a power supply for heating the MIP membrane, another power supply to heat the XSD reactor core, an analog-to-digital (A/D) converter to digitize the analog signals from the XSD, and a laptop computer for logging and displaying the data. The umbilical, connectors and water block are discussed in more detail in Appendix A - Hardware.

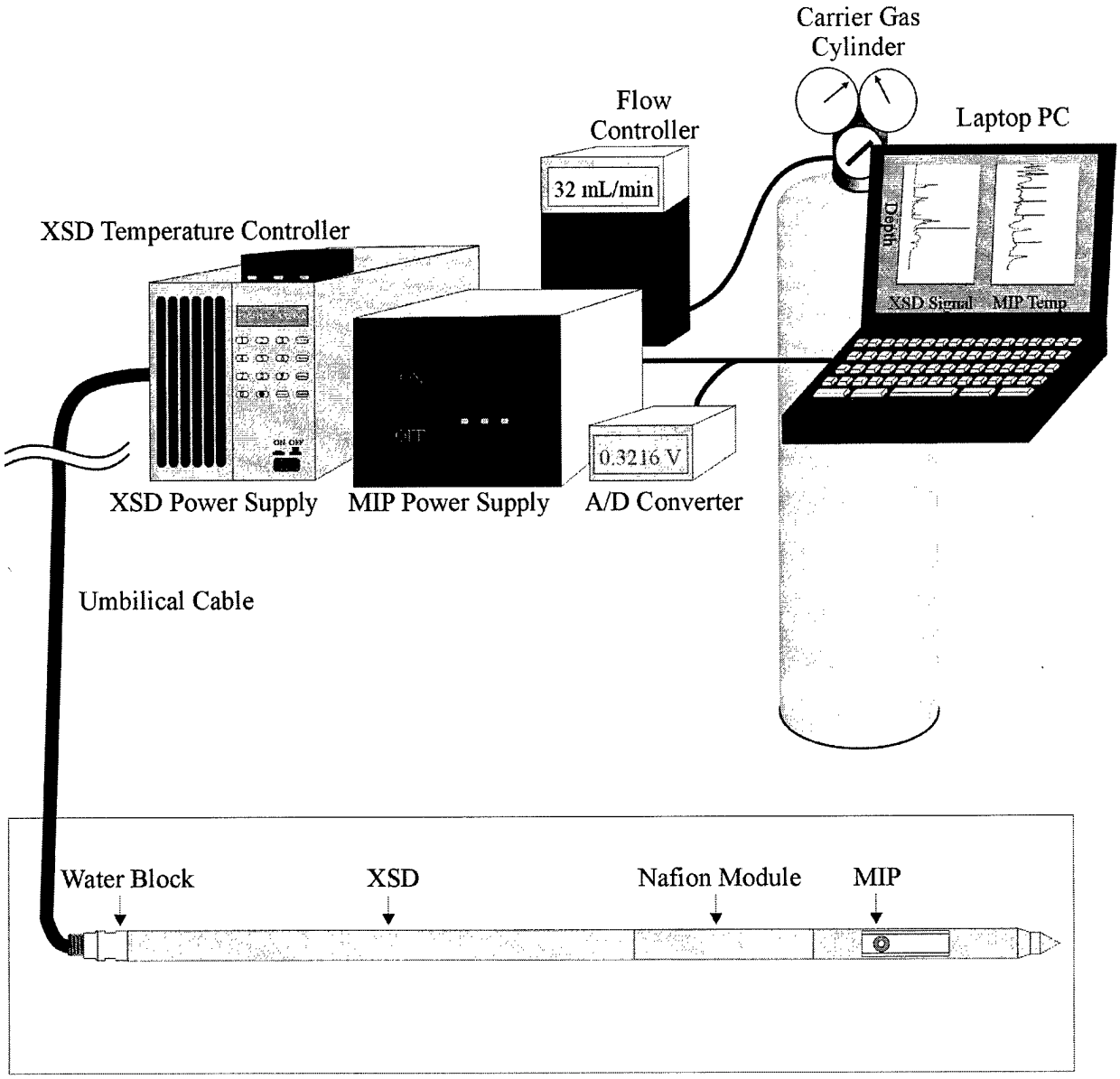

Figure 6. Diagram of XSD system

Preliminary Laboratory Studies

Calibration with gas standards generator

A calibration curve was generated by presenting the XSD with gas samples of known vapor composition. A gas standards generator constructed at DTI was used to prepare the gas samples. The gas standards generator allows vapors that are emitted at a known rate from a permeation tube to be diluted with a carrier gas at a carefully measured flow. In this case, the analyte was TCE and the carrier/diluent gas was air. The gas flow rate through the detector was held constant at 40 mL/min. An uphole, stand-alone XSD similar to the downhole XSD was operated at 5.0 amps and 9.4 volts for an operating temperature of 958-961°C. The TCE was supplied by an HRT-005.00-4036/u (5 cm length) permeation tube from Kin-Tek Laboratories, Inc. The tube is specified to delivered 1060 ng/min of TCE. The oven flow was held constant at 110 mL/min

while the diluent flow was varied. The distance between the gas standards generator and the XSD was approximately 1.5 meters.

Figure 7 displays the background corrected calibration curve, which is linear up to about 200 ppbv and then gently rolls off at higher concentrations. From these data, one could convert the XSD response during a downhole push to an absolute flow rate. However, information on the mass flow across the MIP membrane would be needed to determine concentrations in the environment.

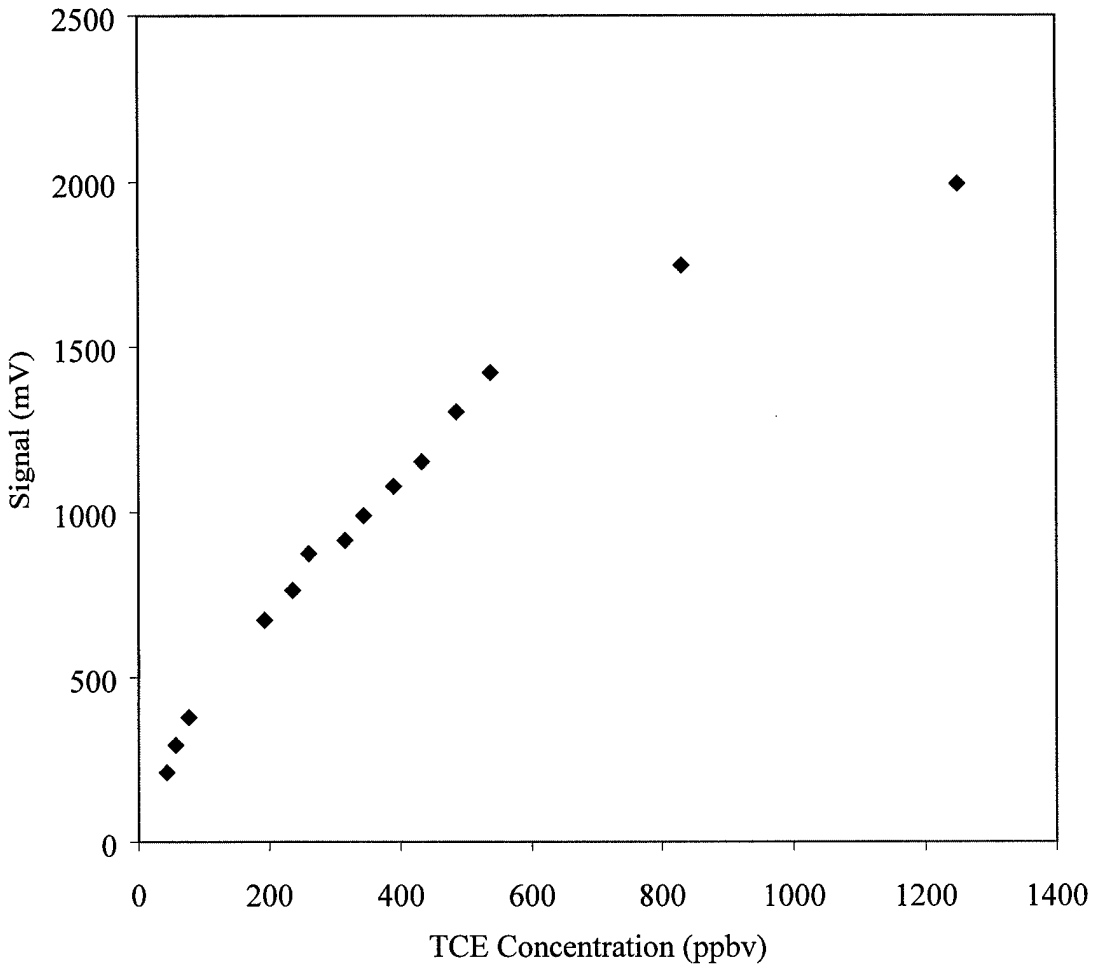

Figure 7. XSD calibration using seeded TCE in air carrier gas.

Temperature dependence of XSD response

The XSD response for a fixed flow rate of analyte vapor through the reactor zone is a strongly increasing function of temperature. However, the baseline response associated with TEE also depends on temperature. The commercial version of the XSD can be operated at four fixed temperatures (800-1100 °C in 100 °C increments). As described below, the downhole XSD was constructed such that we expected its response to be very similar to that of the uphole version, but experiments were carried out nonetheless, to establish an optimal operating temperature.

The setup for the experiment was to use a downhole XSD in conjunction with a downhole GC developed by DTI under an EPA SBIR Phase I Contract (#68-D-99-040) and a MIP. A solution containing 1 mg/L TCE and 1 mg/L PCE was flowed over an MIP at 120°C for 1 minute. After one minute trapping of the vapor passed through the MIP membrane onto a Tenax-filled trap, the trap was ballistically heated to drive the trapped analytes directly onto a 5-meter Restek MXT-1 column. A chromatogram was then collected. The current to the XSD reactor core was then increased and, after the core's temperature had stabilized the procedure was repeated.

The data shown in Figure 8 illustrates that the baseline signal from the XSD is a strongly increasing function of temperature, whereas the TCE and PCE responses plateau at a little above 1000°C.

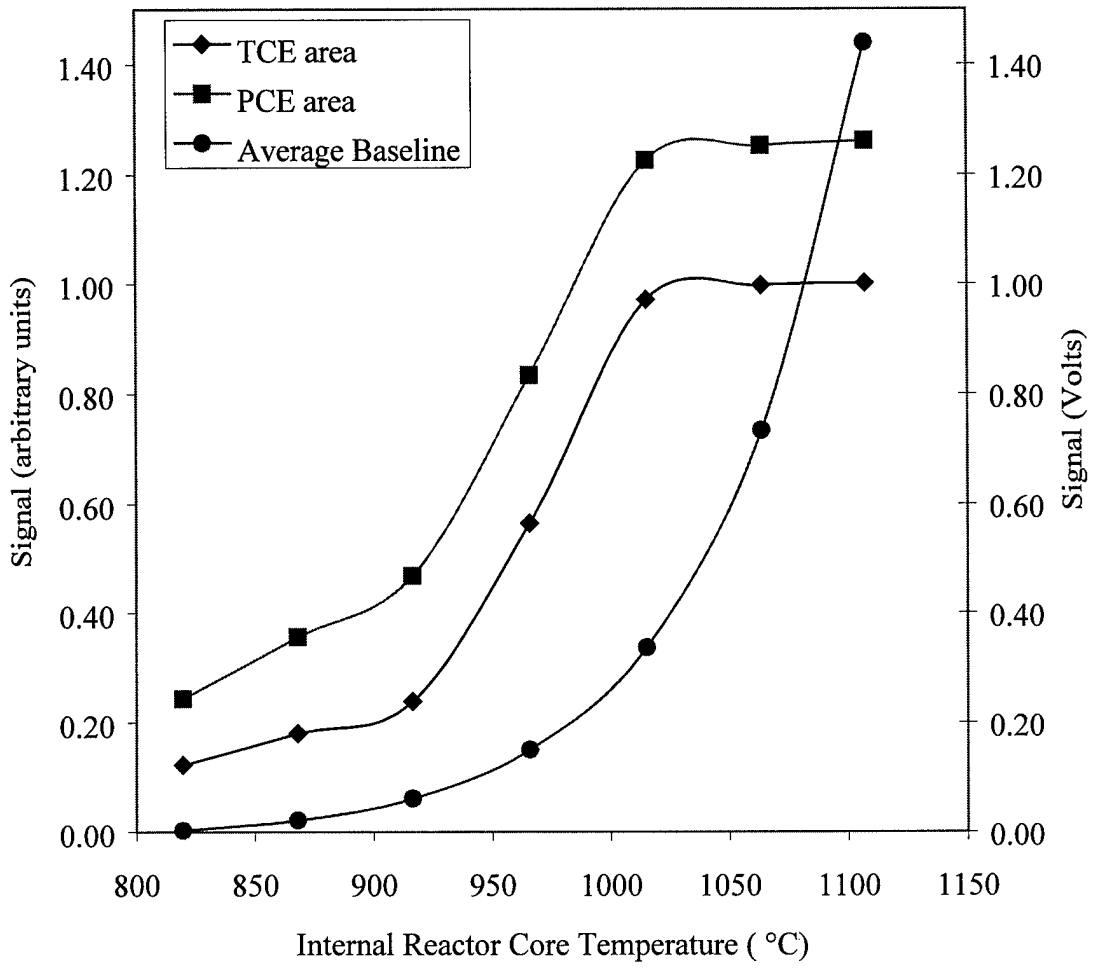

Figure 8. Temperature dependence of the XSD baseline and response to TCE and PCE

These results are readily interpreted with the aid of XSD theory. As noted above, pyrolysis in the XSD generates carbon dioxide, water, and an equilibrium mixture of halogen atoms and halogen dimers. The higher the temperature, the further the equilibrium lies in favor of the halogen atoms. The relative concentration of halogen dimers is very low for temperatures ≥1000 °C. Thus, the leveling off of the signal indicates the point at which the equilibrium between halogenated dimer and free halogenated atoms has been pushed fully to the left as given by:

$$2\,X^{\cdot} \Leftrightarrow X_2$$

Moreover, we can conclude that the XSD response is much stronger to chlorine atoms than it is to chlorine dimers.

The current associated with TEE is given by:

$$i = a_s A T^2 \exp(-\phi/kT) \qquad \text{Equation 1}$$

where a_s is the surface area of the negatively biased electrode, A is a constant whose value is 1.20 A/mm^2K^2, T is the temperature of the negatively biased surface, ϕ is the work function of the negatively biased electrode, and k is Boltzmann's constant. The baseline current was fit to the second equation; the results are shown in Figure 9. As can be seen, the fit between actual and calculated is quite good. A value of 2.07 electron volts (eV) was determined for the work function of the platinum cathode.

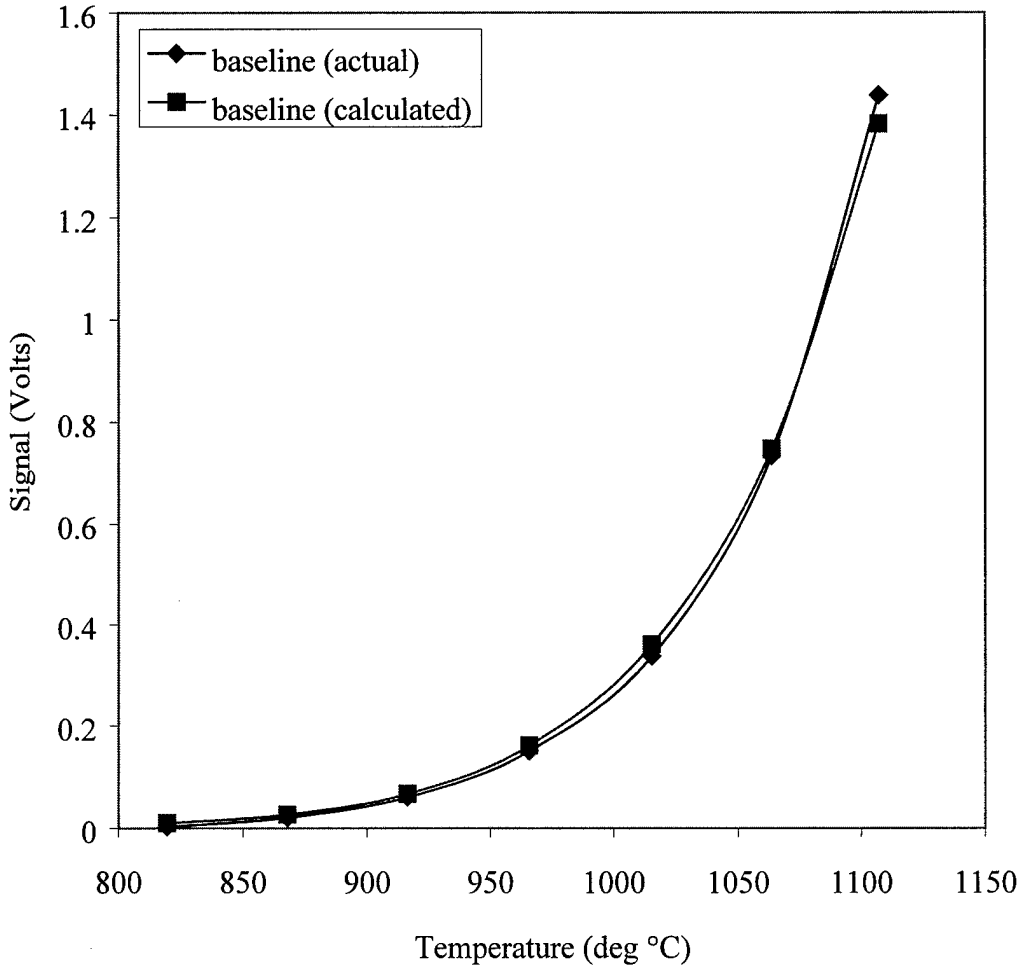

Figure 9. Fit of Equation 1 to the baseline current as a function of temperature

Several practical factors are relevant to the choice of an operating temperature for the downhole XSD.

Factor 1: Signal/noise ratio
The relevant parameter is the analyte response relative to the variation in the baseline current when no analyte is present (baseline noise). For XSD reactor core temperatures above 800 °C, we found that the baseline noise was nearly constant at 5 mV (see below –paragraph after Factor 4).

Factor 2: Operating range of analog-to-digital converter (ADC)
The operating range of the analog-to-digital converter (ADC) was 0-10 volts. The higher the operating temperature, the lower the dynamic range for the analyte measurements. Above 1050 °C, the reduction in dynamic range owing to increased baseline current becomes appreciable.

Factor 3: Material selection
Many of the materials in the downhole XSD have an upper operating range of 1200 °C. We wanted to operate the XSD at least 100 °C lower than this temperature to provide an adequate safety margin.

Factor 4: Power required by the XSD
The XSD reactor core requires substantial electrical power to attain its operating temperature. It was determined that, for each 10-degree increase, 5 more watts of power were needed. The maximum power that can be supplied over a 100-foot umbilical cable is 170 W, and 120 W are required to operate the XSD at 1000 °C. In principle, a temperature of 1100 °C is attainable. However, to compensate for any additional power requirements by the XSD as it was advanced into the ground, we deemed it advantageous to operate the XSD at a temperature somewhat lower than the maximum power.

Since S/N ratio remains constant at or above 1000 °C, factors 2, 3, and 4 dictate an optimal operating temperature at or a little above 1000 °C. Since a thermocouple could not be imbedded directly into the reactor core, an external thermocouple was imbedded just above it. The relationship between the internal and external temperatures was found and used to maintain the XSD at or slightly above 1000 °C. This eliminated any signal fluctuations due to equilibrium effects.

With this information, the choice of the XSD lower operating range was set at nominally 1000 °C.

Effect of temperature drift on response
Limits of detection are affected by fluctuations in the baseline current, not by the current's magnitude. In other words, a high baseline current is not a problem if the current is stable. We determined that the fluctuation in the baseline current does not depend strongly on temperature for laboratory operation. The baseline current varies by about 5 mV/deg. However, XSD operation involves pushing a probe into the ground. As the probe encounters different soil conditions, the rate at which heat flows away from the probe varies substantially. This effect is particularly pronounced as the probe moves from unsaturated to saturated soils, due to the high heat capacity of water. Ideally, a layer of Fiberfrax thermal insulation thick enough to minimize temperature fluctuations in the reactor core would surround the reactor core. However, space constraints limit the amount of insulating material that can be used.

Early field pushes indicated that the XSD temperature dropped significantly during a push. Failure to properly compensate for such temperature swings could lead to erroneous results. At a

minimum, the ability to see small true signals associated with chlorinated solvent contamination is degraded. Extensive studies were carried out to test how well the baseline data could be corrected using a correlation of XSD response as a function of reactor core temperature. A challenge for this correction was the inability to measure the vapor temperature inside the reactor core while the analyte was flowing through it. However, we were able to show that a temperature measurement near the heating coils can be related to the actual temperature in the reactor core. This correlation was found by replacing the normal probe head assembly with a probe head equipped with a thermocouple. A second thermocouple was placed near the heating coils of the reactor core. The XSD was then ramped through a series of temperatures and a correlation between the two thermocouples was found.

Figure 10 shows the results of laboratory experiments in which the temperature of the XSD was deliberately reduced by pouring cold water on it. The 15-degree temperature reduction has a substantial effect on the XSD baseline signal. A correction factor, based on equation 1, was then applied to the baseline signal to correct for these fluctuations. The corrected baseline shows a substantial improvement in baseline stability.

The results of these experiments indicated that we could effectively correct for baseline fluctuations by actively monitoring the XSD temperature and then applying a correction factor. However, because of the differences in each XSD and the variability at field sites, a global fit of the XSD temperature versus baseline signal never yielded acceptable results. A method of removing the temperature fluctuations was deemed necessary to alleviate these problems. Toward this end, a high precision power supply and temperature controller were purchased and implemented with the XSD. Fluctuations of the baseline signal during a push have been reduced to ±0.5 C around the set point. Field implementation of this approach has revealed that the fluctuations in the baseline —in an area known to be contaminant free— are less than 10 mV. This is much better than was ever achieved using the aforementioned correction factors and has resolved the temperature fluctuation issue.

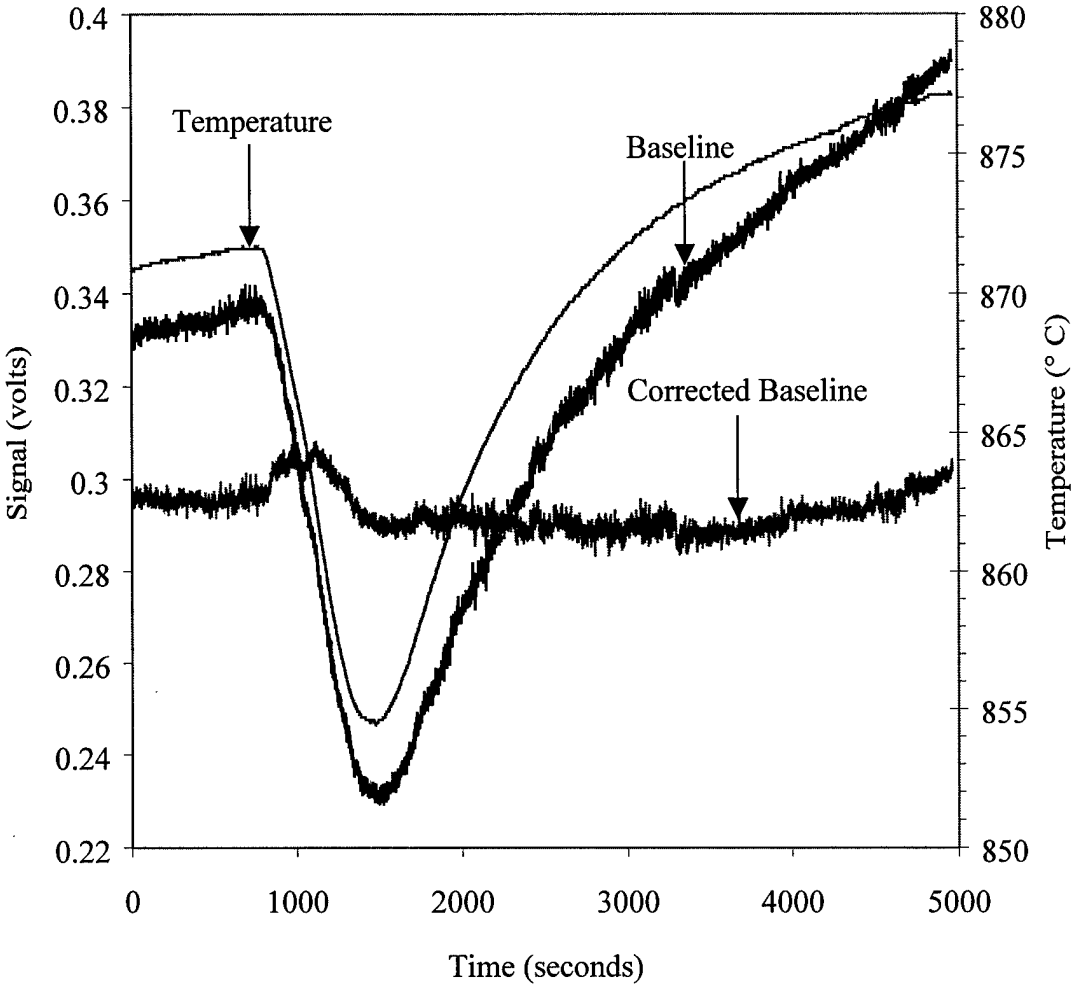

Figure 10. Results of baseline signal correction as a function of temperature

Non-response of XSD to water vapor

Because the combustion process in the XSD generates water vapor, we expected that the XSD would be able to tolerate an additional water vapor burden. Furthermore, since we placed a Nafion drying unit between the MIP and XSD we were confident that the amount of water that reached the XSD would be minimized. To test these suppositions, an experiment was conducted to determine the effect of water vapor on the XSD signal. The Nafion drying unit was removed from the system so any water vapor passing through the MIP would be introduced into the XSD. Aliquots of 10-ppm TCE solution and pure water were alternatively placed on the membrane. The results of the experiment (Figure 11) clearly indicate that water vapor passing through the XSD does not change the XSD signal.

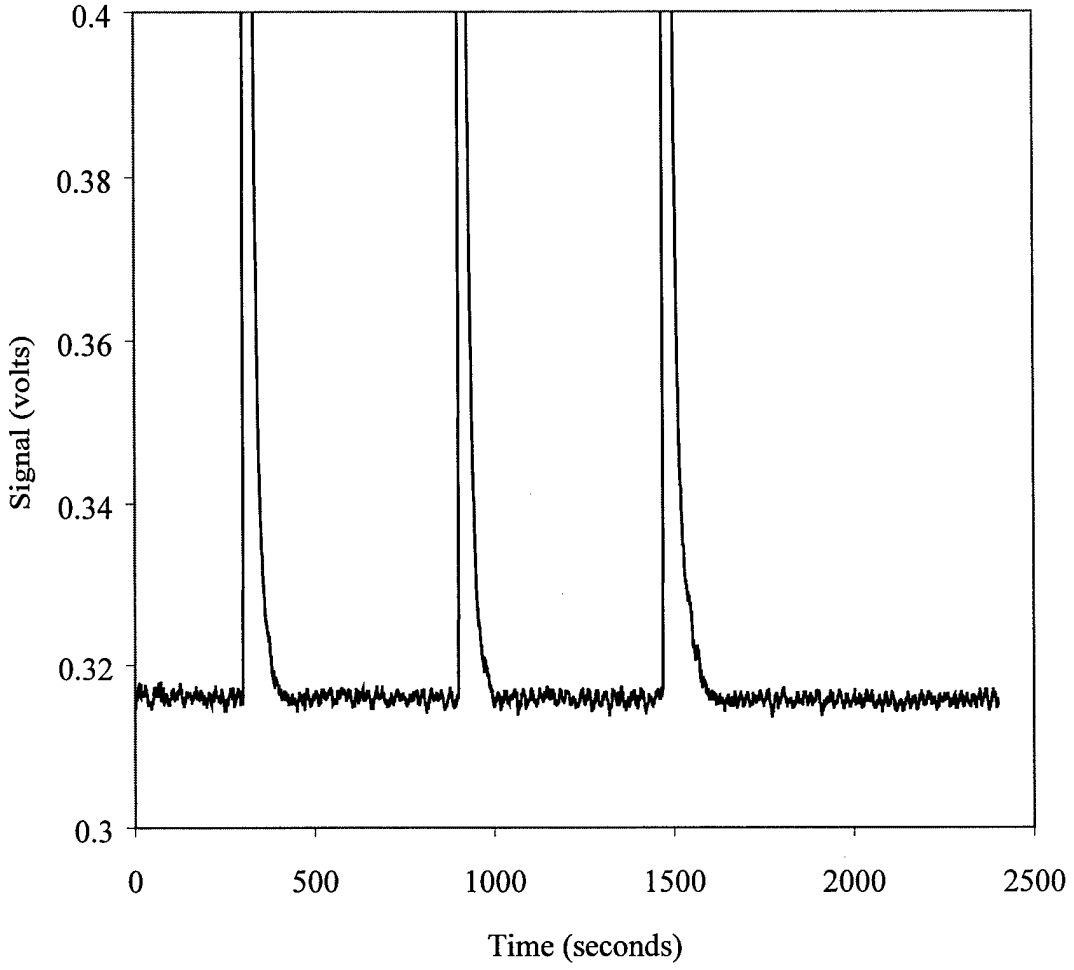

Figure 11. Non-response of XSD to water. A 500 μL aliquot of 10-ppm TCE solution was placed on the membrane at 300, 900, and 1500 seconds. A 2000 μL aliquot of water was placed on the membrane at 600, 1200, and 1800 seconds.

Non-response of XSD to non-chlorinated hydrocarbons

Figure 12 shows that the XSD is highly immune to non-chlorinated hydrocarbons. For these experiments, the downhole XSD was operated as a GC detector. A mixture of 100 mg/L of BTEX, TCE, and PCE was injected on a GC equipped with a PID, which responds to both the chlorinated and non-chlorinated species. The XSD was positioned following the PID. The TCE and PCE peaks in the XSD are broadened because of large dead-volume in the gas lines and connectors between the PID and the XSD, but the lack of any discernible XSD response to the BTEX components is clear.

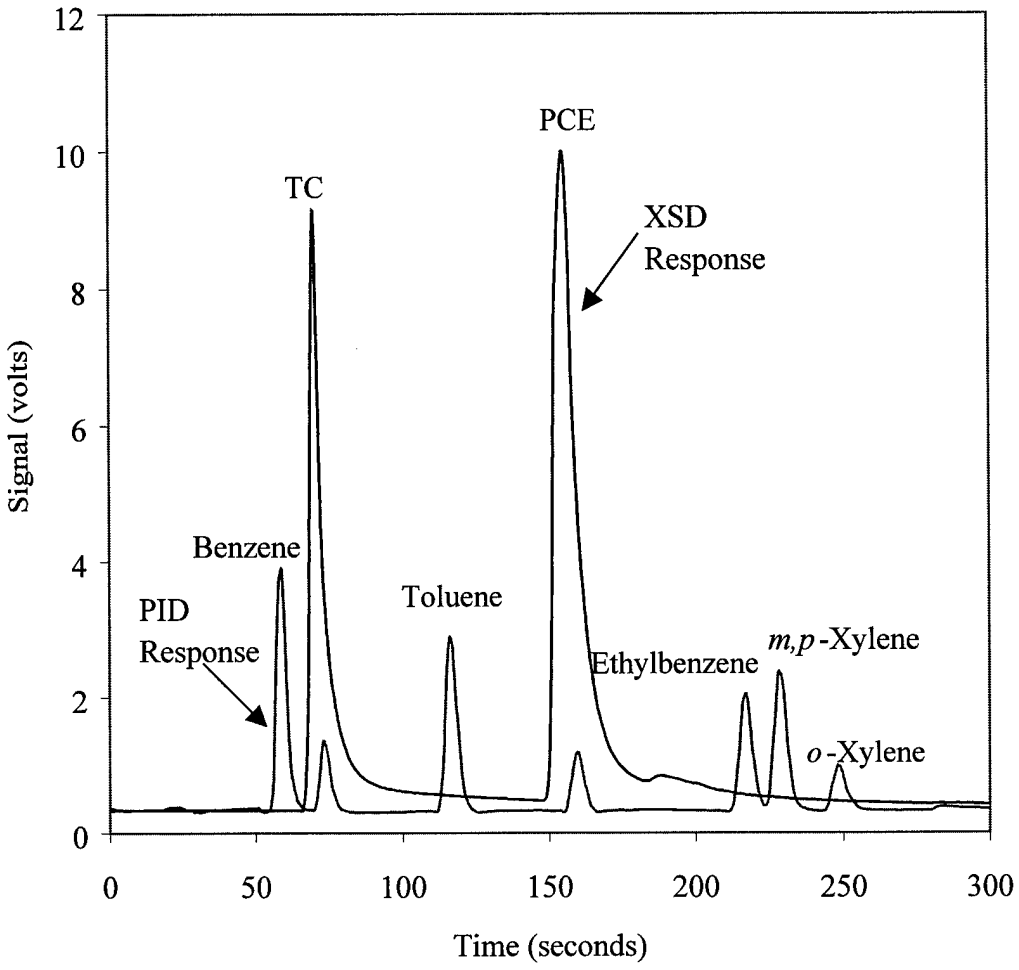

Figure 12. Non-response of XSD to 100 ppm of BTEX

PID – Development and Laboratory Results

A picture of the final version of the PID is shown in Figure 13. While earlier versions relied on the PID being sealed with epoxy to make it gas-tight, this version incorporates miniature screws and nuts to accomplish the sealing. This makes for a more field-serviceable unit that can be readily disassembled for maintenance and cleaning. The complete downhole unit is shown in Figure 14. At the ends of the unit are elastomer supports with stainless steel outer rings that hold the unit in the pipe. The elastomer rings provide a very smooth ride for the PID. While percussion hammering has not been extensively investigated, it has been hammered in the field on occasion with no adverse affects.

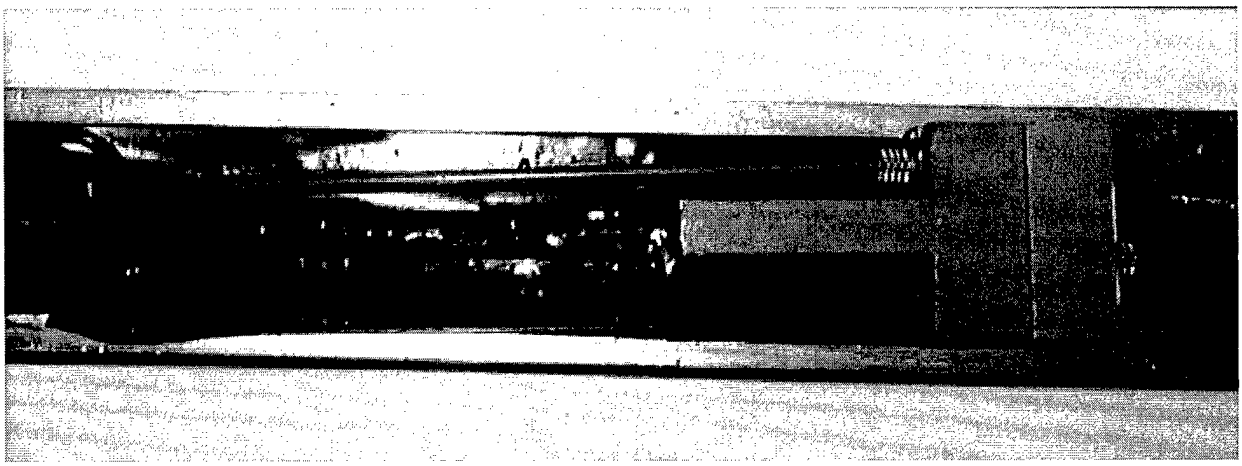

Figure 13. Downhole PID

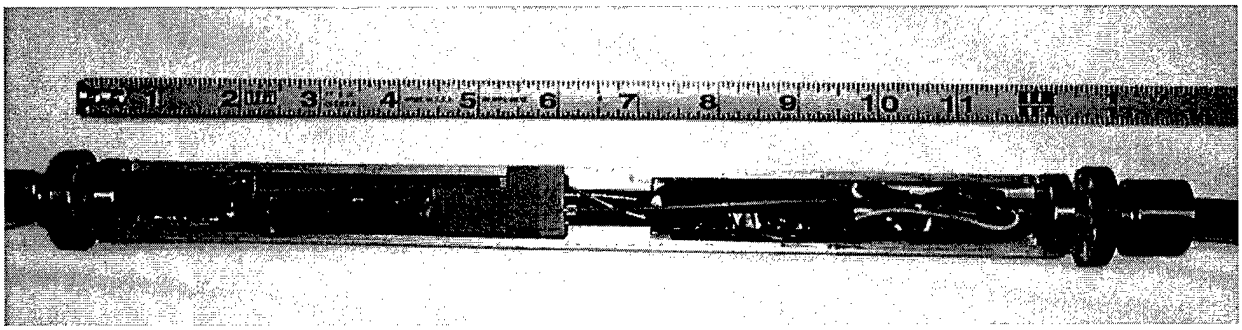

Figure 14. Assembled downhole PID unit with cover removed for viewing

Similar to the XSD, the PID encountered problems with both electrical connectors and water-tightness. Early versions of the PID used LEMO connectors like the XSD, however, the latest version of the PID no longer uses LEMO connectors but is "hard-wired" instead, an approach where the wires run from the surface directly to their necessary position. This benefits the PID by reducing the noise intrinsic to connectors. This is particularly important in light of the fact that the innate currents generated by the PID range from tens of picoamps to several nanoamps. In contrast, the XSD generates currents in the microamp range making it less susceptible to noise. The entire unit is sealed with a bead of silicon RTV compound making it submersible. Figure 15 shows a benchmark of the PID's performance vs. that of a commercial PID. The test mixture contained benzene (0.3 ppm), TCE (0.4-ppm), and PCE (0.8 ppm) and was eluted on an SRI gas chromatograph. The effluent of the GC first passed through the SRI PID and then through the DTI PID. The DTI PID generated approximately 5 times the signal as the SRI PID, but the baseline noise was higher (± 320 μV for DTI vs. ± 4 μV for SRI) for the DTI PID. This is largely due to the analog-to-digital converters (ADC) that are used. In the DTI system, a 12-bit ADC is used with a minimum range of one volt; therefore, 250 μV is the minimum digitization step. The SRI system on the other hand utilizes a 19-bit ADC with a range of 4V producing a step of 10 μV. We have begun to incorporate "on chip" averaging of the signal presented to the ADC. With this and improved shielding of the electronics the noise has been reduced to ± 80 μV.

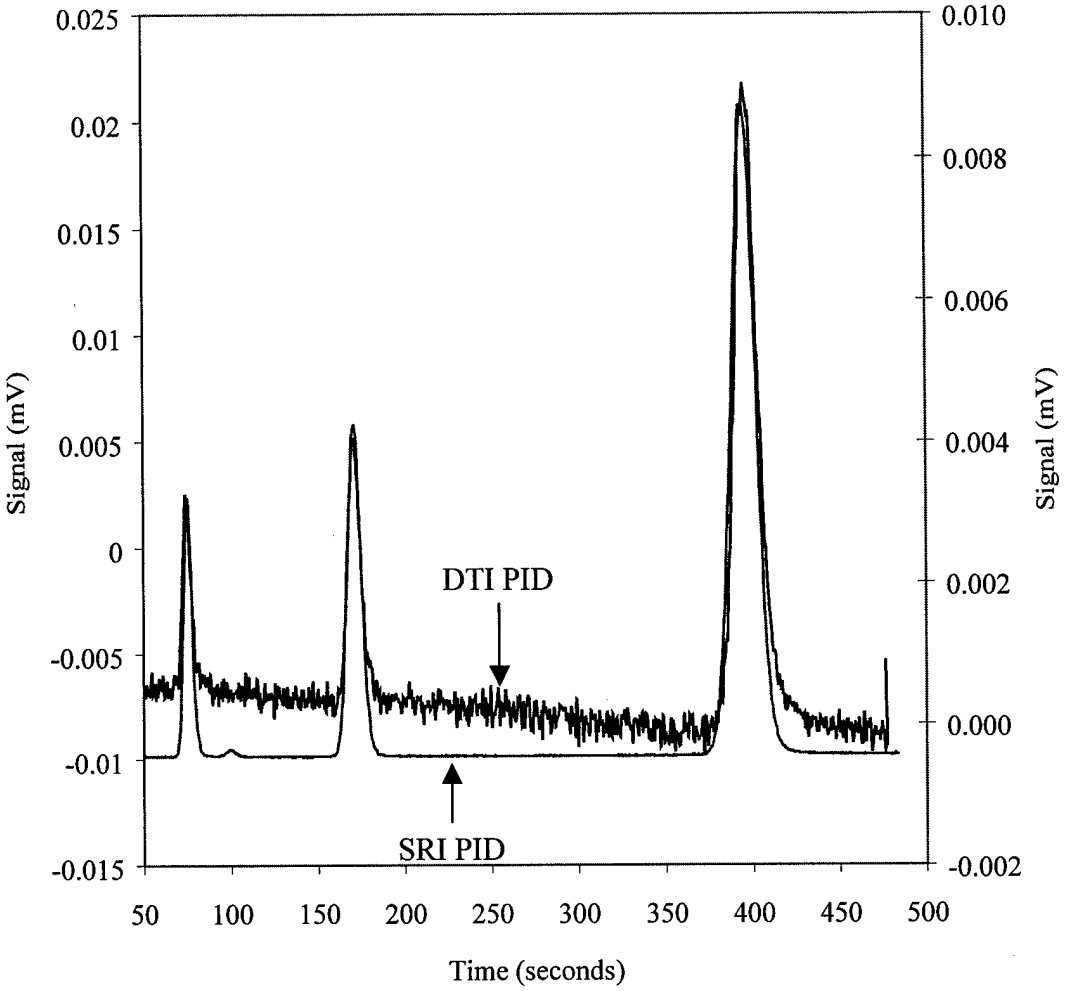

Figure 15. DTI PID vs. Commercial PID

One final issue that has been dealt with is removal of water vapor from the carrier gas stream. It was previously determined that using Nafion in conjunction with Drierite was adequate for drying the carrier gas/analyte stream (this system is used with the XSD). While this is true, ultimately the Drierite begins to drive its water back into the Nafion due to heating of the Drierite by the MIP. This posed a substantial problem during the field demonstration at Offutt AFB. To remedy the situation a small "tube within a tube" drying unit where dry carrier gas sweeps the water vapor away from the exterior of the Nafion and ultimately discharges to the atmosphere was engineered. Bench tests of the drier have revealed it is very effective.

To test the efficiency of the Nafion dryer system we used a flow cell to continually run water over the membrane for approximately two hours. We monitored the baseline signal and found no change other than a small (~3 mV) decrease in the baseline. Figure 16 shows the results of aliquots of 50-ppm toluene and water being applied to the membrane. At approximately 22 seconds, a 500-μL aliquot of the toluene solution was applied and a 500-μL aliquot of water was applied at approximately 60 seconds. A second aliquot of 50-ppm toluene was applied at 72 seconds. In previous versions in which a desiccant was used to trap the water vapor, there would

oftentimes be an obvious signal from the PID when water was applied to the membrane owing to the PIDs response to changing humidity.

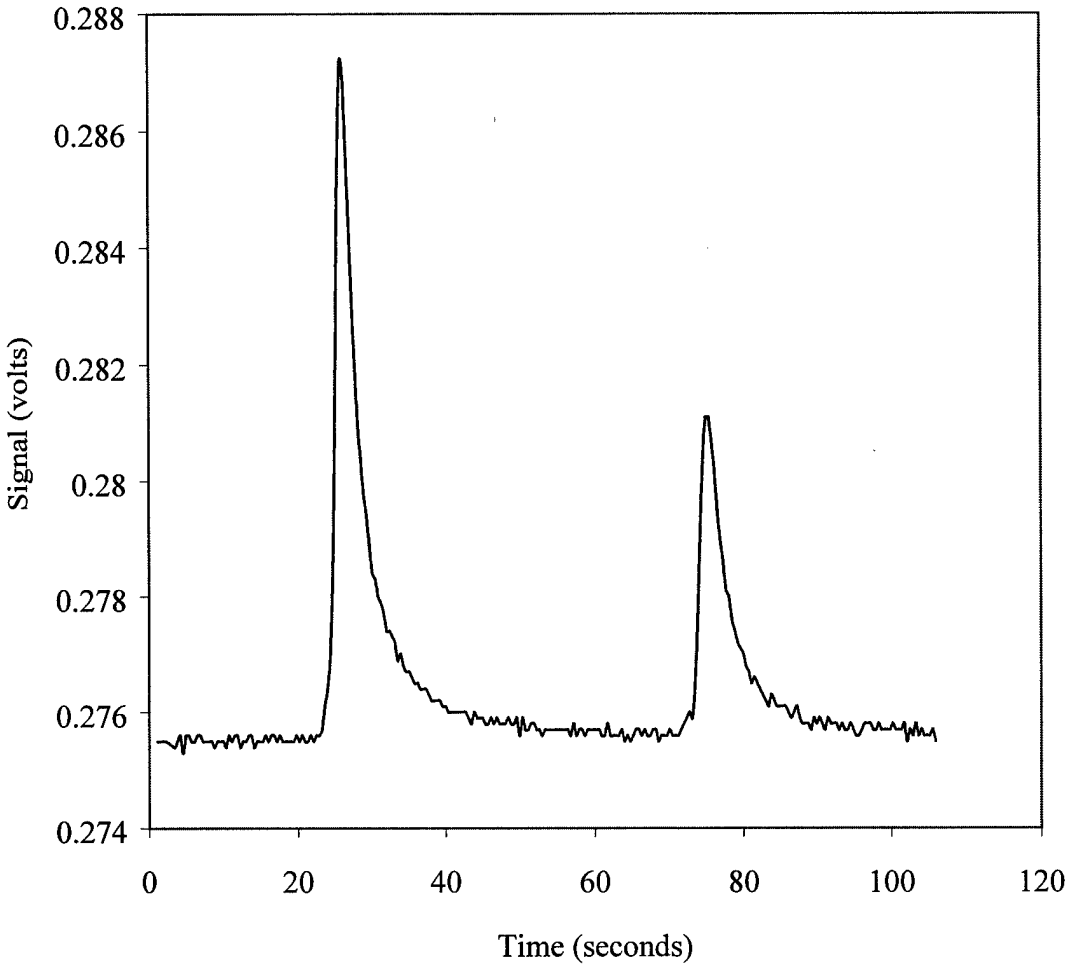

Figure 16. The PID response to 500 μL aliquots of a 50-ppm solution of toluene (22 and 72 seconds) applied to the MIP. At 60 seconds, a 500-μL aliquot of water was applied.

To test the long-term performance of the PID in its current configuration, it was started in the morning and operated all day. A dilute toluene solution was applied early in the run to determine that the PID was functioning. The results of the experiment are shown in Figure 17. The spike on the left of the graph is due to the test solution of toluene. Over the course of the day, the baseline drifted on the order of 3 mV and noise is on the order of 100 μV.

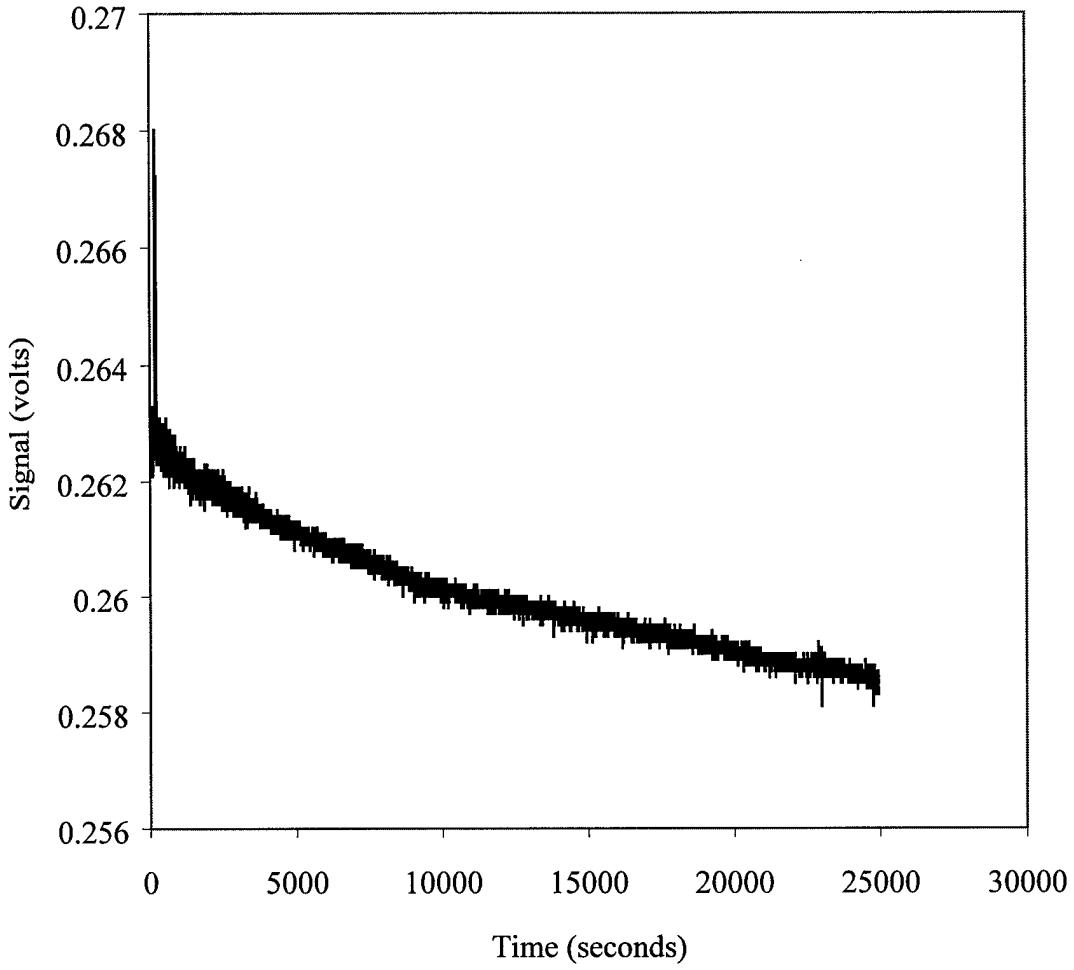

Figure 17. Day-long test of the PID's baseline drift

The ultimate tests for both the XSD and PID were their performance at real-world, contaminated sites. The following sections describe in detail the field studies and results for the XSD and PID during the course of this effort.

FIELD STUDIES

During the SERDP project, field investigations were conducted at several local test sites and at Offutt Air Force Base. Each of these sites was visited multiple times. The XSD field studies are summarized first, followed by the PID field studies.

XSD - Gas Stop Site (Moorhead, MN)

One site was a former drycleaners that had been converted into a convenience gasoline filling station. This site, the Moorhead Gas Stop, is in Moorhead, MN approximately 5 miles from DTI. The site is located approximately one-third mile east of the Red River, which flows north. The hydrodynamic flow of water is directed toward the northwest. DTI first arranged access to this local test site in the fall of 1999. It is now operated as a gas station and convenience store, but had previously been a dry cleaning establishment. During 2000 DTI made seven trips to the site to evaluate aspects of the experimental protocol and to test engineering issues related to sensor construction and durability.

Work by a local environmental consulting firm (Gemstar Environmental) had established that the subsurface is contaminated in different areas by PCE and gasoline with lesser amounts of TCE. Gemstar cooperated in arranging access to the site and providing site data. Eight monitoring wells are in place, with about 5 mg/L being the highest PCE concentration observed in any well. It is not known whether true DNAPLs are present at the site. When the business was operated as a dry cleaning facility, chlorinated solvents were stored behind the building on the east and south sides. The current fuel storage and contaminated areas are the west and north sides of the building.

We have used the Gas Stop site (1) to test for water blocking abilities of a gasket seal between the umbilical cable and the rod assembly, (2) to determine the best modalilty for understanding and correcting for temperature fluctuations of the XSD reactor core and its effects on the XSD signal in the field, and (3) to compare the results of downhole continuous sampling against continuous sampling in which the vapor is brought to the surface and analyzed with a stand-alone XSD.

Previous site characterization of the Gas Stop site has involved traditional GC measurements of volatiles from water well locations, along with PID readings from fresh soil borings. An independent testing laboratory, directed by an environmental firm, reported the values in Table 4. The values are from water samples taken from a well at the spot of greatest contamination (former PCE storage area).

Table 4: Concentrations (ppb) of PCE and TCE in Well #1 determined via GC

Date	PCE	TCE
2-17-99	5900	<0.30
5-25-99	9600	1.6
8-19-99	3600	1.6

Our initial goal was to employ the downhole XSD for chlorinated analyte detection and to compare our results to the data above. Our efforts included direct in-situ pushes of the XSD detector, along with purge-and-trap GC runs on soil boring samples. To access day-to-day performance of the XSD, we returned to the site several times in October 1999. During each visit, we "pushed" at well #1 to determine XSD performance at the same location. Subsequent XSD pushes occurred at other locations, often forming transects of the site. During all pushes, the XSD performed normally.

Soil samples taken near Well #1 were analyzed with a purge-and-trap GC at DTI. The results shown in Table 2 were obtained by removing one gram of material from soil cores at approximately 12 feet. These results (see Table 5) are based on a 1-gram sub-sample taken from a soil core at approximately 12 ft. Our motivation for undertaking purge-and-trap analysis of the soil cores was to relate the results to the in-situ XSD measurements of the site.

Table 5: Concentrations (ppb) of Soil Boring Samples Collected by DTI using GC

Detector	CH_2Cl_2	Benzene	TCE	Toluene	PCE
PID	NA	6.2	6.4	15.8	113
XSD	45.5	NA	1.3	NA	>>550
PID	NA	31.2	12.4	22.3	67
XSD	105.7	NA	7.1	NA	57
PID	NA	58	43.6	88	433
XSD	156	NA	8.1	NA	525

NA: Not Applicable

Figure 18 depicts a 0.5 cm/s push made near one of the wells with a relatively high PCE concentration (3.6 mg/L in August 1999). The repeatability of pushes made in the same area is very good. Data obtained by screening the soil cores uphole with a PID (from four years ago when the monitoring well was installed) are also in agreement. Data were acquired on a transect to show our ability to delineate the boundaries of the contaminant plume. The clay soils at this site are tight, so the plume has not migrated very far.

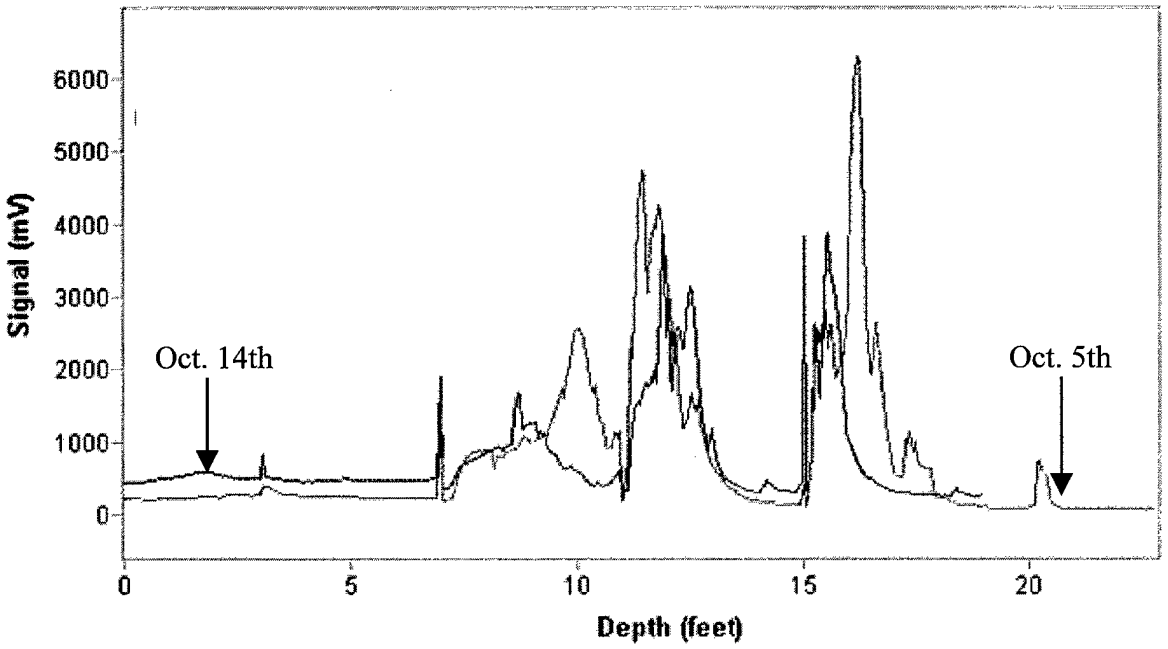

Figure 18. Replicate pushes of the XSD at the Gas Stop site, October 1999

XSD - Former Dry Cleaning Site (West Fargo, ND)

In January and February of 2001 DTI learned of another contaminated site (see Figure 19) in the area. This site, a former drying cleaning establishment, has been cited as the source for a major PCE contaminant plume. The PCE plume is headed toward a nearby river. DTI was asked by

the City of West Fargo and the North Dakota Department of Health to investigate the city property adjacent to the site.

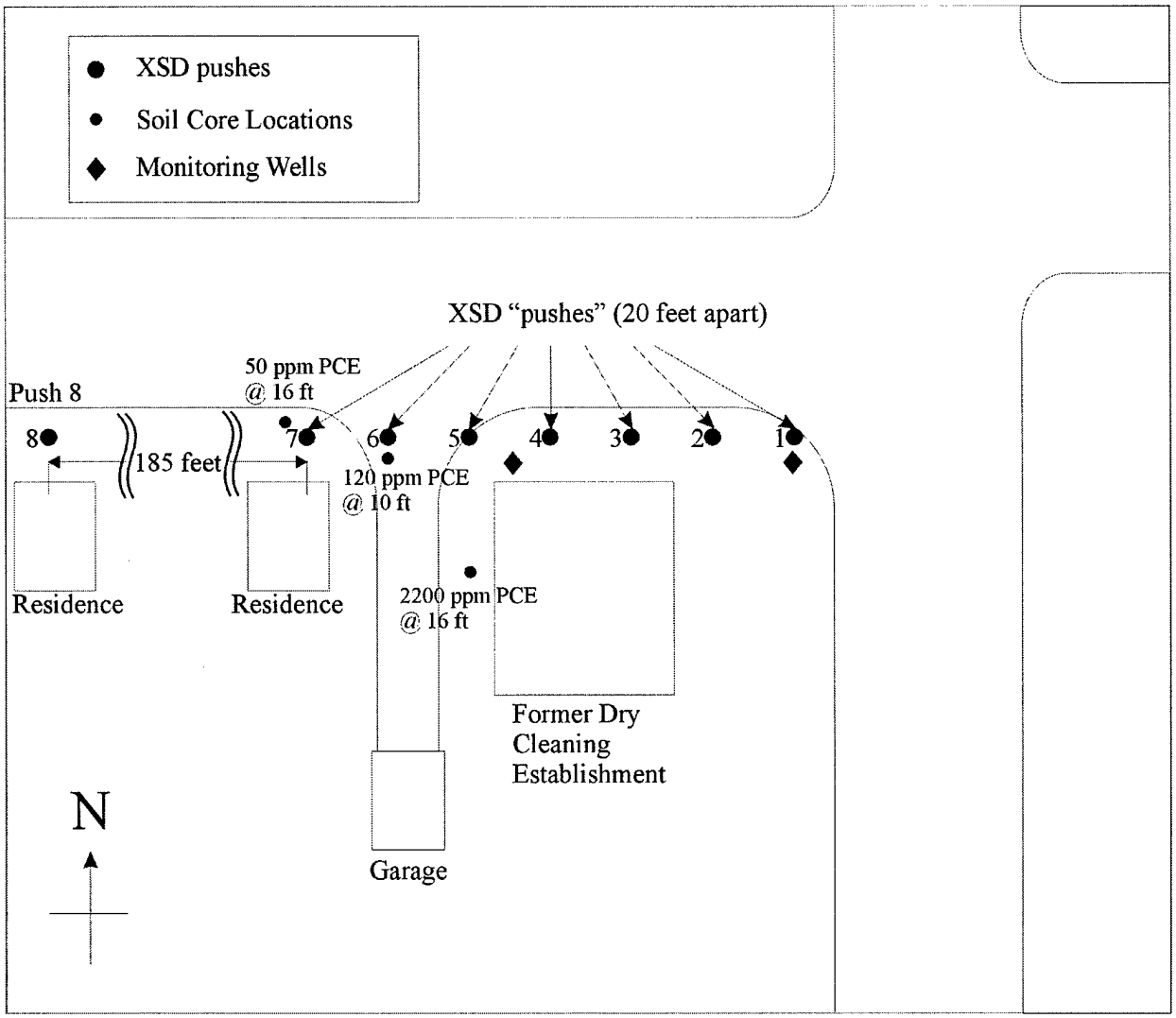

Figure 19. Map of former dry cleaning site (West Fargo, ND) showing locations of XSD pushes

On April 3 and 4, 2001, eight XSD probe pushes were performed on an east-west transect along the north side of the site. Figures 20 and 21 show the logs of the XSD response vs. depth for the eight pushes.

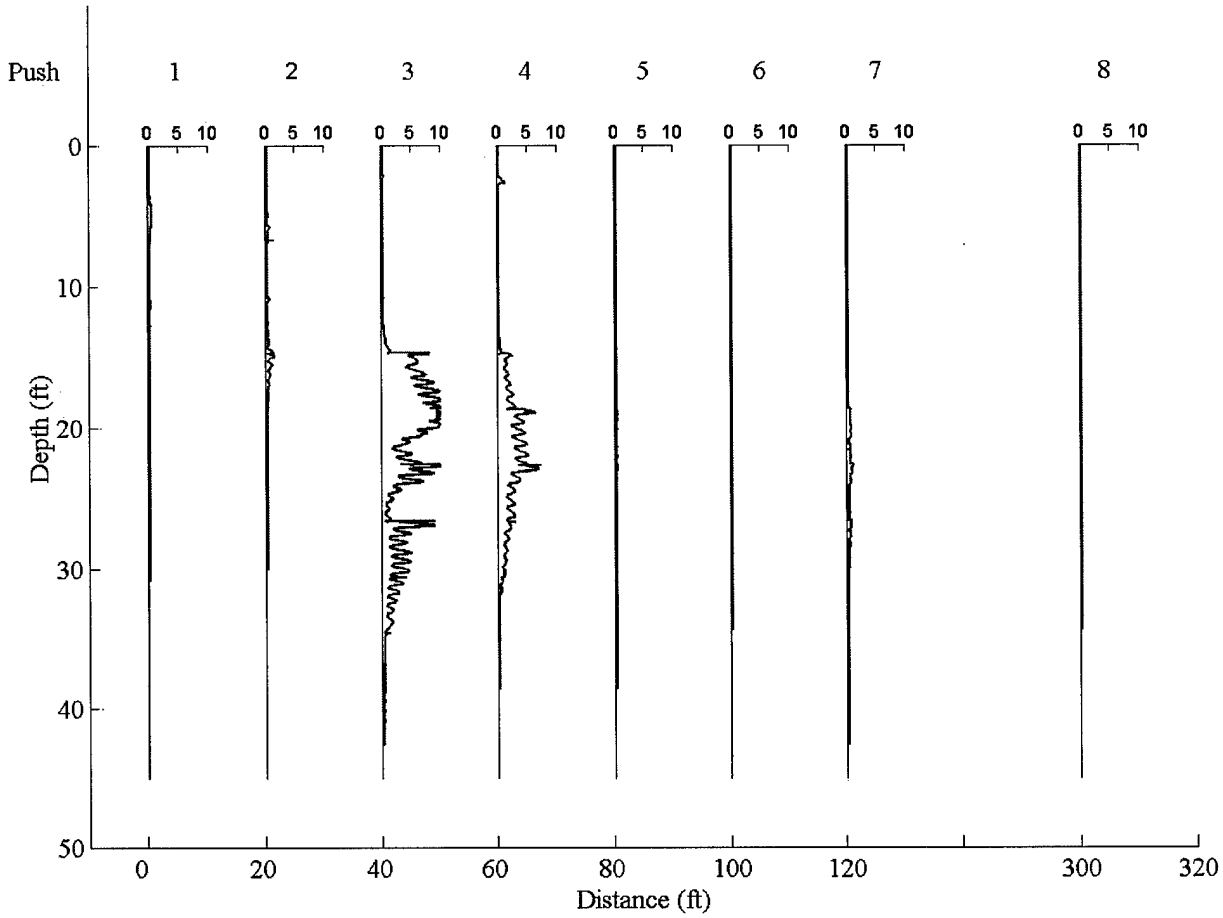

Figure 20. Field data from West Fargo former dry cleaning site. Collected with the XSD on April 3 and 4, 2001. The data are presented on a 0-10 volt scale.

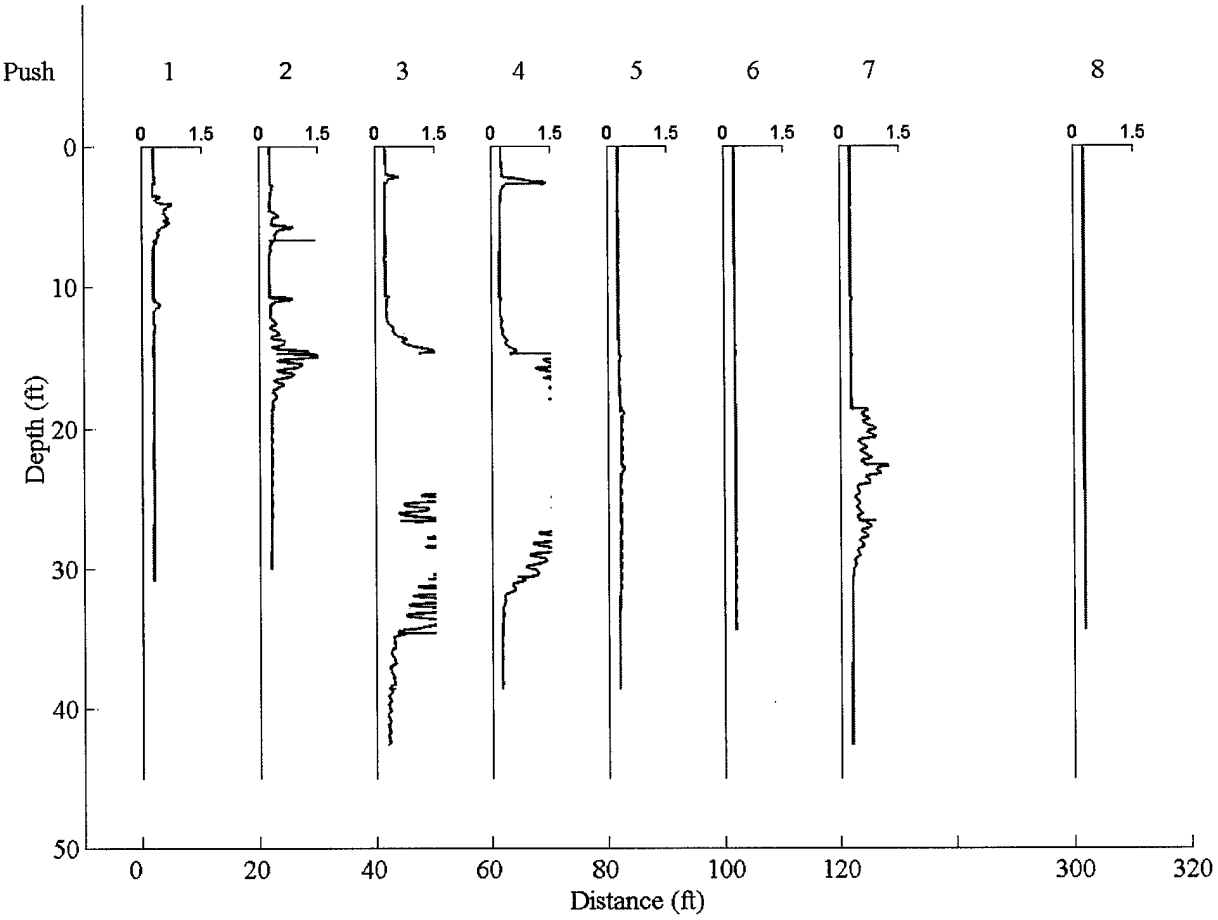

Figure 21. Field data from West Fargo former dry cleaning site. Collected with the XSD on April 3 and 4, 2001. The data are presented on a 0-1.5 volt scale.

The first seven pushes were spaced 20 feet apart and extend from the northeast corner of the dry-cleaning property (near monitoring well 2) to just a few feet west of the neighboring residential driveway. The eighth and last push was conducted 185 feet further west of push 7 in an area expected (and found) to be outside the contaminant plume.

The signals indicative of chlorinated solvent contamination are very low for pushes 5 and 6, but quite pronounced for push 7. These differences lead us to speculate that there may be two sources of contamination, one on the north side of the building and the other on the west. A series of pushes along the adjacent residential driveway and in the grassy space between the driveway and the dry-cleaning building would help determine if this is true.

Generally the further one probes west (and farther from the dry cleaning building), the deeper the contamination lies. In fact, if push 7 had been terminated at 16 feet, as with many of the previous soil borings, it would have been clean. This shows the unfortunate and hard-to-avoid arbitrariness of soil borings: How deep do you go before you conclude there is not another, deeper zone of contamination? We see this as one of the great advantages of our technology. It's easy to add another rod or two and keep measuring, just to be sure.

We were not able to collect enough data to determine the degree to which the plume underlies the neighboring residence. One could continue along the transect to see if concentrations were still increasing to the west of push 7.

There are other points to keep in mind as one examines the data. The XSD response, expressed in volts, can be used to gauge the relative amount of contamination at the various push locations and as a function of depth below ground surface. Data of this nature can be used with confidence to locate hot spots, to define plume boundaries, and to draw plume contours. Furthermore, one can note that the response of the XSD exhibits an obvious oscillatory behavior. These oscillations are related to the regular swings in the operating temperature of the MIP (130± 15 °C). At the lowest point in the cycle, the temperature of the MIP was lower than the boiling point of PCE (121 °C). At this temperature, PCE becomes embedded in the MIP's Teflon coating. As the temperature rises, the embedded PCE is transported through the MIP membrane into the carrier gas stream. By raising the setpoint of the MIP so the lowest point of the oscillation is above PCE's boiling point, these oscillations can be reduced or eliminated.

XSD - Offutt Air Force Base Site (Omaha, NE)

In September 2000 the XSD sensor was field-tested at Offutt Air Force Base near Omaha, NE. Offutt was an ideal location to check the field ruggedness of our sensors, since it has both chlorinated and fuel contamination. This site provided a variety of soil types, water table depths, and contamination scenarios in which contamination concentrations and spatial distribution vary widely. Another advantage of the site was the ability to cost-share the expense of the first field study with a concurrent AFCEE contract at DTI whose work plan included field demonstration of current DTI technology. In anticipation of the site's more gravel-like, porous soil and low water table (10-13 feet) the last 10 feet of the umbilical cable was coated with polyurethane. However, during the second XSD push, water inundated the rod sections to a point above the polyurethane and seeped through the uncoated portion of the umbilical cable. The water then passed down through the cable and electrical connections, ultimately making its way to the XSD housing and causing a catastrophic failure of the sensor.

After the first field trip, an umbilical cable was completely coated with polyurethane. The XSD with the new umbilical was field tested at Offutt AFB February 15-17, 2001. Water intrusion was completely eliminated with the new cable. A detailed description of the field study follows.

Data collection procedure

Data were collected using the XSD/MIP system and a Geoprobe percussion delivery vehicle at Offutt Air Force Base's old jet engine test stand (OJETS). The Geoprobe vehicle was operated in push mode to continuously advance the sensor into the ground at 0.5 cm/sec. All pertinent information for each push was collected with a PC and DTI's in-house software. The software simultaneously collects MIP temperature, XSD temperature, time, depth, and XSD signal. To allow the user to immediately see the results of the push, as the probe is advanced, the software plots XSD signal versus depth and MIP temperature versus depth. A total of 383.24 feet were logged over a two-day period. The number of feet pushed on day one (156.34 feet) was less than on day two (226.9 feet) because of the initial setup time required. Also, day one involved about one hour of downtime after the probe was accidentally pounded. Six hours were spent actually pushing the XSD on day one. On day two, the sensor was pushed for eight hours, with one hour spent warming up the sensor assembly. The total time required to perform the 12 pushes was 36 man-hours (two DTI personnel at 18 hours each).

Twelve pushes were completed, to a maximum depth of 38 feet below ground surface. The pushes were done in a line parallel with a monitoring well cluster in a north to south direction.

The first two pushes were done near monitoring well cluster 2 to determine whether the instrument was working properly. Push 1 showed contamination at 8, 17, and 20-25 feet. Push 2 was done approximately 1.5 feet to the north of push 1 to provide a replicate push for comparison. However, at approximately 2 feet the operator accidentally pounded the probe,

which caused the XSD to become unstable, resulting in noise spikes in the signal. The probe was extracted and the push was subsequently abandoned to allow the XSD time to recover. After approximately 45 minutes push 2 was attempted again. This push showed contamination zones at 7, 9, 13, and to a lesser extent at 24 feet. The data did not show a high degree of repeatability between pushes 1 and 2; likely caused by the instability previously mentioned.

Pushes 3 through 12 were done to form a transect of the OJETS contamination plume. A map of our pushes with respect to monitoring well cluster 2 is shown in Figure 22. The main area of contamination is between pushes 6 to 9, seven feet west of monitoring well cluster 2 (see Figure 23). See Appendix B for logs of each push.

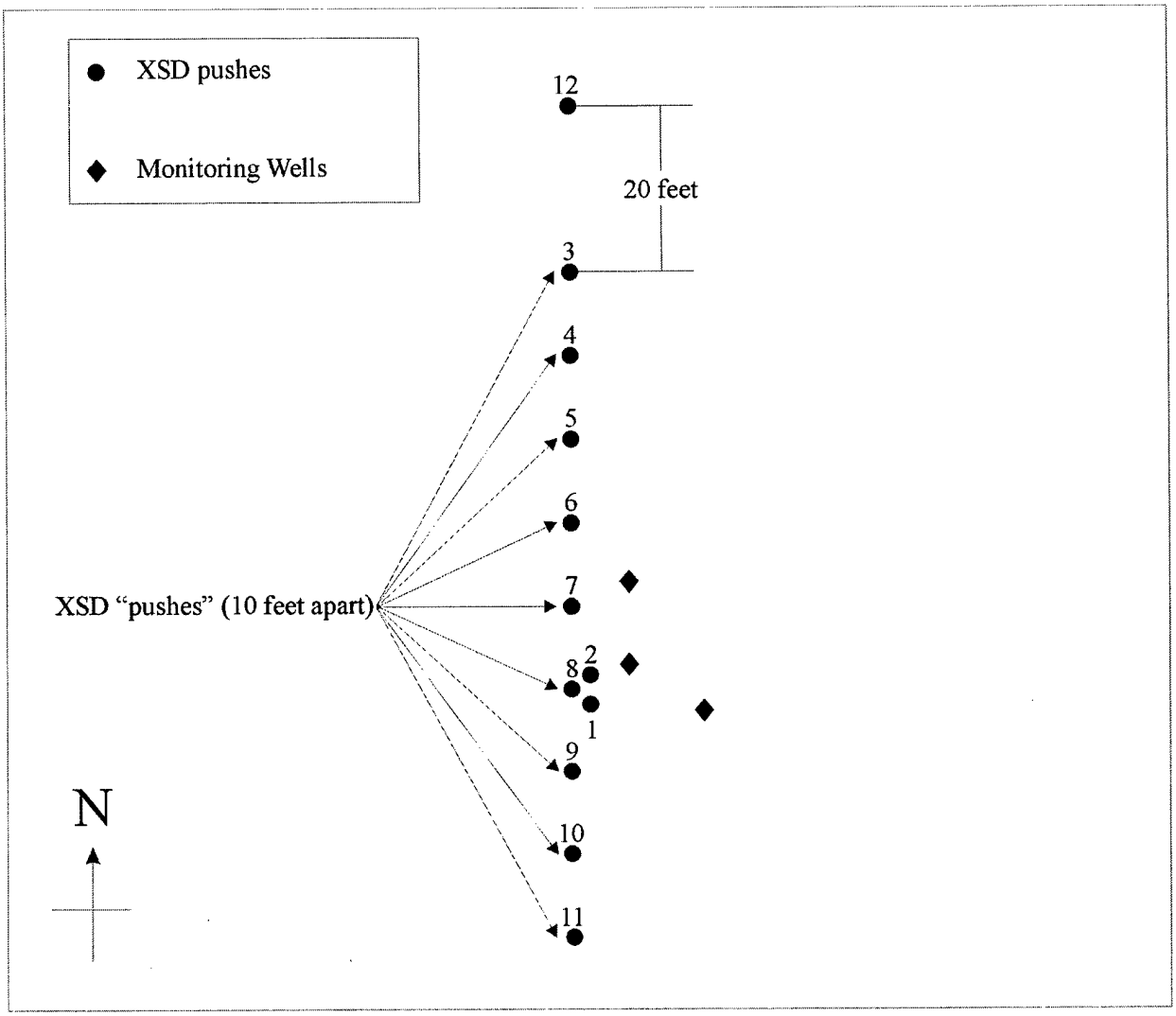

Figure 22. Map of OJETS site, Offutt AFB, showing locations of XSD pushes

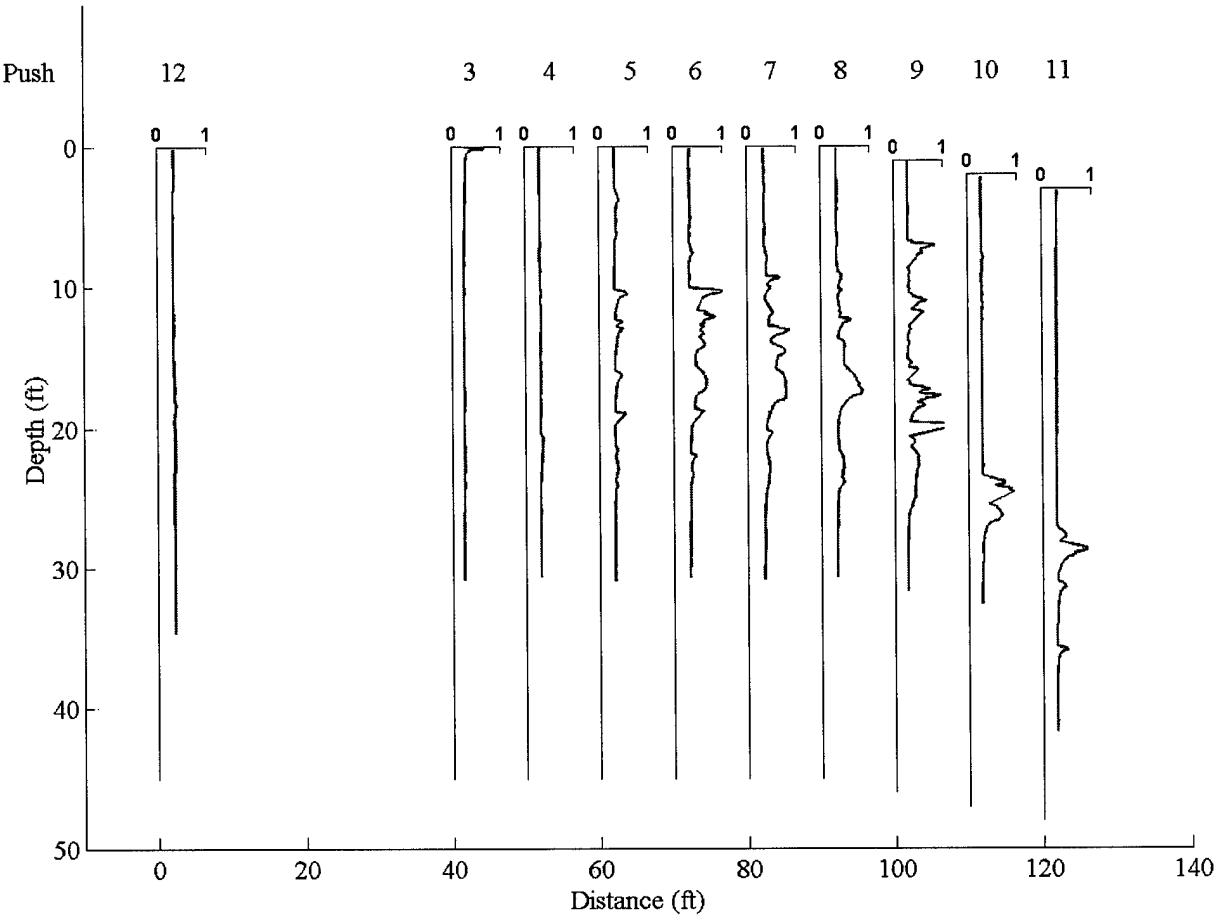

Figure 23. Field data from OJETS site, Offutt AFB. Collected with the XSD on February 15 and 16, 2001. The data are presented on a 0-1.0 volt scale.

Data analysis

Analysis of the data consisted of two main components, normalizing the XSD baseline and removing erroneous data during rod changes. Each will be discussed separately. Due to the high temperatures of the XSD sensor and the cooling ability of the earth, some temperature fluctuations are seen when the XSD is advanced into the ground. Since the XSD baseline signal is directly related to the XSD temperature, baseline fluctuations of 30 to 80 millivolts are common. However, since the XSD temperature is recorded, the data can be corrected to one temperature thus reducing baseline fluctuations to 20 millivolts or less.

The second portion of the data analysis was to remove any erroneous data due to the XSD sensor being stopped during rod changes. If a rod change occurs in a contamination zone, the XSD signal sharply rises then decays to baseline. The XSD signal remains at baseline levels until the sensor has moved at least another 10 to 18 inches. As the sensor remains stationary, the hydrostatic pressure around the sensor lessens as the ground comes into equilibrium. This pressure phenomenon is well understood and forms the basis for the hydroconductivity sensor commonly employed on cone penetrometer trucks. In our case, the tip of the MIP is 10 inches below the actual membrane. To remove any erroneous data caused by the stoppage of the probe during rod changes, all data are removed from the point at which the sensor stops to 10 inches after the sensor begins to move again. The actual amount of perturbed soil may be greater than

this —as evidenced in pushes 7, 8, and 9 —but for this transect data only 10 inches were removed.

Data comparison

A comparison of our data with that of soil and water samples collected by URS Greiner Woodward Clyde (URS) was undertaken to identify any correlation. The URS data was collected over a two-month period from March 13-14 to May 17, 2000. The method for correlating our pushes and those of URS was to choose URS points that were close to our push locations. Since the URS data was collected at discrete depths and our data was collected continuously, to correlate our data the XSD signal was averaged over the depth range collected by URS. To obtain a signal representative of only chlorinated contamination, an average of the baseline signal was subtracted from the averaged XSD signal. The region that best represented a baseline region was the last foot of each push. Our averaged values were then plotted against the concentrations provided by URS. The correlation between data collected with our sensor and that collected by URS is shown in Figure 24. There is good correlation between the data; only one point deviated substantially from the rest. This point corresponding to a concentration of 1490 ppb collected at approximately 8 feet corresponded to a very low signal level on our data. However on reviewing the push (push 8) where this point was taken, a contamination region can be seen approximately 1 foot lower than that used for our averaged values.

Our data and the URS data share many similarities, including:

- High level of contamination at 15-18 feet
- Moderate level of contamination at 20-25 feet
- Lower level of contamination at 3-5 feet
- Moderate level of contamination at 8 feet
- Shallow (above 25 feet) contamination very low at southern end
- Low level of contamination at 20-25 feet at northern end

The only major difference between our data and that of the URS data is a deep (below 25 feet) contamination region (1 to 2 ppm) at the southern end of site.

This difference is attributed to the lack of URS data south of monitoring well cluster 2. Data from previous water samples did not show any significant contamination below 25 feet. The location of this deep contamination zone corresponds to the direction of water flow, so the migration of the contamination plume to the southeast is reasonable.

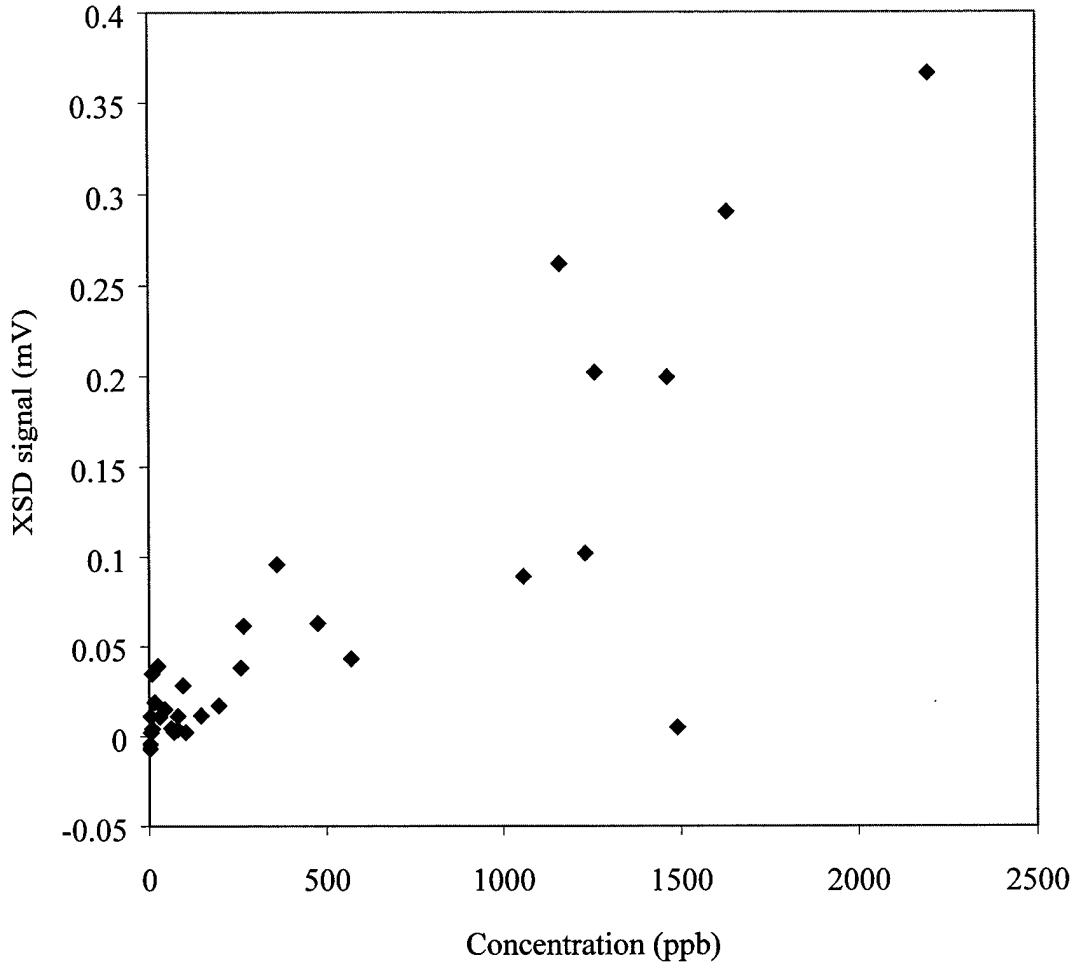

Figure 24. Correlation of URS' total chlorinated concentration data versus averaged XSD signal data

XSD - Conclusions

The goal of this research was to identify, develop, and field test vapor detectors that could be operated downhole in close proximity to Geoprobe's MIP. The criteria for the sensor were:

- Highly sensitive and specific for chlorinated hydrocarbons
- A gas phase measurement to minimize or eliminate matrix effects
- Better depth resolution than techniques that draw vapors to the surface
- Delivers logs similar to those provided by LIF for fuels

In the proposal, we suggested three modified GC detectors: a thermionic ionization detector (TID), a photoemissive electron capture detector (PE-ECD), and a photoemissive ion mobility spectrometer (PE-IMS). Early in the contract, our attention was directed to the halogen specific detector (XSD) available from OI Analytical, which, like the TID, relies on a high temperature combustion process. However, the XSD is much less demanding of the carrier gas properties than the TID. In addition, our experiments showed that the TID performance tended to degrade fairly rapidly. Once we established that the XSD was both more sensitive and more stable than the TID, it was adopted as the detector of choice.

An initial XSD was constructed to demonstrate downhole feasibility. This XSD was deployed at a local site where dissolved phase PCE was known to be present. The initial tests indicated that the XSD could detect chlorinated VOCs in the subsurface.

Several subsequent modifications were made to the downhole XSD system to improve its performance, including: a Nafion drying module to remove any water vapor passing through the MIP, a means to actively monitor and stabilize the XSD temperature, miniaturization of the assembly to fit within a 1.25 inch I.D. pipe, and a water block and coated umbilical cable to eliminate water intrusion into the system.

Concurrent with the XSD modifications, numerous experiments were conducted in the laboratory to determine the XSD's specificity and sensitivity. We determined the XSD's specificity to be greater than 10000 to 1 for chlorinated hydrocarbons relative to non-chlorinated hydrocarbons. This level of specificity is approximately double that of our initial claim.

The XSD's sensitivity was studied both in the laboratory and in the field. The XSD's sensitivity in the laboratory was found to be 10 ppbv for both TCE and PCE. In the field, the sensitivity of the XSD was found to between 100-400 ppb. This value is dependent on two factors: the soil type, and, more importantly, the membrane of the MIP. These values still fall within our target range of low μg/L levels of detection for chlorinated compounds.

The advances made in the development of the XSD culminated in several field tests with the XSD; the most extensive of these occurred at Offutt Air Force Base (Omaha, Nebraska) in February 2001. Twelve pushes were done to an average depth of 30 feet in a two-day period. The logs were printed out in real time before the rod extraction for each push was completed. Depth resolution for all of the pushes was less than 1 inch. The logs generated were similar to LIF data and provided better depth resolution than techniques that bring the vapors to the surface (resolution greater than 6 inches). The results of this field study clearly demonstrated that the XSD could be used to effectively map dissolved phase plumes of chlorinated contaminants.

As with all research projects, questions still remain, particularly pertaining to the effectiveness of the XSD for mapping DNAPLs. The XSD was transitioned to an ESTCP funded project, along with two optical sensors, to collect additional data that will demonstrate its ability for real-time delineation of DNAPLs. However, results to date indicate that the downhole XSD will be an invaluable tool for the detection and delineation of subsurface chlorinated VOC plumes.

PID - Trucker's Inn Site (Glyndon, MN)

In early June 2001, the PID was deployed at the Trucker's Inn near Glyndon, MN, which has mixed fuel contamination. The area the PID was deployed had been contaminated with diesel fuel. Five pushes were made at four locations (see Figure 25). A monitoring well (MW 5) served as the reference point, with the four locations approximately 50 feet apart on a straight line heading west. A recent analysis of MW 5 had revealed free diesel fuel on top of the water. Figures 26 and 27 show the PID response versus depth for the five pushes.

The first PID push displayed a very small signal at 13 feet. The boring log taken when MW 2 was installed (handheld PID and bag headspace) showed a weak signal (5 ppm) from 15 to 20 feet. The PID signal may be representative of this result.

The second push was essentially featureless. Unlike other pushes that displayed a marked reduction in MIP temperature when the water table was encountered, this push did not. The reasons for this difference are unknown.

The third push, approximately 50 feet from MW 5 displays an artifact at 11 feet. This was caused by a failure in communication between the data acquisition program and the depth control acquisition module (DCAM). The system had to be restarted therefore the probe sat in the ground for a protracted period of time and may have perturbed the surrounding soil or baked a mud layer on the MIP. Weak features are seen at 17 and 21 feet.

The fourth and fifth pushes were performed very near MW 5. The fourth push was aborted at 16.25 feet when a layer was encountered that could not be penetrated by pushing. There is a very strong signal at 14 feet. The probe was extracted and moved a few feet for the fifth push. A similar hard zone was encountered during this push and the PID was hammered through the zone. The PID was electronically saturated (signal greater than 5 volts) during the push. The long tailing is believed to be caused by diesel fuel baking off of the membrane.

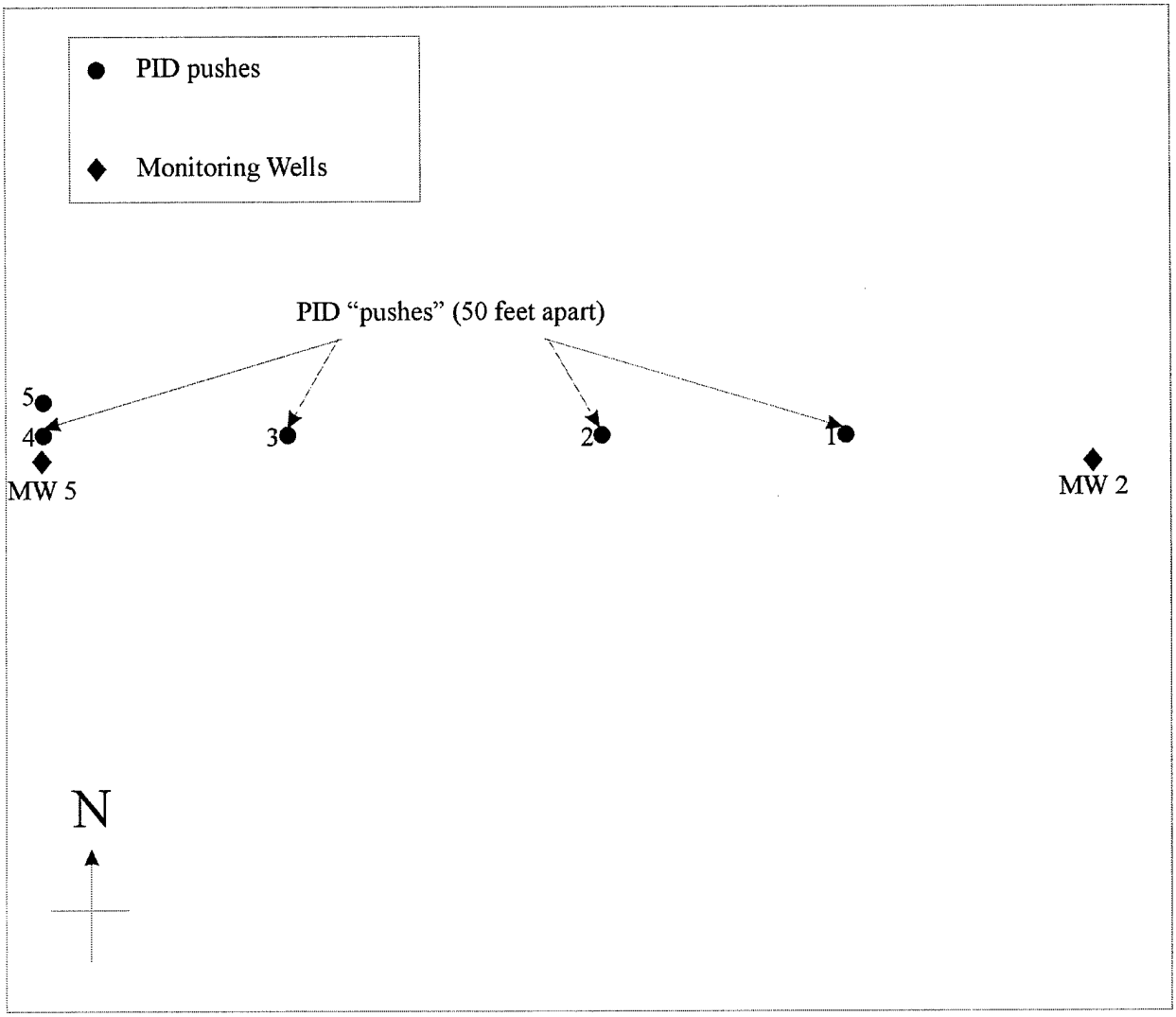

Figure 25. Map of Trucker's Inn site, Glyndon, MN, showing PID pushes

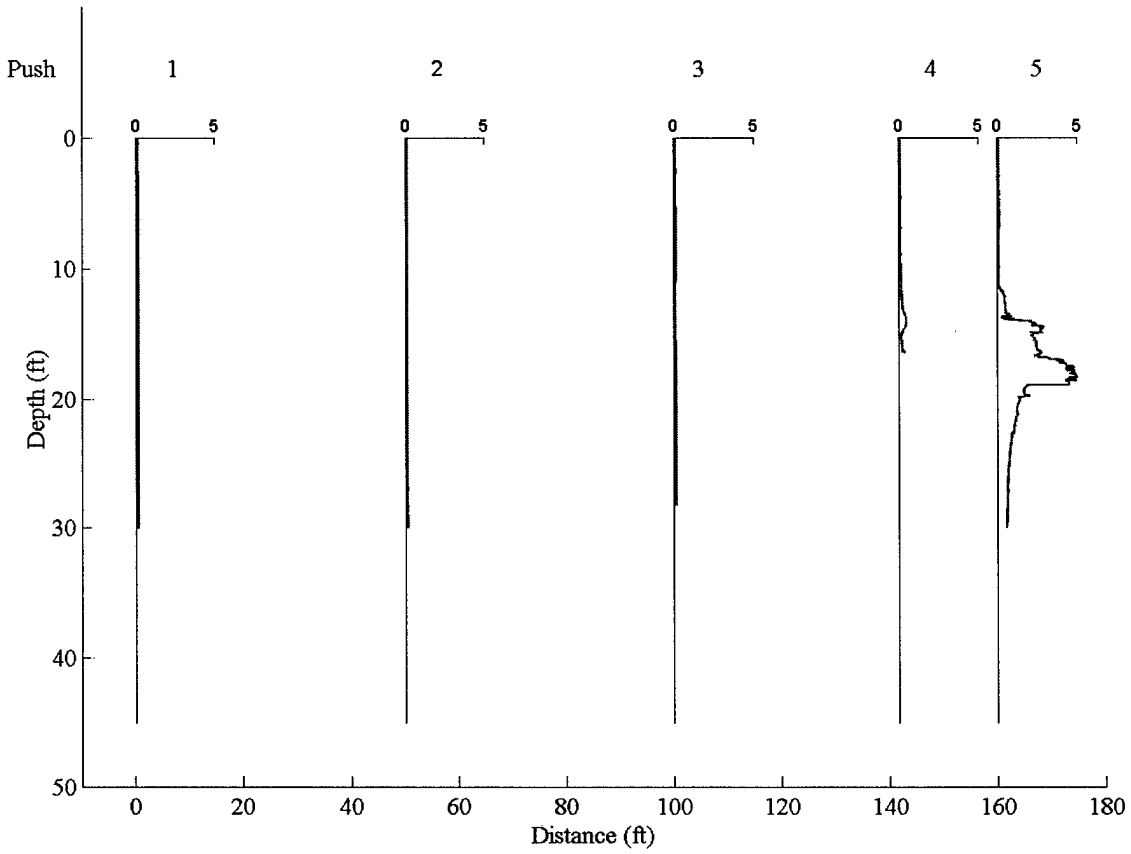

Figure 26. Field data from Trucker's Inn site, Glyndon, MN. Collected with the PID, June 2001. The data are presented on a 0-5 volt scale.

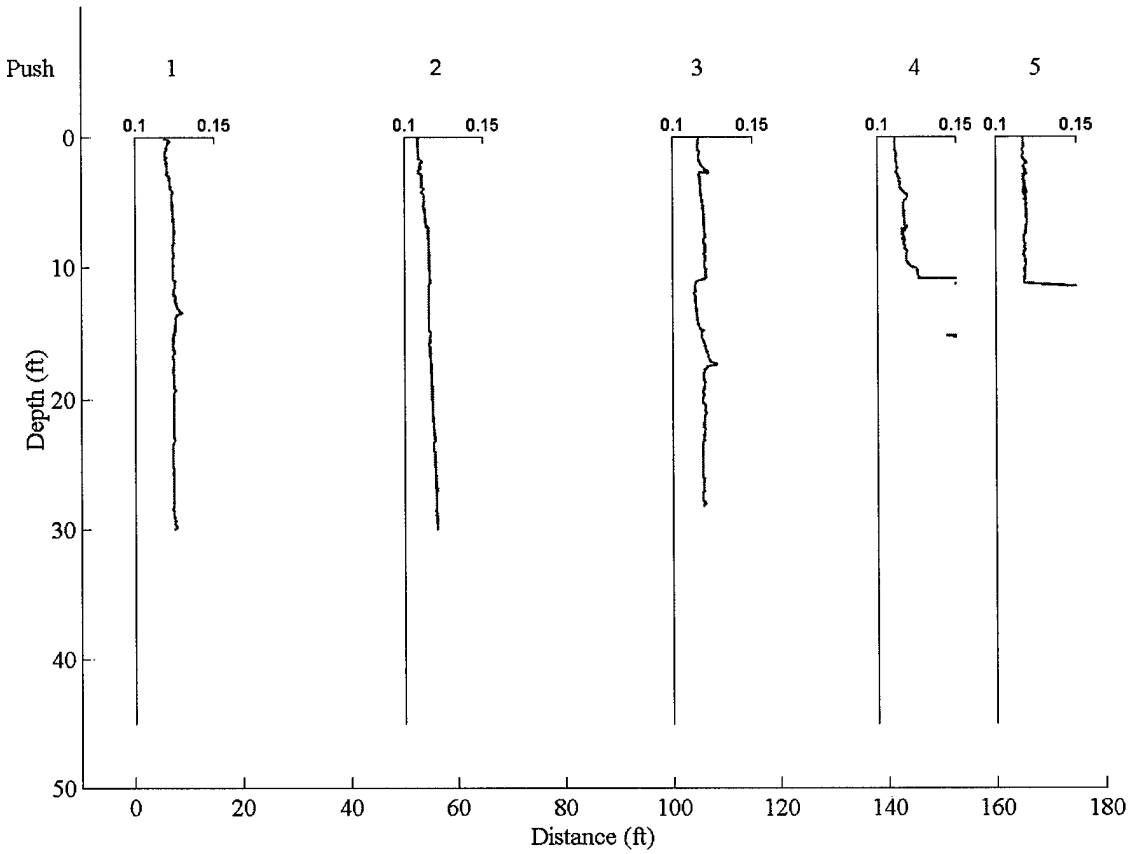

Figure 27. Field data from Trucker's Inn site, Glyndon, MN. Collected with the PID, June 2001. The data are presented on a 0.1- 0.15-volt scale.

PID -Former Leaking Underground Storage Tank (Enderlin, ND)
June 2001, the PID was deployed in Enderlin, ND at a site where a leaking underground storage tank for diesel fuel had been removed. A map depicting structural features and push locations is shown in Figure 28. Based on the location of the site relative to the Maple River, it is presumed that the groundwater flows primarily west and slightly north. The site had been previously characterized using laser-induced fluorescence (LIF) to delineate the free-product plume. Two of the LIF logs are shown in Figure 29; the logs are plotted on the same scale to show the relative strength of each signal. Log LIF 1 was collected when the probe was deployed outside the area where the tank had been and LIF 3 was collected in the center of the tank excavation area.

Because this site was on rolling terrain, the depth of some observed features appear to be different. Logs of the six pushes are shown in Figure 30 and 31. The first push was performed in an area expected to be free of contamination. We were unable to probe past 15 feet. This log displays a broad feature in the vadose zone that may be due to contaminant vapors in the soil gas or possibly naturally occurring vapors.

The second push had the same vadose zone features as the first and also reveals some very weak features between 16 and 17 feet. Based on observations of the MIP temperature variation, it appears that groundwater was encountered approximately 8 feet below ground surface. At approximately 19 feet, the probe entered a gravel zone where there was a relatively strong signal.

The third push, directly downgradient from LIF 3, showed a feature at 10 feet. Based on the vertical displacement of this site relative to LIF 3, this feature is likely due to a strong free-product band. This push also shows some features between 16 and 17 feet that are more intense than those in push 2.

The fourth push, made at a slightly higher elevation than the third, showed features that likely have similar origins as those in push 3.

The fifth PID push was performed within 3 feet of LIF 1. LIF did not reveal any significant contamination in the area. The PID displayed a modest signal between 16 and 21 feet.

The sixth PID push, on the edge of the excavated area, had a very large signal. The push was terminated at 18 feet when the data acquisition system lost communication with the DCAM. When the rods were extracted from this hole they exuded a strong smell of diesel fuel.

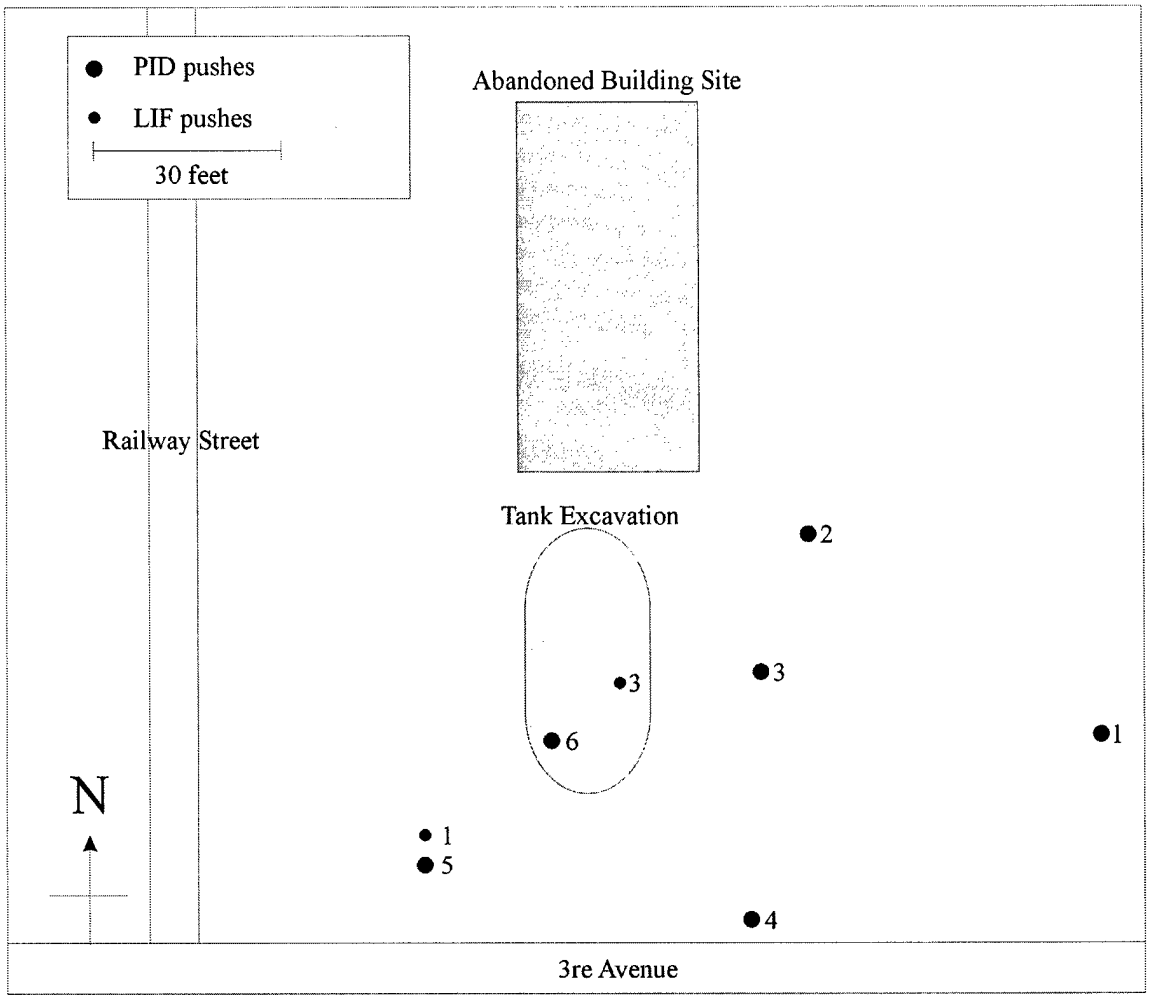

Figure 28. Map of former underground storage tank site, Enderlin, ND, showing PID and LIF push locations.

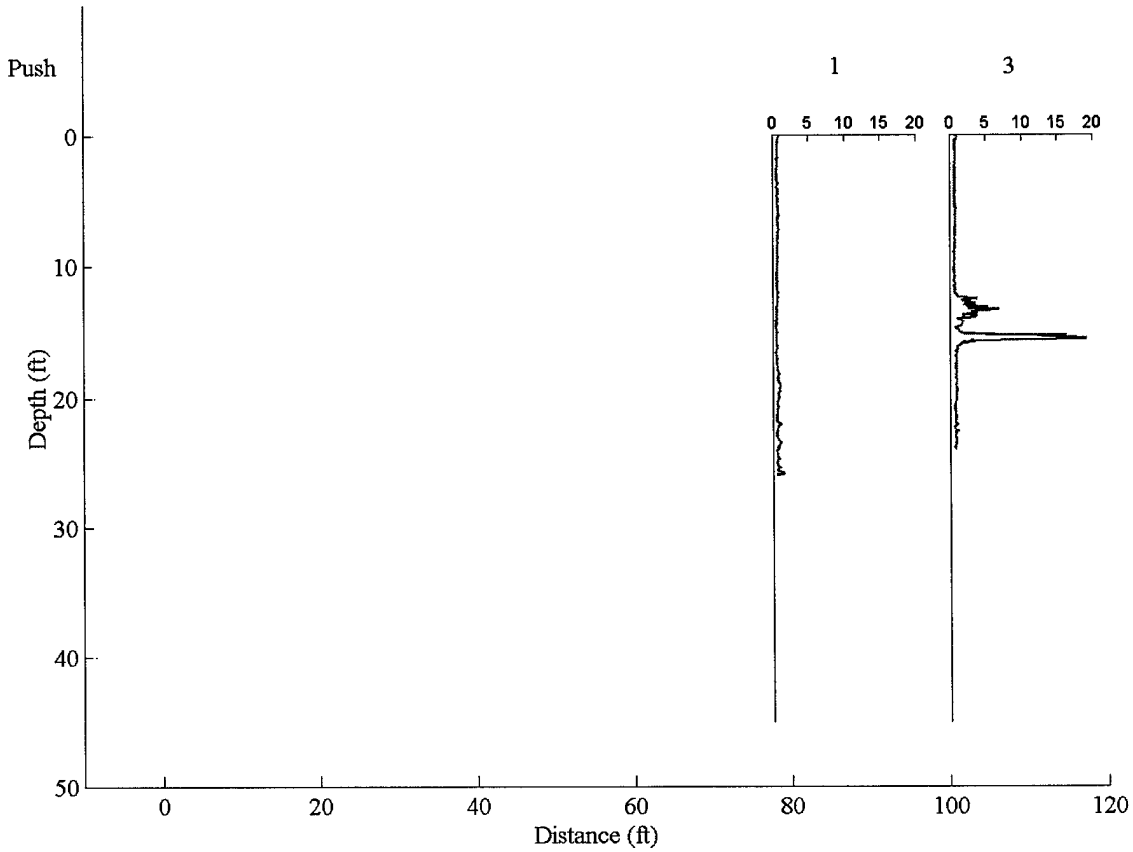

Figure 29. Field data from Enderlin, ND site. Collected with the LIF, June 2001

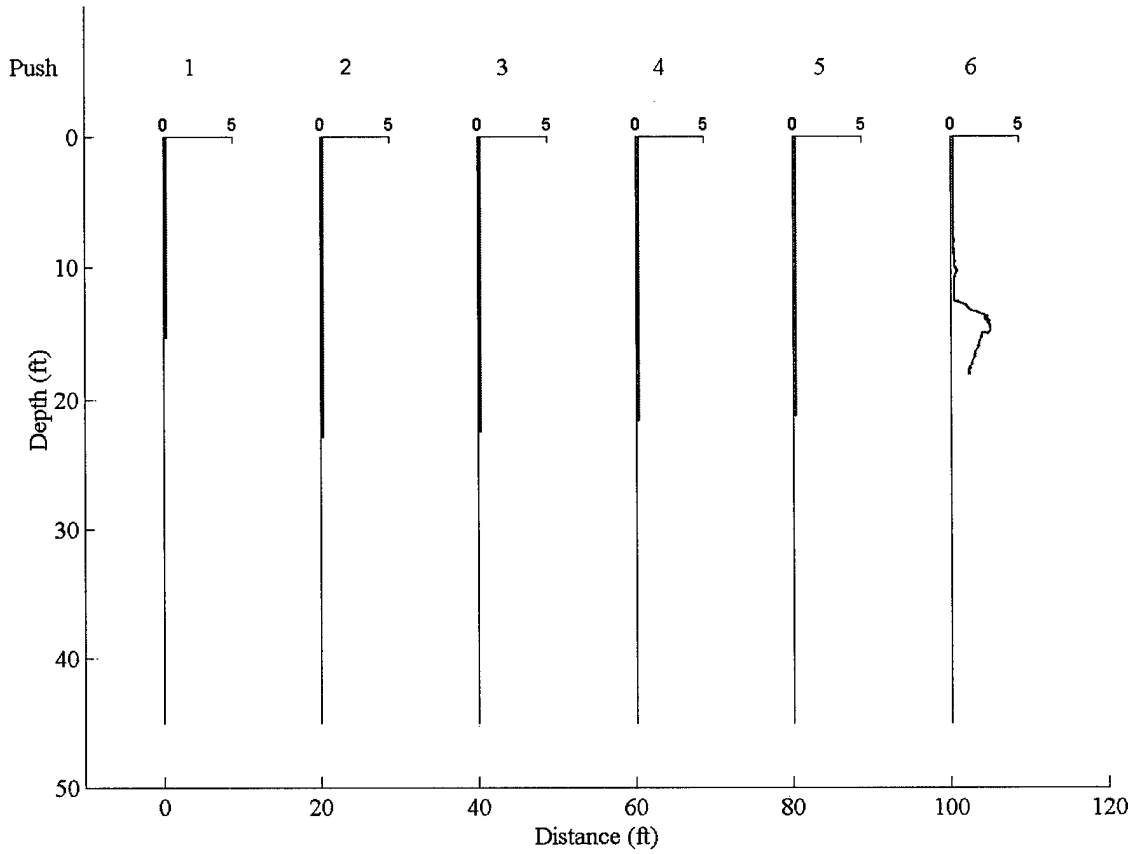

Figure 30. Field data from Enderlin site. Collected with the downhole PID on June 26, 2001. The data are presented on a 0-5 volt scale.

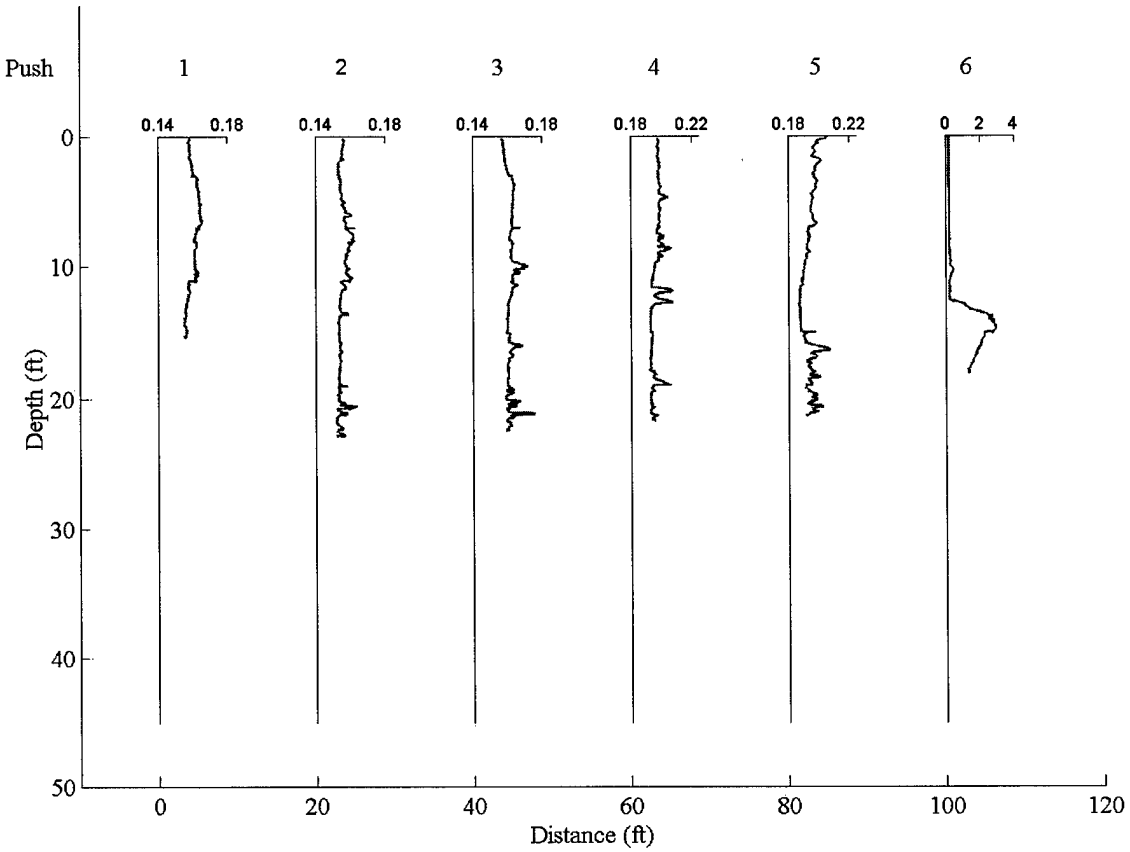

Figure 31. Field data from Enderlin site. Collected with the downhole PID on June 26, 2001. The data are presented with an automatic scale.

PID–Former Dry Cleaning Site (West Fargo, ND)

The PID was deployed June 28, 2001, at the same former dry cleaning site in West Fargo as the XSD. (A detailed description of the site and map are provided in the XSD section of this report.) Data gathered at the site are shown in Figure 32 (constant scale to show relative changes) and Figure 33 (autoscaled to show more detailed features). The first three PID pushes were done near the second XSD push. The XSD had displayed marked oscillations in the signal between 11 and 19 feet and the PID mimicked these oscillations on the first push. It was hypothesized, that since these oscillations directly corresponded with oscillations in the MIP temperature, the relatively high-boiling point PCE was being trapped on the membrane and only came across well at higher temperatures. To test this hypothesis, the MIP temperature was set to 150 °C for the second push (compared to 130 °C for the first). This temperature increase minimized some of the oscillatory behavior. A third push in the same area was performed with the MIP temperature set at 180 °C, which nearly eliminated the oscillations between 11 and 19 feet. The strong feature in Push 3 between 6 and 8 feet is likely an artifact. During the push, the encoder on the DCAM (which provides depth information) malfunctioned and the push had to be paused while the system was restarted. It is believed that, during this pause, the MIP more thoroughly heated the surrounding soil and drove more VOCs into the vapor phase for detection.

The fourth PID push was done in the same area as the fourth XSD push. This location was chosen since it had given a relatively moderate XSD signal. The MIP temperature for this push was 180 °C. The PID replicated the shallow feature around 2.5 feet that had been displayed by the XSD. From 15 to 35 feet, the PID displayed a strong signal (the spikes at 15, 19, 23, 27, and 31 feet are due to local heating of the soil that accompanies rod changes). In contrast to the XSD, which displayed an oscillatory signal that tracked with MIP temperature, the PID signal was not oscillatory. In fact, often the signal was increasing while the MIP temperature was decreasing. This was viewed as a very exciting result since it appeared that the hypothesis about the relationship between MIP temperature and oscillatory signals was proven.

The fifth push was a blank push. The fine scale (Figure 33) shows that there was clearly a low but oscillatory signal. The sixth PID push was made in the area of the third XSD push. The XSD displayed strong oscillatory signals (saturated) in this area. The PID signal was extremely oscillatory and the oscillations were in phase with the MIP temperature oscillations. The strong signals (15, 19, 23, and 27 feet) occurred only at rod changes where the PID push was paused and the MIP more efficiently heated the surrounding soil.

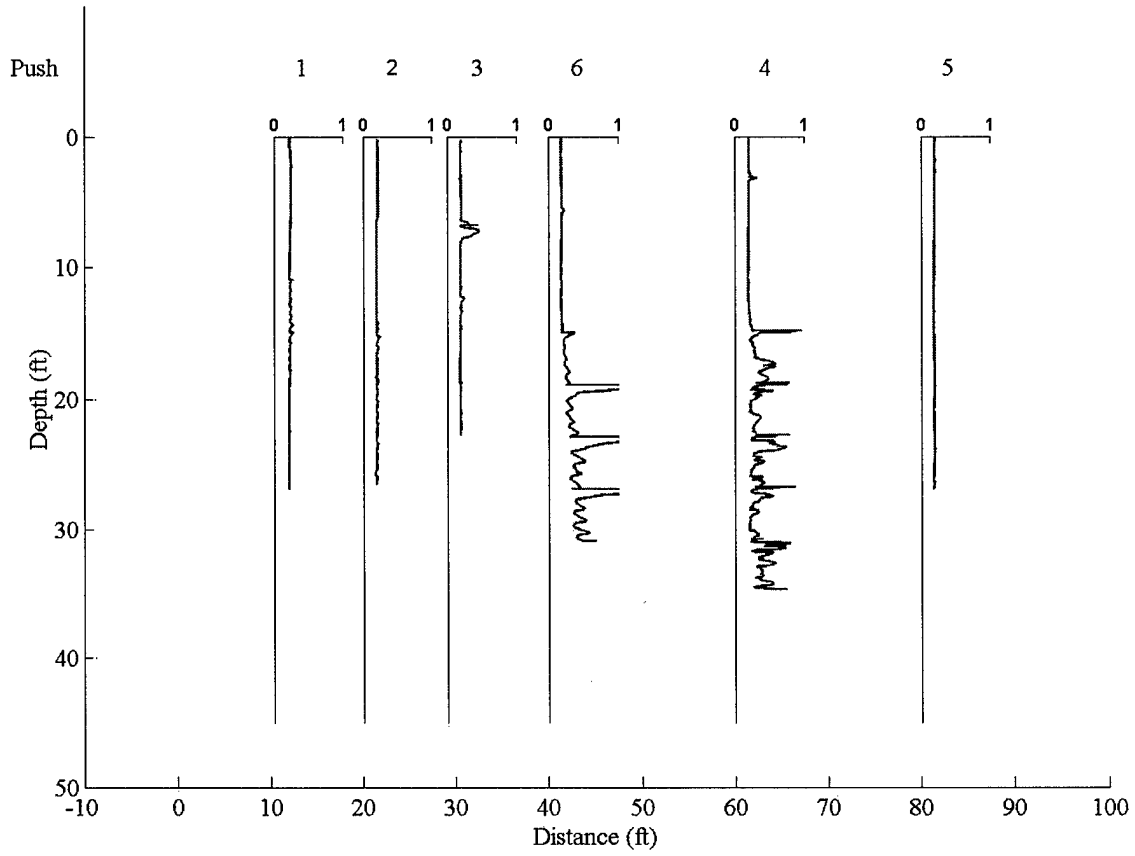

Figure 32. Field data from West Fargo former dry cleaning site. Collected with the downhole PID on June 28, 2001. The data are presented with a 0-1 volt scale.

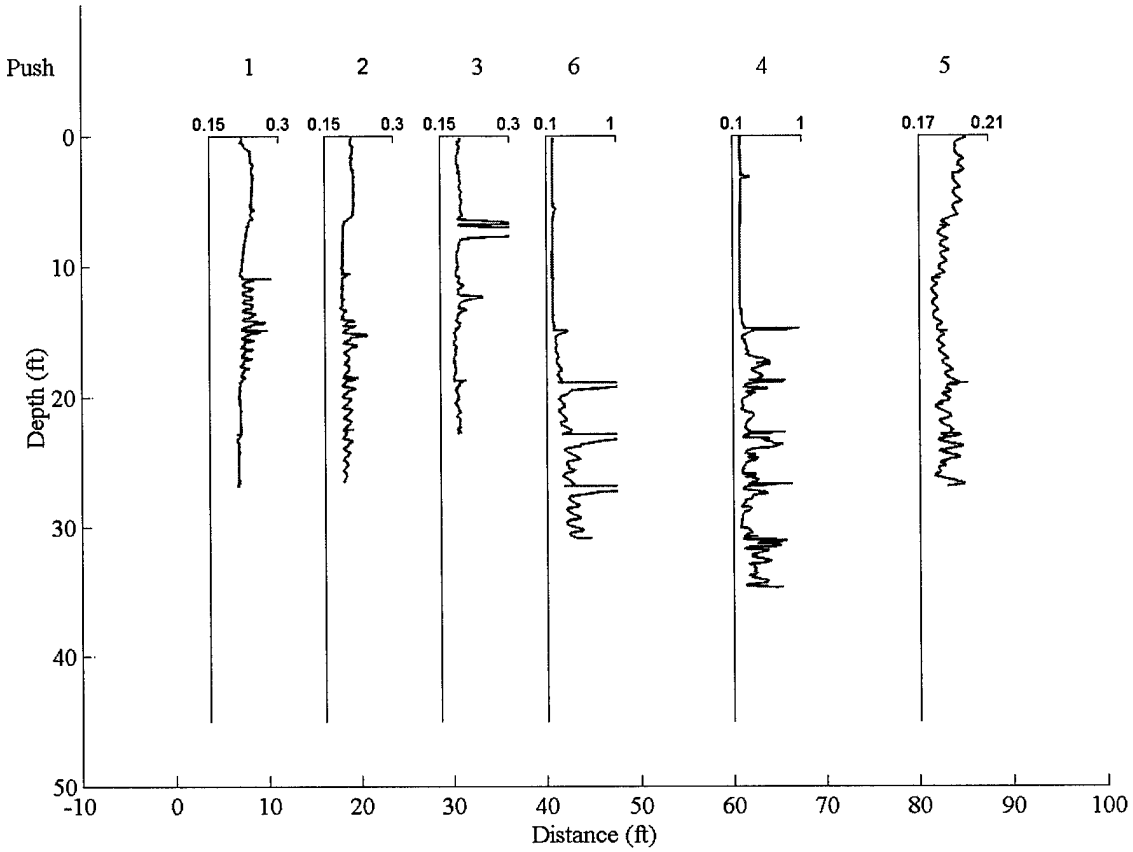

Figure 33. Field data from West Fargo former dry cleaning site. Collected with the downhole PID on June 28, 2001. The data are presented with an automatic scale.

PID - Offutt Air Force Base Site (Omaha, NE)

In September 2000, the PID and XSD were tested near Omaha NE. After the failure of the XSD, (see section XSD - Offutt Air Force Base for complete explanation of the failure), several attempts were made to waterproof the PID. While these efforts were not completely successful, several PID pushes were completed before the sensor failed entirely. A complete explanation of each PID push follows.

Five pushes were done to transect the contamination plume of the fire protection training area (FPTA). A map of our pushes across the FPTA is shown in Figure 34. The main area of contamination is in the center of the burn pit of the FPTA (Figures 35 and 36). In all five pushes, it was necessary to anchor the Geoprobe to successfully push the probe to a meaningful depth. Each push was terminated once the Geoprobe anchors started pulling out of the ground.

The first push, performed near monitoring well 2, was in an area that air base personnel thought would have little or no contamination. Rod changes were made at 2.96, 6.97, 10.93, 14.91, and 18.97 feet. The rod changes can be seen in as vertical deviations, since both the MIP temperature and signal are changing and being recorded while the rods are being screwed into place. The push rate was 1 cm/sec until the rod change at 10.93 feet, where the velocity was reduced to 0.5 cm/sec. In the vadose zone, there is very little

change in the signal, indicating little or no contamination. In the saturated zone there are several small signal variations. Based on laboratory experience, changes of this magnitude would be attributed to ppm contamination levels.

The second push ended prematurely when the anchoring system (a single earth anchor) gave way when the probe reached 15 feet. There is apparently some vadose zone contamination but the push ended shortly after reaching the saturated zone.

The third push was done just a few feet from the second push using a three-screw anchor to provide more pushing power. The data correlates nicely with push 2 from the previous day. Apparent oscillation in the signal that corresponds to changes in the MIP temperature is likely an electrical pick-up of the MIP heater cycling. The vadose zone push rate was 1 cm/sec; in the saturated zone, the rate was reduced to 0.8 cm/sec. This rate did not lead to the high cycling rate that was apparent in the first push when the velocity was reduced to 0.5 cm/sec. At 0.8 cm/sec, the heater was on all of the time (except at rod changes) thereby eliminating the cycling seen in the vadose zone. The data from the saturated zone are expanded in Figure 36. Rod changes at 18.9, 22.9, 26.9, and 30.9 feet give rise to apparent vertical transitions, since the data handling system was still recording while the rod were being changed. Several other features throughout this range can be attributed to small levels of contamination.

The fourth push was performed in the center of the FPTA. It is very similar to the other pushes with the exception of a strong feature at 7.8 feet. Data gathered by the XSD operated in uphole mode at this same spot did not reveal this same contamination. This feature is likely caused by fuel since the rods smelled of fuel when they were pulled from the ground.

The fifth push was made near a cluster of monitoring wells on the edge of the FPTA. The very large signals observed in this push are most likely due to high humidity in the PID cell. At this site, a great deal of water was encountered. Large amounts of water vapor are not completely trapped by the desiccant, resulting in a high humidity condition in the cell.

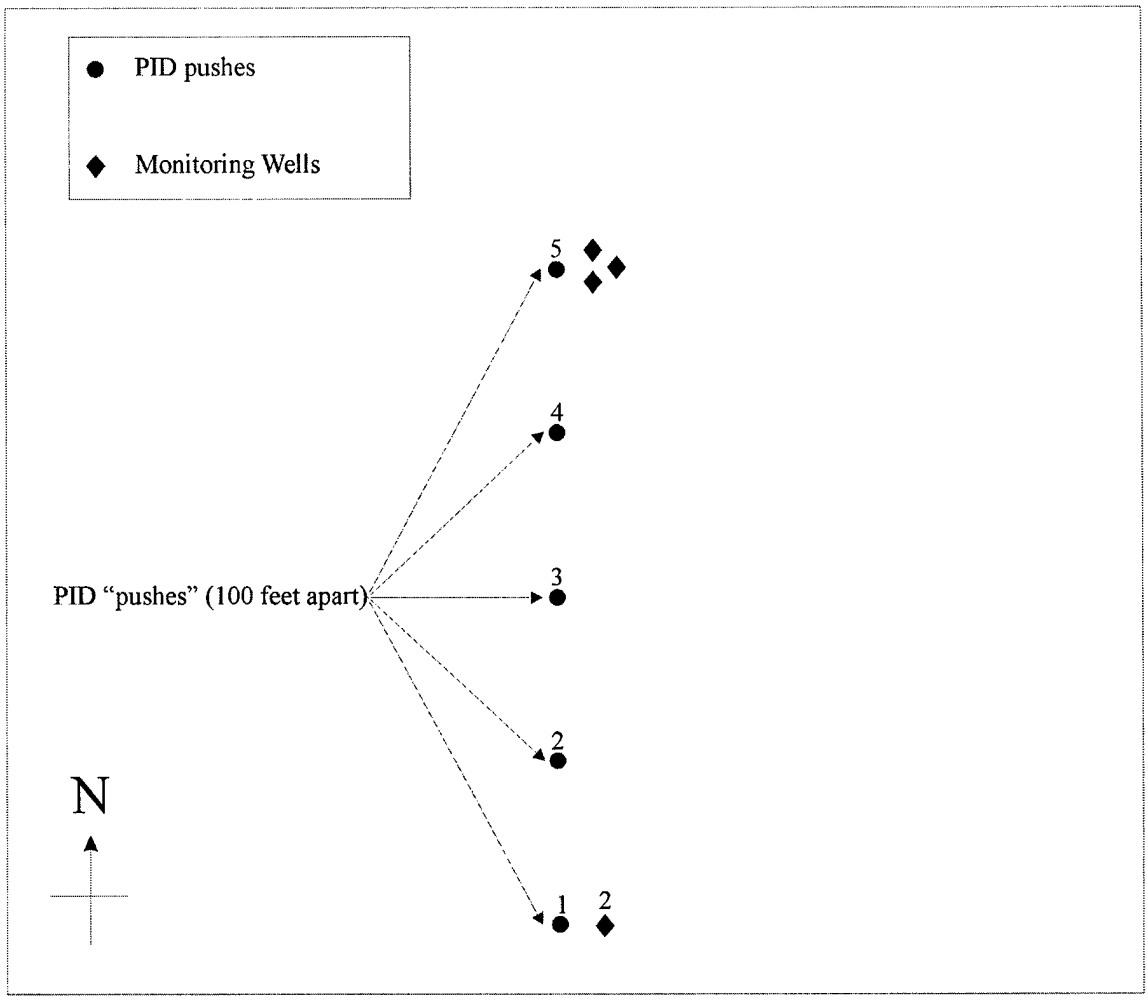

Figure 34. Map of FPTA site, Offutt AFB, showing locations of PID pushes

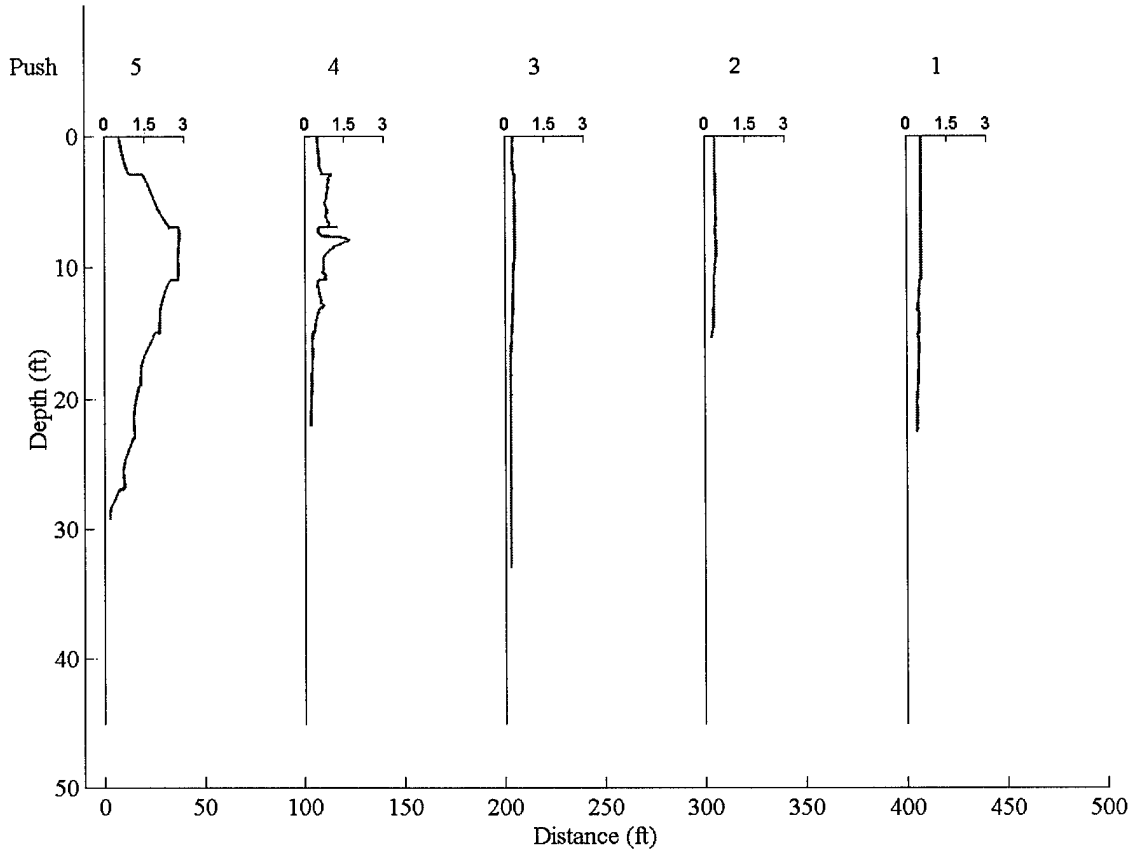

Figure 35. Field data from FPTA site, Offutt AFB. Collected with the downhole PID September 2000. The data are presented with a 0-3 volt scale.

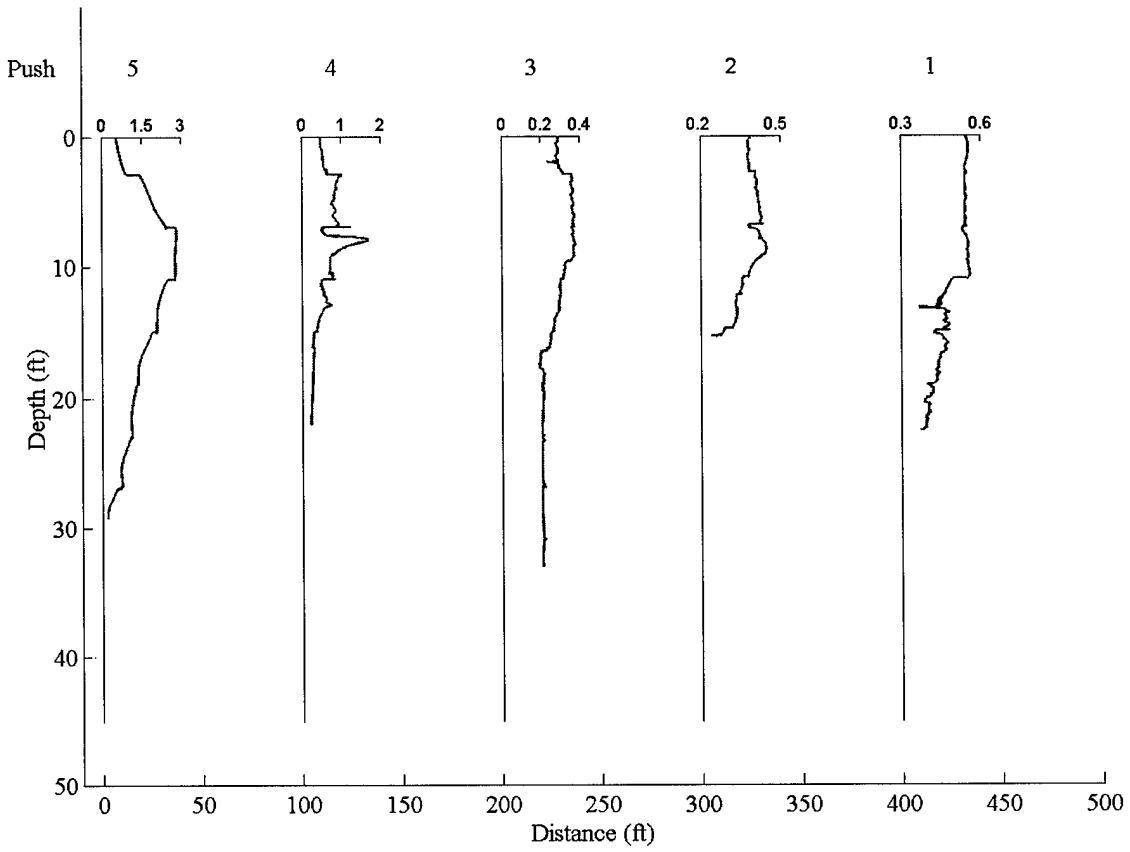

Figure 36. Field data from FPTA site, Offutt AFB. Collected with the downhole PID September 2000. The data are presented with an automatic scale.

PID - Conclusions

The development of a downhole photoionization detector (PID) was not anticipated when the contract work began. The PID responds to a wide range of hydrocarbons and therefore does not meet the requirement for specific response to chlorinated organic compounds. However, the development of a downhole PID allowed us to test several of the important aspects of placing a detector downhole.

The PID is not as complex as the XSD nor does it require efficient thermal management to achieve a stable baseline. The PID is simply a vacuum-ultraviolet lamp and a pair of electrodes. Taking advantage of this simplicity allowed us to quickly get a version into a large-bore pipe and demonstrate the feasibility of placing a detector "downhole". The initial tests revealed the cabling required for operating the detector and MIP downhole; the requisite gas connections needed; and, introduced us to the operation of the MIP.

In addition, we used the PID to develop the downhole and uphole electronics packages that are used by both the PID and XSD. These electronics provide for analog to digital conversion of the currents produced by the detectors. Since the current generated in the PID is less than that generated in the XSD, the development of the current to voltage amplification circuitry for the PID was more stringent than required for the XSD. By

developing the PID circuitry first, we were able to simply substitute the PID electronics package (at lower amplifications) into the XSD.

The PID, since it is more sensitive to water vapor than the XSD, was also used to develop the carrier gas drying strategies for the vapors coming out of the MIP. One of these approaches — a Nafion tube embedded in Drierite desiccant — was adopted for the XSD.

The development of the PID played an important role in the overall success of this project. Several of the discoveries made during the course of the PID development have been subsequently implemented in the XSD. Furthermore, knowledge gained from the PID has been used in several other projects currently underway at DTI.

PHOTOEMISSIVE ELECTRON CAPTURE DETECTOR (PE-ECD)

The NDSU subcontractors conducted laboratory studies to test the feasibility of a downhole PE-ECD. Dr. Al Meidinger designed the PE-ECD prototype and coated the first photoemissive gold thin films. Chris Walls performed most of the work reported herein and made all the measurements. Additional results are contained in Walls' M.S. thesis (North Dakota State University) and reported under Air Force Research Laboratory Contract No. F08637-98-C6003.

Although the two prototype PE-ECDs utilized off-the-shelf vacuum components that would not fit into a soil probe, the flashlamp was chosen and the cell designed so that a downhole version could be built without major reengineering. The second PE-ECD gave considerably better sensitivity than the first. However, there was not enough time to repeat all characterization studies with the second cell so some results obtained with the first cell are described herein. By the end of the contract, a PE-ECD with detection limit below 30 ppbv for PCE in nitrogen was demonstrated. A more intense flashlamp and improvements in the efficiency of the photoemissive surface could lead to further sensitivity improvements.

The PE-ECD represents a class-specific detector for chlorinated species because all of the common species of interest undergo dissociation upon electron capture to generate Cl^-. The abundant oxygen anions generated by electron attachment in air interfere with detecting the Cl^- anions. A working device would therefore require that oxygen be removed from the sample prior to electron capture detection. The oxygen separation could be accomplished via a membrane or short GC column. It was also demonstrated that the oxygen attachment efficiency varies with the mean free-electron energy in the gas. Controlling the electron energy by the applied bias provides a limited means to discriminate against oxygen anion formation.

The flash lamp PE-ECD was also demonstrated as a GC detector. The detectability was demonstrated to be below 2 pg/s PCE or 2 ppbv PCE in P-5 carrier gas, making its performance competitive with the commercial ECDs for GC purposes.

Detection of Chlorinateds

Initial downhole PE-ECD design

A pin-in-cup design with a small volume was developed and tested for potential downhole application. The PE-ECD consisted of a stack of four 2.75-inch o.d. off-the-shelf stainless steel vacuum flange blanks that were drilled and tapped. However, a less than 1-inch o.d. cell could be readily machined for a downhole probe. The front flange was 0.50 inches thick and had an axial 0.25-inch diameter aperture. The photoemissive window rested on a thin fluorocarbon o-ring within a 0.50-inch diameter depression in the back (internal side) of the flange. The photoemitter was a 0.125-inch thick, 0.50-inch diameter fused silica disc sputter coated with an approximately 10-Å thick layer of chromium before overcoating with a 300-Å thick layer of gold. The function of the chromium layer is to promote adhesion of the film to the fused silica substrate. The second flange was 0.75 inches thick and had an axial 0.25-inch diameter hole. An indium foil washer pressed between the flange and the photoemitter provided electrical contact with the metal thin film. The third flange was 1 inch thick and had an axial 1.25-inch diameter hole and two 1/4-27 NPT (National Pipe Thread) tapped holes in its outside edge fitted with Swagelok fittings to serve as gas delivery and exhaust ports. The final flange was a 0.50-inch thick high-voltage BNC (Bayonet Nut Connector) feedthrough flange. Mounted on the feed-through pin on the internal side of the flange, the copper anode (collector) extended axially through the PE-ECD to within 4 mm of the photoemissive surface. The flat head of the anode was 3.35 mm in diameter. The internal volume of the cell, excluding the gas inlet and outlet, was less than 13.5 cm^3. The bored flange and photoemissive surface that are in electrical contact form a cup about the ion collector pin. A consequence of the design was that the electric field between the photoemitter and the collecting pin was axially inhomogeneous. Later in this report,

we will describe a parallel-electrode geometry, where ion packets induce a steady current while moving toward the collector; and the pin-in-cup configuration, for where the electric field increases in strength near the collector, causing the ion current to be registered as a peak.

The Hamamatsu L4646 xenon flashlamp was usually operated at 10 Hz repetition rate and the lowest output intensity setting. Under these conditions, the pulse duration is approximately 1 μs. The output from the flashlamp was focused on the gold-coated photoemissive surface with two plano-convex fused silica lenses. The 2.5-cm focal length lens collimates the light from the flashlamp and the 7.5-cm lens produces a focused image at a distance approximately 9.5 cm from the lamp. The pulse energy incident on the photoemissive surface is about 25 μJ. The flashlamp and its power supply were housed in an aluminum-shielding box to reduce electrical noise,

A 10^8 V/A transimpedance amplifier monitored the current in the external circuit between the collector and the photoemitter. The output of the amplifier was directed to a Tektronix TDS 620A digital storage oscilloscope (DSO). The DSO was triggered by a photodiode that viewed scattered light between the shielding box and the first lens. Flashlamp pulse energy fluctuations were monitored with a second photodiode. Corrections of the electron capture signal for pulse energy were usually not performed because the variability of the flashlamp output was within a few percent of the mean pulse energy. The standard operating procedure was to operate the flashlamp for about 30 minutes while the PE-ECD was conditioned at 103.2 V bias under 0.01 L/min nitrogen flow rate prior to data acquisition.

PE-ECD characterization

Adjustments of the cell position relative to the focal point of light from the flashlamp showed that maximum free-electron production occurs when the discharge image is focussed on the photoemissive coating. The free-electron generation in nitrogen was characterized as a function of nitrogen flow rate in the range 0.01 to 2.00 L/min. The data show that total charge collected is nearly independent of flow rate for values greater than 0.20 L/min, but about 20% higher when the flow rate is nearly zero. These data show that the PE-ECD signal depends on gas flow rate through the detector. The influence of bias voltage on electron charge collected at constant nitrogen flow rate was also determined. The bias voltage was reduced incrementally starting at 103.2 V. The bias voltages were measured at the connectors on the high voltage supply using a digital multimeter. The data (Figure 37) are similar to those obtained from previous detectors using photoemissive electron sources. Although the light intensity and the number of photons reaching the photoemitter are essentially constant, electron yield increases non-linearly with bias voltage. Clearly, the strength of the electric field plays a role in the release of electrons from the metal film bathed in atmospheric pressure nitrogen. A curve nearly identical in shape to that of Figure 37 is obtained when the peak of the electron current waveform is plotted as a function of bias voltage.

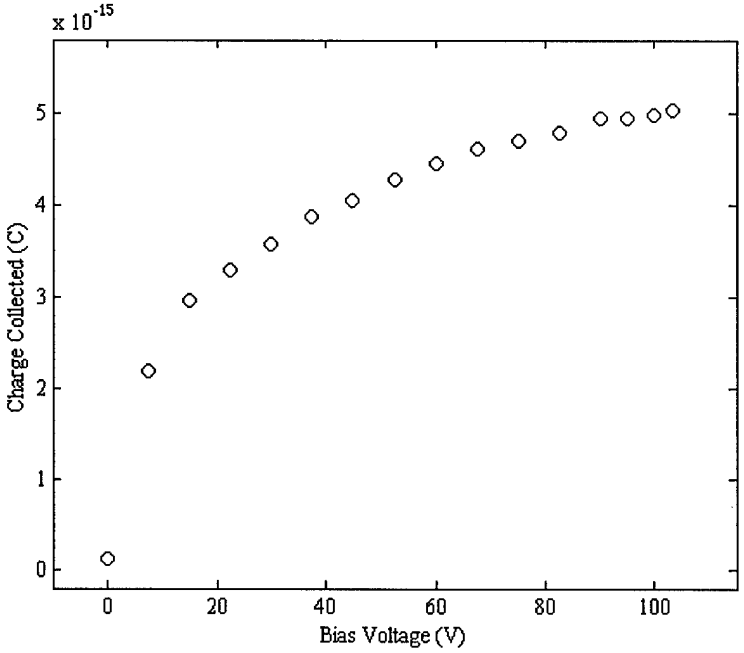

Figure 37. Total charge collected in nitrogen as a function of bias voltage

Limit of detection - PCE in nitrogen

Exponential dilution is a convenient, straightforward method for producing a range of analyte concentrations necessary to calibrate a vapor sensor. A gas mixture of known analyte concentration is prepared by injecting a known volume of analyte liquid or vapor into a rigid chamber containing an inert carrier, or diluent gas. After sufficient time to ensure complete gas mixing, additional diluent gas is flowed steadily through the chamber, causing the analyte concentration in the gas exiting the chamber to decrease exponentially with time.

The concentration of analyte in the exiting gas is calculated from the equation

$$\log c = \log c_o - \tau Q/2.303V$$

where c is the analyte concentration in the exiting gas, c_0 is the initial analyte concentration, τ is the duration of the gas flow, Q is the constant flow rate of gas through the chamber, and V is the volume of the rigid chamber.

A 5-L round-bottomed glass flask fitted with an o-ring sealed metal stopper was inserted into the gas line between the flow meter and the PE-ECD. Three stainless steel tubes pass through the aluminum stopper. A relatively long tube delivers diluent gas to the bottom of the flask while a shorter tube extracts mixed gas from the center of the flask. Each tube is fitted externally with a valve so that the chamber can be isolated during preparation of the gas mixture. The shortest tube, which is capped externally with a 5 mm NMR septum, is the analyte injection port. The action of a magnetic stir bar sealed within the flask enhances gas mixing during preparation of the standard and during the exponential dilution. After the flask and PE-ECD were flushed extensively with nitrogen, the inlet and outlet valves on the flask were closed and the bypass flow opened to continue flushing of the PE-ECD during preparation of the gas mixture. After initial measurements using the minimal flashlamp discharge, the maximum discharge voltage

was used to obtain the following results. The maximum discharge voltage generates about 2.5 times greater number of free-electrons compared to what is obtained at minimum flashlamp voltage. This factor is approximately equal to the manufacturer's specified ratio of flashlamp output at the maximum and minimum intensity settings.

A mixture of 40.7 ppmv PCE in nitrogen was prepared by introducing 0.85 μL PCE liquid into the 5-L flask. After a 50-minute equilibration period, a dilution flow of 0.40 L/min nitrogen was initiated. Waveforms were acquired as 256-acquisition averages at 90-s intervals over a two-hour period. The exemplary waveforms shown in Figure 38 were obtained during a dilution experiment. The waveforms consist of a predominately free-electron signature from 0 to about 50 μs and an anion signature visible beyond 50 μs. The anion signal is due to chloride ions formed by the dissociative attachment of electrons to PCE. Because analyte is dispersed uniformly throughout the cell, electron capture events occur throughout the active volume between the electrodes as the free-electron swarm passes from the photoemitter to the collector. Thus, anions reach the collector over a range of drift times, extending from near 0 (i.e., when the photons are incident on the photoemissive surface) to as long as 300 μs, depending on the distance from the collector at which they were formed. As a result, the fast portion of the chloride signal, associated with chloride ions formed relatively close to the collector, is superimposed upon the free-electron signal. The negative overshoot seen around 90 μs drift time in waveform *e* is due to electronic ringing in the circuit.

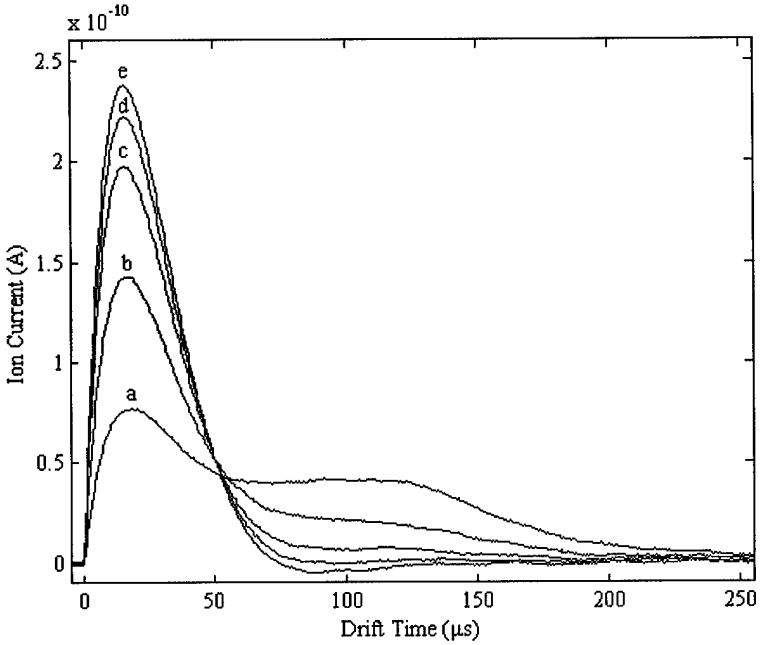

Figure 38. Ion current as a function of drift time at acquisition times a) 6 min, b) 18 min, c) 30 min, d) 42 min, and e) 128 min corresponding to estimated concentrations 29.5, 11.3, 4.3, 1.7, and 0.002 ppmv PCE, respectively.

The fact that the free electron and chloride ion currents overlap in time makes partitioning the waveform into electron and chloride anion portions problematic. For simplicity, we selected a fixed drift time point (52 μs) between the electron and anion signatures and assumed all ion current before this time was due to free electrons and all after was due to anions. This simplification overestimates electron charge and underestimates chloride charge. Free-electron charge collected between 0 and about 52 μs drift time and chloride charge collected between 52 and 400 μs drift time are plotted as functions of dilution time in Figure 39. Also plotted in

Figure 39 is one-half the total charge (one-half the sum of integrated free-electron current and integrated anion current) as a function of dilution time, which is included as a consistency gauge. Both the decrease in chloride ion charge and the increase in free-electron charge match the predicted exponential decay in PCE concentration except during the initial few minutes when the concentration was very high.

The detection limits for PCE can be calculated two different ways from the data shown in Figure 39, one based on the disappearance of free-electron charge (electron charge "absorption" by PCE) and the other based on the production of chloride ion charge from electron capture by PCE. The mean and standard deviation of charge collected between 100 and 133 minutes was computed for each charge curve and applied to calculations of detection limits for PCE. The detection limit for PCE based on electron charge "absorption" was calculated as the mean minus three standard deviations, while that for PCE based on chloride charge generation was calculated as the mean plus three standard deviations. The results of these calculations, 7.73E-15 C and 3.61E-16 C, respectively, are indicated by lines *a* and *b* in Figure 39. The dilution times corresponding to these charge values yield estimated concentrations of 0.34 and 0.64 ppmv PCE, respectively, for the first PE-ECD cell design.

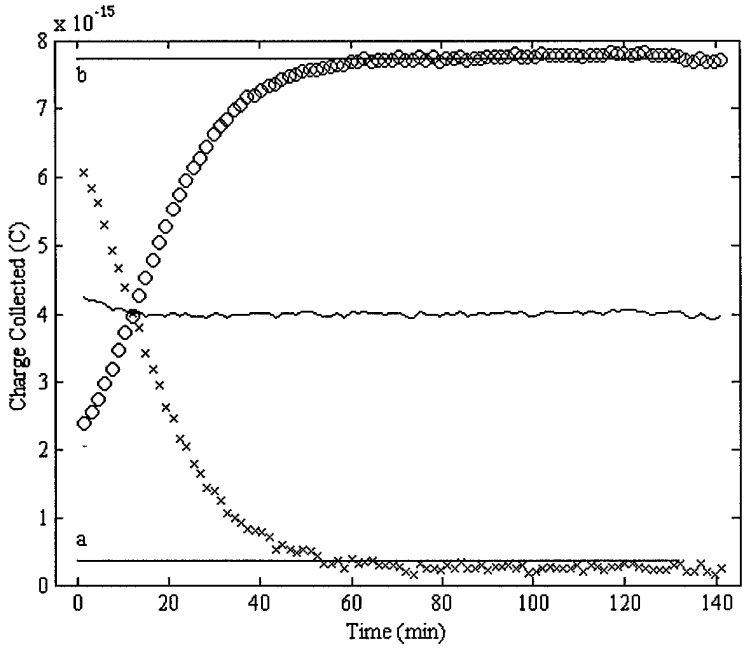

Figure 39. o) Electron charge, x) chloride ion charge, -) and one-half the total charge collected as a function of time during the exponential dilution of a 5-L mixture of 40.7 ppmv PCE in nitrogen at a dilution flow rate of 0.40 L/min nitrogen. Lines *a* and *b* represent the means plus and minus three standard deviations of the chloride charge and electron charge collected between dilution times 100.5 and 133 min, respectively.

The preceding experiment was repeated with a mixture of 46.4 ppmv TCE in nitrogen. The mean and standard deviation of charge collected between 60 and 90 minutes were computed for each charge curve and applied to calculations of detection limits for TCE based on electron and on chloride ion data. The results are 7.36E-15 C and 4.04E-16 C corresponding to the estimated concentrations 1.00 and 2.05 ppmv TCE, respectively. The values are about three times higher for TCE than PCE, which is consistent with their known electron capture cross-sections. Due to the extra chlorine atom, PCE captures electrons more efficiently than TCE.

Detection of PCE from permeation tube

A PCE permeation tube was purchased from Kin-Tek, Inc. (LaMarque, TX). The tube was certified prior to shipment to provide 237 ng PCE vapor per minute at 30°C. When bathed in a gas flowing at 1 L/min (1000 cm^3/min), the permeant concentration in the resulting gas mixture is 31.5 ppbv PCE. Since the temperature of the device must be held constant to maintain permeant concentration at a given gas flow rate, a simple constant-temperature gas mixer was constructed from available equipment and inserted into the gas delivery line. Three or four waveforms were collected at each of several selected flow rates of PCE-doped and pure nitrogen in alternating fashion by switching the flow between the permeation chamber and the bypass. This generated corresponding PCE and pure nitrogen response curves for direct comparison. With each increase in flow rate and change of gas, the system was allowed to equilibrate for at least 15 minutes prior to data acquisition. Comparison of responses to PCE-doped and pure nitrogen reveals clear detection of PCE at concentrations between 530 and 315 ppbv. The significant amount of chloride charge detected at 315 ppbv PCE relative to the reference value obtained in pure nitrogen supports a lower detection limit.

Photoemissive Variation Due to Molecular Gas Exposure

Response of the PE-ECD to cyclohexane vapor

Injections of pure PCE or TCE into the 5-L flask create standard gas mixtures of relatively high initial concentration, on the order of tens of ppmv. The high initial concentration versus the detection limits of these species necessitates long dilution times, during which analyte may leak from the system or adsorb to, or be absorbed by, internal components of the system. Lower initial concentrations can be produced by diluting the chlorinated species in a non-attaching solvent. A known volume of the solution can then be introduced into the 5-L flask. Cyclohexane, which is transparent to low-energy electrons and readily available, was evaluated as a candidate solvent for this application. To evaluate the approach, a gas mixture was prepared by adding 2 μL of cyclohexane to the 5-L flask containing high purity nitrogen. After 1 hour equilibration, a 0.40 L/min dilution flow was initiated through the flask and cell. Data were collected at 256-acquisition averages every 90 s for nearly two hours. It was determined that cyclohexane is a suitable diluent if the cell is preconditioned for about an hour with cyclohexane vapor.

Improved PE-ECD Cell Design

The pin-in-cup design was used for a significant portion of the subcontract effort, but a modified version developed relatively late in the contract performed substantially better. As many characterization experiments as possible were repeated in the time remaining. The improved cell has lower dead volume and was altered so that the gas flow was directed through the space between the electrodes; the earlier design had the gas inlet and outlet well behind the head of the collecting pin near the back of the detector. The second flange was replaced with one of dimensions identical to its predecessor, but with gas delivery and exhaust ports bored as near its front edge as possible, through opposite sides of the flange to the axial hole. Short lengths of stainless steel tubing were inserted and soldered in place. The delivery port used 1/16-inch tubing terminated in a zero-dead-volume connector and ferrule and the exhaust port used 1/8-inch tubing terminated in a 1/8-inch nut and a 1/8-inch to ¼-inch Swagelok adapter attached to the room exhaust system. The third flange was omitted and the high-voltage BNC feedthrough flange was changed. Because the ground connector on the replacement feedthrough was not electrically isolated from the flange, a Teflon disc that fit tightly about the feedthrough pin was inserted between the second and feedthrough flanges. A new collecting pin that fit snugly over the feedthrough pin was fabricated from a short length of brass tubing capped with a droplet of solder ground flush. To decrease dead volume and to ensure insulation from the surrounding flange, the collecting pin was sheathed within a ceramic sleeve that extended from the head of the pin to the Teflon disc. The photoemitter-to-pin distance was about 3.3 mm. The new cell

has a mini-parallel plate configuration compared to the previous pin-in-cup. Other aspects of the detector and associated electronics were left unchanged.

The design changes affected the ion current waveforms. Using the permeation system, five 256-acquisition average waveforms were collected at each of several diluent flow rates between 0.01 and 0.64 L/min, representing PCE concentrations from 3.15 to 0.05 ppmv. At the end of the experiment, five 256-acquisition background waveforms were collected in 0.64 L/min pure nitrogen by switching the flow through the bypass. The mean background waveform was subtracted from the mean PCE waveform in order to remove electronic noise. Corrected mean waveforms at selected diluent flow rates are presented in Figure 40.

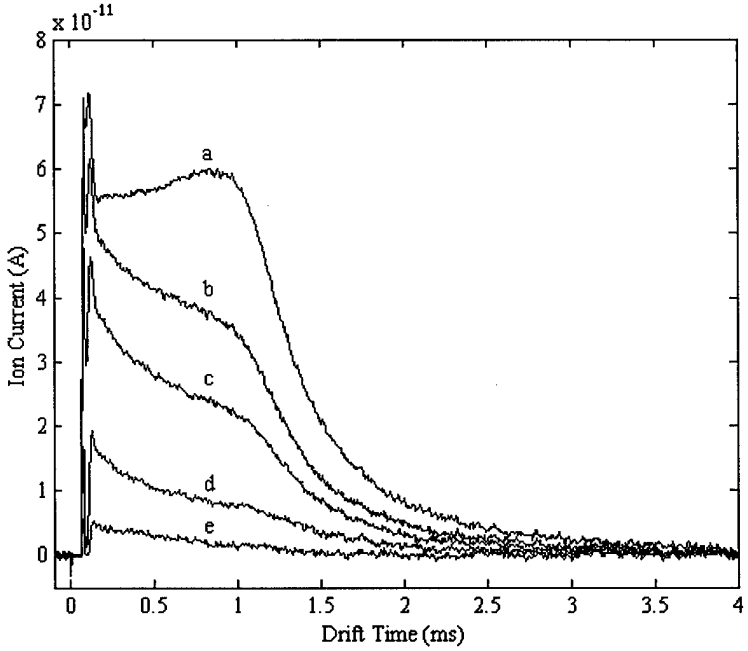

Figure 40. Ion current waveforms of PCE doped in nitrogen at concentrations a) 3.15, b) 1.58, c) 0.63, d) 0.19, and e) 0.05 ppmv

The waveforms differ markedly from those of the pin-in-cup detector, but are qualitatively similar to waveforms collected in similar studies for larger parallel plate configurations. The ion current persists about 10 times longer compared to that of the first cell. In addition to prolonging the ion current, design changes appear to have increased ionization and detection of chloride ions from PCE at a given concentration by about one order of magnitude. The improved response is attributed to decreasing the dead volume of the cell by directing gas flow between the electrodes instead of behind the head of the collecting pin.

Chloride ion charge, calculated by integrating the mean waveforms between 150 μs and 4 ms drift time, indicates that the chloride charge collected is not linear with PCE concentration. It is thought that the detector response saturates at high concentration. However, these results may also reflect the influences of flow rate, temperature, or pressure on permeation rate. The hump of curve *a* in Figure 40 clearly indicates space charge effects due to the very high ion concentration, which may also account for the nonlinearity. In any case, the relationship is monotonic and consequently the detector can be calibrated for concentration.

The temperature bath is designed to heat the diluent gas from room temperature to 30°C before it reaches the permeation tube, but its performance as a function of diluent flow rate is unknown.

Thus, as flow rate increases, heating efficiency and gas temperature at the permeation tube might decrease, inhibiting permeation and artificially decreasing PCE concentration. This would cause a decrease of chloride charge detected with flow rate. To alleviate any overpressure, Swagelok tees were inserted into the gas line immediately after the constant temperature system and immediately after the PE-ECD and connected by a length of 1/8-inch Teflon tubing. The section of tubing before the permeation chamber containing the glass beads was left in place. The previous experiment was repeated after several days of flushing with high-purity nitrogen and realignment of the flashlamp, optics, and PE-ECD, which improved photoyield considerably. Figure 41 is a plot of chloride ion charge as a function of PCE concentration.

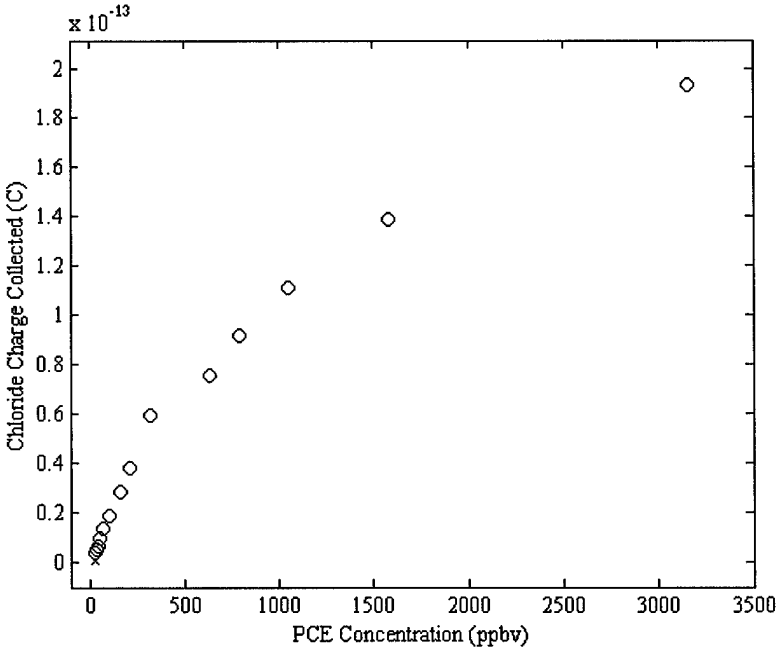

Figure 41. Chloride charge as a function of calculated PCE concentration. The *x* plotted near the origin represents nitrogen background at 1.00 L/min flow rate.

Although the entire response curve is not linear, the portion for PCE concentration less than 350 ppbv appears linear. This portion, reproduced in detail in Figure 42, shows detection of PCE at concentrations as low as 30 ppbv in nitrogen. The linear response and the amount of chloride charge collected in the presence of 30 ppbv PCE, versus the pure nitrogen reference, indicate a lower detection limit for PCE. Whether pressure relief, enhanced photoelectron yield, or both are responsible for the improved detector linearity is uncertain. Pressurization of the permeation chamber with flow rate is purely speculative, but the 2.5-fold increase in photoemission yield, as judged by the number of chloride ions generated at 0.01 L/min flow rate in this run versus the previous two, is real. The substantial increase might have delayed the onset of saturation and increased the linear dynamic range of the detector.

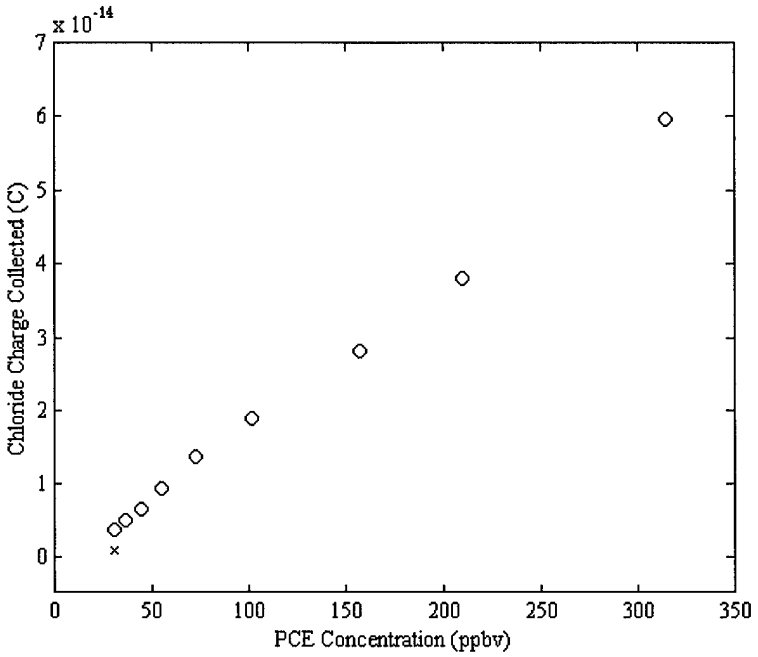

Figure 42. Linear portion of chloride charge as a function of calculated PCE concentration. The *x* plotted near the origin represents nitrogen background at 1.00 L/min flow rate.

Carrier Gas and Oxygen Electron Attachment

Free-electron signature in non-attaching gases

Free-electron signatures were measured in the three non-attaching gases, namely, high-purity nitrogen, argon, and P-5 (5% methane in argon). Prior to waveform acquisition, the delivery line and PE-ECD were purged with selected gas for several minutes at low flow rate. After the free-electron current stabilized, multiple waveforms were collected as 500-acquisition averages of record length 1000 points on 25 or 50 μs/div horizontal scales. Flow rates, measured with the mass flow meter, were 0.03 L/min for nitrogen and 0.02 L/min (uncorrected) for both argon and P-5. During all measurements, the flashlamp was operated at maximal output intensity and 25 Hz repetition rate and the PE-ECD bias voltage was 103.2 V. Mean ion current signatures obtained in each gas appear in Figure 43. The size of the free-electron signature is largest in argon, moderate in P-5, and smallest in nitrogen, for which the peak ion currents are 0.22 nA, 0.16 nA, and 3.6 nA, respectively. In both argon and P-5, the free-electron signal reaches maximum current at 0.0160 ms drift time; while in nitrogen this occurs at 0.0170 ms. The signatures, normalized to maximum ion current, appear in Figure 44.

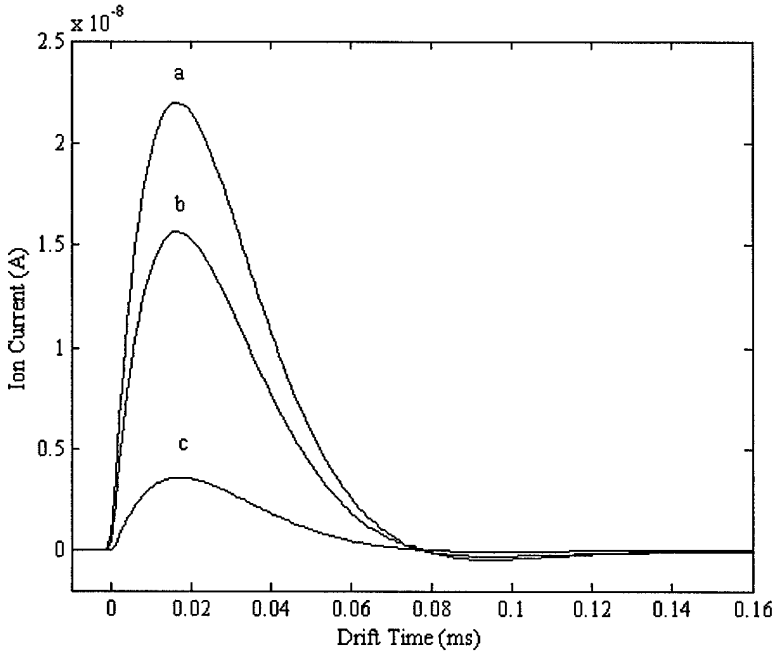

Figure 43. Mean free-electron signatures obtained in a) argon, b) P-5, and c) nitrogen

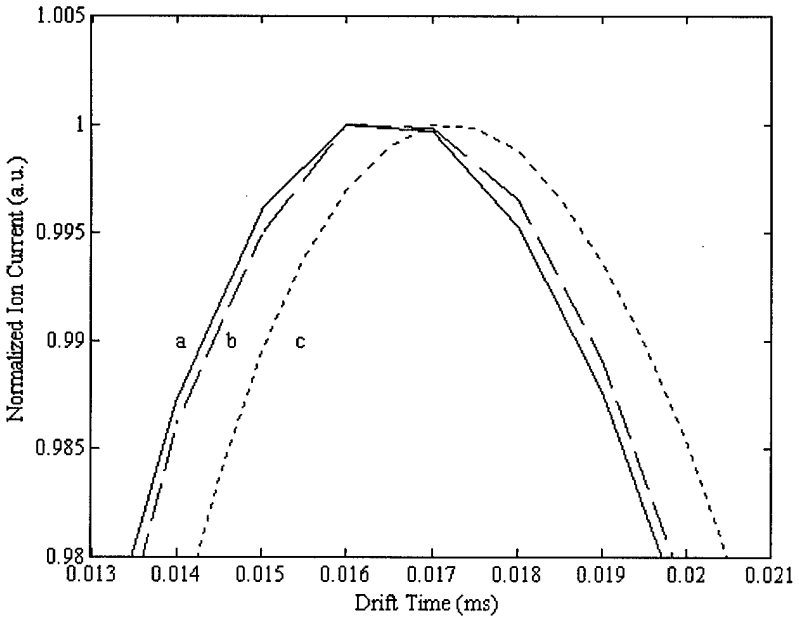

Figure 44. Free-electron signatures obtained in a) argon, b) P-5, and c) nitrogen normalized to maximum ion current

Figure 44 indicates that the free-electron current peak occurs at longer drift time in nitrogen than in either argon or P-5. The P-5 electron peak possibly occurs at slightly longer drift time than that in argon. The order of drift velocities Ar>P-5>N_2 suggested by Figure 44 does not agree with literature values that give the order of electron drift velocities P-5>N_2>Ar. Despite the drift time differences, Figure 44 shows that all three-electron signatures are of similar half-height

width (FWHM) (approximately 36 μs), which is considerably wider than the 1 to 2 μs duration of the flashlamp discharge. Similar results were obtained when the measurements were repeated. Baseline overshoot occurring near the end of the free-electron signatures, particularly in those of argon and P-5 in Figure 43, was eliminated by adjusting the position of the shunt capacitor wire in the pre-amplifier.

Oxygen anions in nitrogen

Oxygen anions created by free-electron attachment interfere with the detection of chloride anions in air and, therefore, are of major interest for this study. Although the chlorinated molecules have higher electron affinities than oxygen and ultimately acquire electrons from the oxygen anions, the resultant oxygen anion peak from the much more abundant oxygen molecules overlaps the chloride anion peak. This is smeared even more, since the process occurs throughout the drift time of the anions to the electrode. Also in air, the free electrons are nearly all attached by the abundant oxygen molecules, making detection of chlorinateds by electron absorption impossible.

Oxygen anions in P-5

A similar experiment was performed in P-5 bath gas for comparison. An open tube was included in the gas delivery line to admit trace air in P-5 carrier gas to the PE-ECD. A Swagelok tee fitting, to which a short length of Teflon tubing was attached, was placed in the gas delivery line. At low flow rates of P-5, due to the partial vacuum to which the cell exhaust is attached, air was drawn into the gas line through the tube. After establishing a P-5 flow rate of 0.03 L/min (uncalibrated), the oxygen anion signature was measured frequently as the bias voltage was increased from near 0 V to 103.2 V. Anion charge is plotted in Figure 45 as a function of bias voltage. Using the free-electron data acquired in the absence of air, ratios of anion to electron charge were computed at all bias voltages. Ratios calculated at bias voltages below 2 V were discarded due to insignificant or limited electron production from the photoemitter. Ratios computed at bias voltages 2 V or greater are plotted in Figure 46 as a function of bias voltage. Figure 46 shows a well-defined peak that reaches a maximum near 9 V bias, lower than the 18-V bias shown by the peak obtained from trace air in nitrogen. As seen in nitrogen, the low-bias side of the peak is sharper than the tailing high-bias side, which assumes the shape of an exponential decay. Attachment efficiencies are higher at all bias voltages in P-5 and charge ratio at the peak is 0.18 in P-5 compared to 0.08 in nitrogen. Attachment efficiency at the maximum in P-5 appears to be at least 50% larger than ratios on either side of the peak, a result similar to that seen in nitrogen.

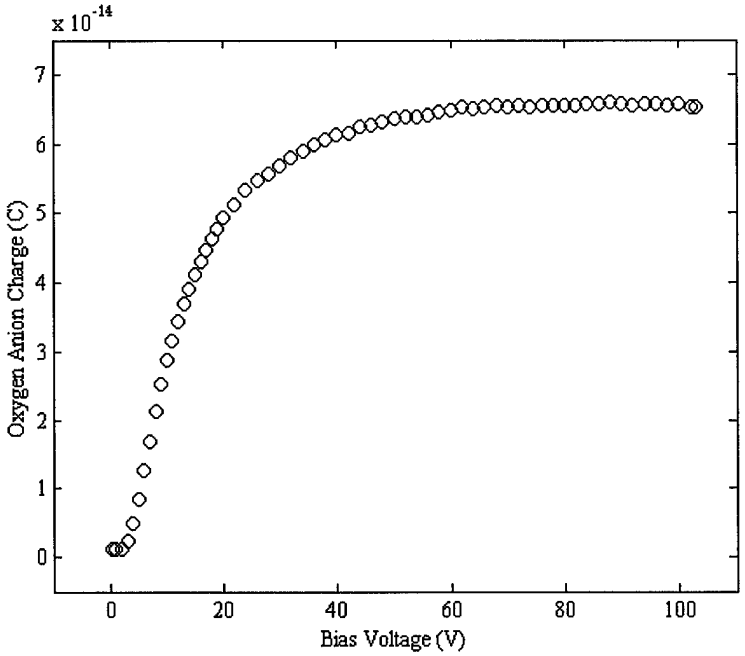

Figure 45. Anion charge as a function of bias voltage

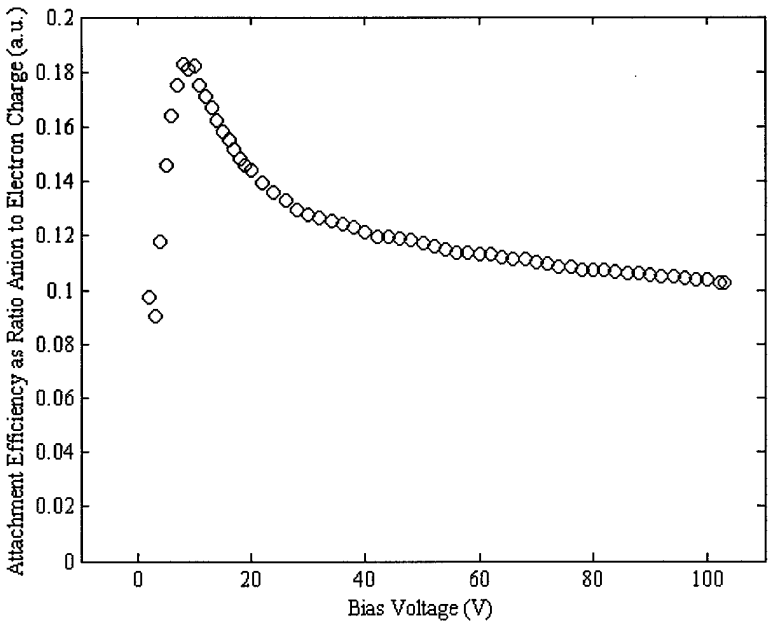

Figure 46. Electron attachment efficiency, computed as ratios of oxygen anion to free-electron charge, as a function of bias voltage

PE-ECD as a GC Detector

The PE-ECD was interfaced to a SRI 8610 gas chromatograph at DTI. As space for the experimental layout was limited, gas flow through the PE-ECD was reversed relative to previous arrangements; the 1/8-inch stainless steel tube became the gas inlet and the 1/16-inch stainless

steel tube became the outlet. The outlet of the chromatographic column was attached to the PE-ECD through a length of 1/16-inch Teflon tubing and a 1/16-inch to 1/8-inch Swagelok adapter. All other aspects of the experimental setup were left as in previous experiments. The GC was equipped with a PID whose output was acquired on the GC computer. A second computer acquired the PE-ECD output. Although data acquisition could not be started simultaneously and the detectors were at different lengths from the column inlet, for purposes of comparison, both PID and PE-ECD chromatograms were obtained for each sample admitted to the GC. The GC used P-5 carrier gas flowing at 15.6 mL/min.

Acquisition of PE-ECD waveforms and PID response was initiated immediately after each injection. The GC column temperature was 50°C and the flow rate of P-5 carrier gas through it was 15.6 mL/min. The PE-ECD was operated at bias voltage 30 V and the repetition rate of the flashlamp was about 9.5 Hz. During each run, PE-ECD waveforms were collected as 8-acquisition averages at computer-timed intervals of 4 s for total durations of 450 to 600 s. These were integrated from drift times 0 to 77.5 μs, corresponding to the baseline width of the free-electron signature. When plotted as a function of time, the integrals formed a chromatogram that represented the absence of electrophore in the eluent as high charge collected and the presence of electrophore as low charge collected. The initial studies used pesticide-grade hexanes as the solvent for preparing low concentrations of PCE. Additional features in the chromatograms were thought to possibly correspond to 20-ng/L-heptachlor epoxide present in pesticide-grade hexanes. Pentane was then selected as solvent for the solutions in the hope that this would simplify the chromatograms. A 2.59-ppm PCE stock solution was prepared by adding 2.5 μL PCE to 25 mL pentane. A 0.72-ppm PCE solution was prepared from this solution by adding 50 μL of it to 18 mL pentane. Ten sample solutions of concentrations ranging from 5.62E-3 ppm to 0.36 ppm PCE were prepared starting from the secondary solution via various two-fold and three-fold serial dilutions. In turn, 10.0 μL portions of each of the 10 sample solutions were applied directly to the GC column by microsyringe.

The raw chromatograms were corrected to baseline then normalized as follows. All chromatograms were anchored to zero by subtracting from each the average of the first 13 charge values. Then the chromatograms were normalized and inverted by dividing each by the minimum charge value attained between 0 and 87 s elution time. Corrected chromatograms represented electrophore absence as zero signal and presence as positive signal. Examples of corrected chromatograms appear in Figure 47.

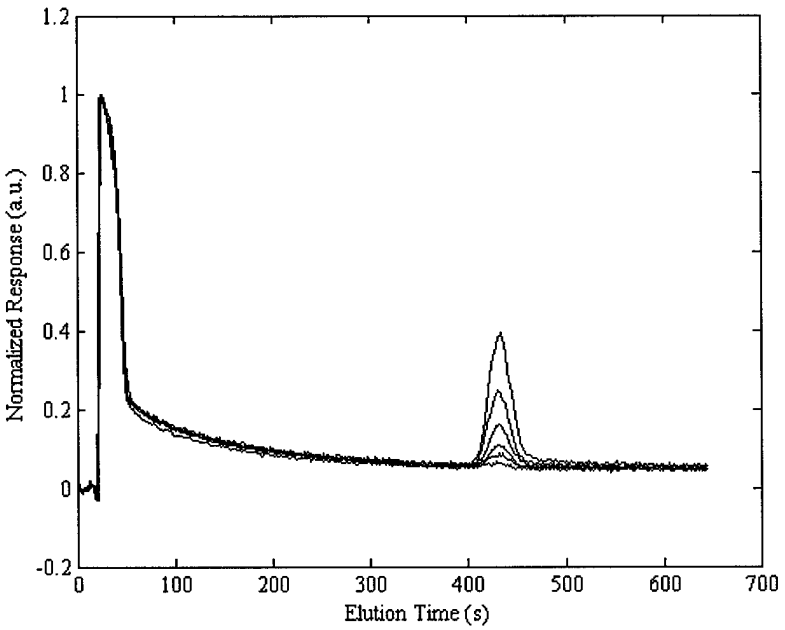

Figure 47. PE-ECD chromatograms obtained from solutions of PCE dissolved in pentane. Positive response represents loss of free electrons to electron attachment by constituents of GC eluent passing through the cell.

Figure 47 shows PE-ECD response to PCE at retention times near 430 s and, despite the change of solvent, response to the unidentified electrophore at retention times near 25 s. The retention time of the unidentified peak is considerably shorter than the 122 s retention time of the corresponding peak shown in PCE chromatograms of PCE dissolved in hexanes. The raw PE-ECD chromatograms again indicated that the size of the peak caused by the unidentified electrophore is independent of PCE concentration.

Tails of the unidentified electrophore peaks were fitted then subtracted from the PE-ECD chromatograms. Fits included points either side of the PCE peaks from approximately 87 s to 398 s and 592 s to 643 s elution times. Fit equations were evaluated from 87 s to 643 s elution time then subtracted from corresponding chromatograms, leaving the PCE peaks surrounded by linearized, zeroed baseline. Corrected PCE peaks appear in Figure 48.

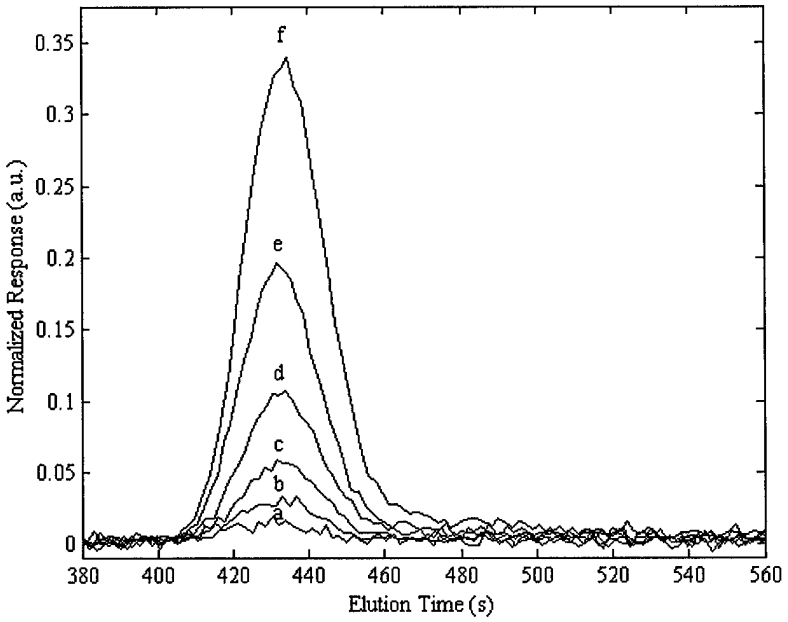

Figure 48. Responses to PCE solution concentrations a) 0.0075 ppm, b) 0.030 ppm, c) 0.045 ppm, d) 0.090 ppm, e) 0.180 ppm, and f) 0.36 ppm, representing PCE masses, 47, 187, 281, 563, 1.13E+03, and 2.25+03 pg, respectively

The PCE peaks were integrated with respect to the time increment between chromatogram data points, about 1.75 seconds. PCE signal areas, plotted as a function of the calculated mass of PCE administered to the GC, appear in Figure 49. The small PCE peaks slightly disrupt the linearity of PCE peak area with the calculated PCE mass.

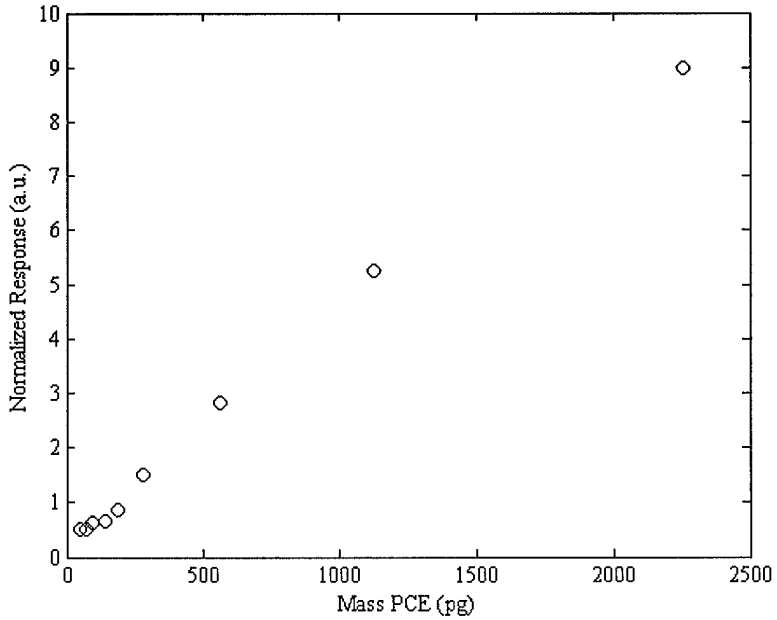

Figure 49. PCE peak area as a function of calculated PCE mass administered to the GC

The baseline width of the PCE peaks varies, but because the start and end points of each peak are often difficult to ascertain, a baseline width of 67 s was assumed for all PCE peaks. This fixed width was used to calculate mean mass flow rates of PCE and mean gas phase densities and concentrations of PCE in P-5 during the flow of PCE-containing eluent through the PE-ECD. Mean mass flow rates were calculated in units of pg/s by dividing masses of PCE applied to the GC column by the baseline width. PCE masses divided by products of the P-5 carrier flow rate and the baseline width yielded mean gas phase PCE densities in P-5 in units of pg/mL. Mean PCE vapor concentrations were calculated in units of ppbv PCE in P-5 by multiplying mean gas phase densities by the inverse of the molecular weight of PCE (6.03E-2 mol/g), the gas constant R, (8.2058 L·atm/mol·K), and the temperature (assumed to be 323 K). Characteristics of the PCE peaks and results of these calculations are summarized in Table 6.

Table 6: Characteristics of PCE peaks appearing in Figure 49

Run	Mass PCE (pg)	Width (s)	Area (a.u.)	pg PCE/s	[PCE] pg/mL	[PCE] ppbv
10	2250	67	9.0051	67.28	258.8	41.4
9	1130	67	5.2476	33.64	129.4	20.7
8	563	67	2.8276	16.82	64.7	10.3
7	282	67	1.5203	8.41	32.3	5.2
6	188	67	0.8683	4.20	16.2	2.6
5	141	67	0.6490	2.80	10.8	1.7
4	93.9	67	0.6154	2.10	8.1	1.3
3	70.4	67	0.5257	1.40	5.4	0.9
2	47.0	67	0.5185	1.05	4.0	0.7

PCE detectability appears to lie near 2 pg/s PCE or 2 ppbv mean gas phase PCE concentration in P-5 based on free-electron loss to electron capture. These results agree with those obtained from PCE in pesticide-grade hexanes.

Photoemissive Thin Films

Photoemissive windows for the parallel-electrode PE-ECD

Two 0.125-inch thick, 1.75-inch diameter fused-silica windows were masked. They were then coated, first with approximately 10 Å chromium, then with 500 Å gold using a Balzers SCD 030 sputter coater. The mask produced coatings consisting of a 1.25-inch diameter disc centered on the fused-silica window with a 0.175 x 0.175-inch tab extending from the edge of the disc toward the edge of the window. Visual inspection of the completed coatings revealed only minor defects. Baseline-corrected transmission spectra of the photoemissive windows and an uncoated fused-silica window were acquired with a Varian Cary 500 spectrophotometer from wavelengths 200 to 800 nm. All transmission spectra were acquired at approximately a 45° angle, with the beam incident on the coated side of the photoemissive windows. The transmission spectra are shown in Figure 50.

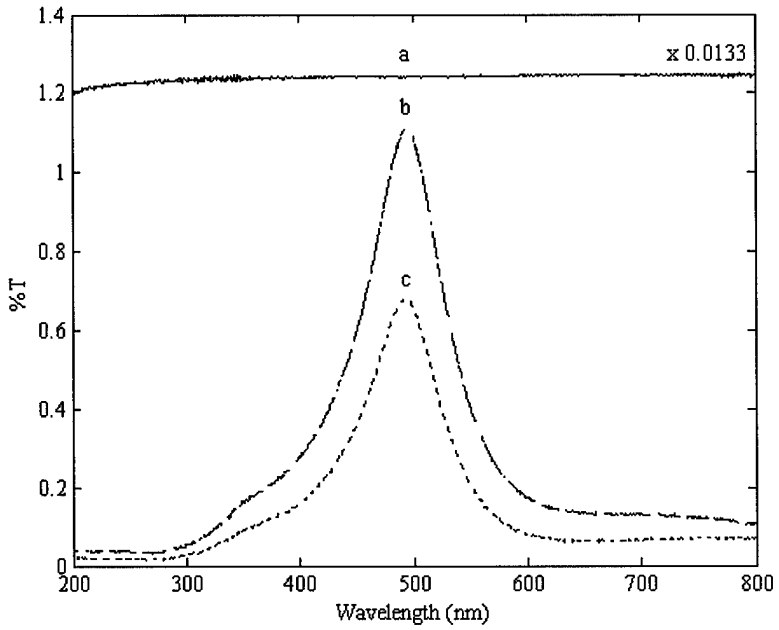

Figure 50. Transmission spectra of a) an uncoated fused-silica window (divided by 75), b) a fused-silica window coated with approximately 500 Å gold (w*indow #1*), and c) a second fused-silica window coated with approximately 500 Å gold (w*indow #2*)

The structure of the transmission spectra of both coated windows was similar, but the magnitude was different because of coating thickness. Both spectra show broad regions of weak, structured transmission between 300 and 625 nm attaining maxima near 495 nm. That window #1 transmits more than window #2 between 300 and 625 nm suggests that the gold coating on #1 is somewhat thinner than that on #2. Variability of film thickness is expected, as consistent sputtering conditions and sputtering duration are difficult to achieve. Transmission through the uncoated fused-silica disc was approximately 93% and flat over most of the wavelength range, falling slightly with wavelength below 225 nm as the window became less transparent to deepening UV radiation.

Parallel-electrode PE-ECD design

A PE-ECD featuring large-diameter parallel electrodes was constructed within an off-the-shelf vacuum stainless steel 4-way cross of nominal flange diameter 2.75 inches. The 1.75-inch diameter photoemissive window #2, gold film diameter 1.25 inches, was mounted on one arm of the cross. The window was mounted between thick Viton o-rings. The gap between the window edge and the inside edge of the retaining flange was packed with aluminum foil to keep the window in place as the o-rings were compressed. A 1.18-inch diameter copper disc soldered to a length of copper rod was mounted to a BNC feed-through on the opposite arm of the cross as the collector electrode. The collector was centered and parallel to the photoemissive surface with a separation of about 4.9 mm. A wire was glued with silver epoxy to the tab protruding from the gold film and connected to a second BNC feed-through in the third arm of the cross. The first several centimeters of the wire were sheathed in a glass tube. The fourth arm of the cross was fitted with a double-tapped, double-sided flange and capped with a fused-silica window.

Variation of oxygen anion production with bias voltage

Production of oxygen anions from laboratory air was measured as a function of bias voltage in four segments. The oxygen-anion current was measured between 0 and 103 V using a Harrison

Laboratories 881A voltage supply and the Hamamatsu L4646 xenon flashlamp operated at maximal output intensity and 25 Hz repetition rate. The image of the flashlamp discharge was centered on the photoemissive film using the same two lenses used during experimentation with the previous cell design. The cell remained open to air during the experiment. Waveforms were acquired in the direction of increasing bias voltage as 500-acquistion averages of record length 2000 points. Recently completed C++ signal acquisition software drove signal acquisition and downloaded binary waveforms from the Tektronix TDS 620A oscilloscope to the controlling computer. One horizontal scale change, from 500 μs/div to 1 ms/div at 15 V bias, and one vertical scale change, from 1 mV/div to 2 mV/div at 55 V bias, were required on the oscilloscope during waveform acquisition.

Several examples of waveforms acquired during the experiment, smoothed to reduce high-frequency noise, are plotted in Figure 51. The structure of the waveforms consists of the rapid onset of current in the external monitoring circuit that terminates as the anions reach the anode, characteristic of ion waveforms obtained from parallel-electrode detectors. Waveform duration is comparable to waveforms obtained with previous detectors at similar bias voltages. All waveforms contain a leading edge spike and some show an unexplained noise spike that occurs variably between 4.2 and 4.8 ms drift time.

Raw waveforms were integrated to calculate the total charge registered by the detection circuit at each bias voltage. Integrations included points 400 to 2000, corresponding to entire waveforms beyond the oscilloscope trigger. These results are similar overall to those observed in previous detectors equipped with photoemissive electron sources.

The oscilloscope vertical scale change might account for the irregularity at the transition between 50 and 55 V in the total charge curve.

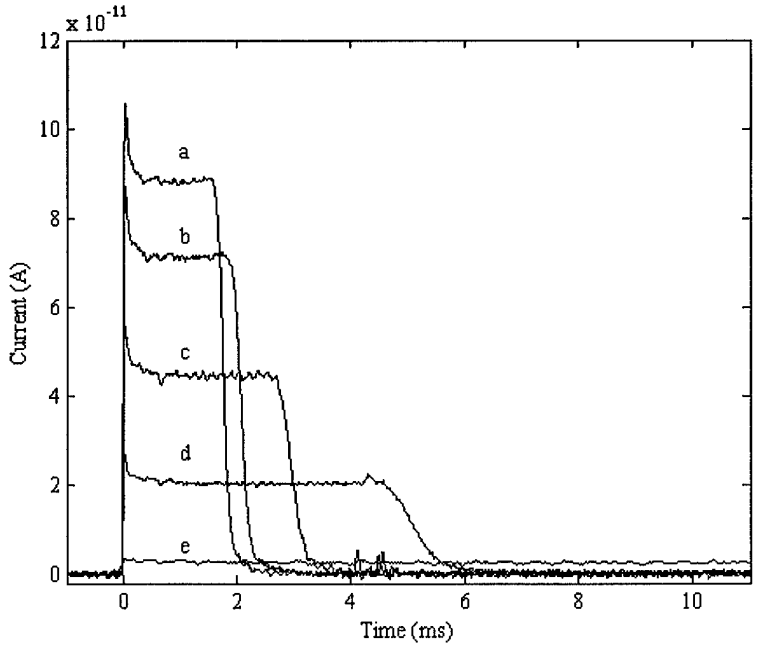

Figure 51. Detector current as a function of time at bias voltages a) 100 V, b) 85 V, c) 60 V, d) 35 V, and e) 10 V. Note that waveform *e* extends beyond the end of the time axis of the figure.

Charge registered by the detector is plotted in Figure 52 as a function of bias voltage. This shows that electron emission or oxygen anion generation increases sharply as bias voltage increases from 0 V, but then rolls over to an approximately linear increase with bias voltage. Figure 52 is very similar to curves obtained in air at atmospheric pressure during early explorations of the photoelectric effect [Schweidler and Wien, 1928].

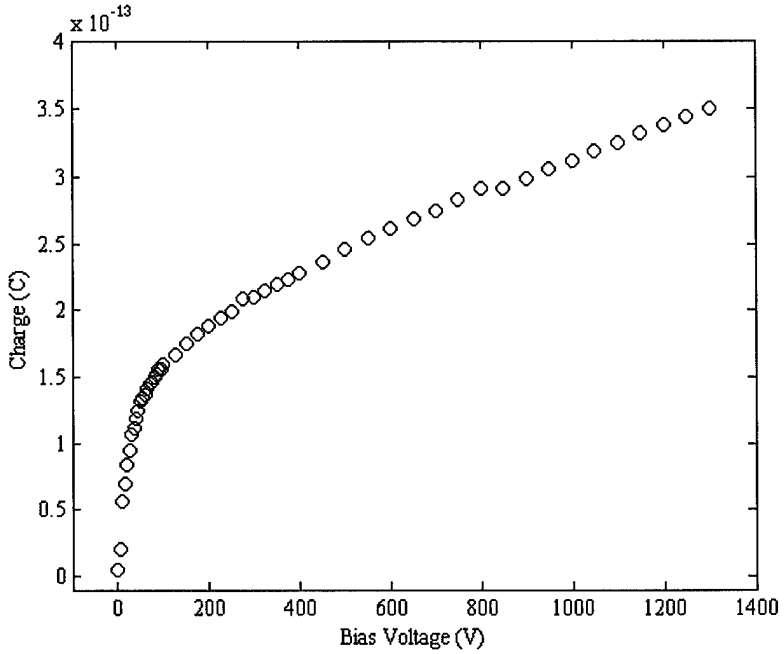

Figure 52. Charge registered by the detector as a function of bias voltage from 0 - 1750 V

The data suggest that 200 V is a useful operating bias voltage for the parallel-electrode PE-ECD. Although electron yield is roughly half that obtained at 1750 V bias, 200 V bias lies near the onset of the linearity of ion yield with bias voltage and produces an electric field of magnitude 400 V/cm, within low-field limits in both nitrogen and air at ambient pressure. Operating the detector in low-field conditions ensures that ion-drift velocities depend only on the electric field magnitude.

Wavelength effect on photoyield

Oxygen anion production was measured as a function of laser wavelength with the parallel-electrode PE-ECD. Perpendicularly polarized, frequency-tripled Ti:Sapphire laser output was passed through a Schott filter, a fused-silica microscope slide, a 30-cm negative lens, and a variable aperture to the PE-ECD. The microscope slide directed reflections of passing pulses to a fused silica window that relayed reflections to a quantum counter used to trigger the oscilloscope. Pulse diameter, expanded by the negative lens, was controlled with the variable aperture. Measurements were performed with the cell rotated 30° relative to the incident beam, creating a 30° angle of incidence with the photoemitter. This arrangement allowed reflections of pulses from the photoemissive window to be monitored by a pyroelectric detector without obstructing the incident beam. Because reflections overlapped, the indirect measure of laser energy included reflections from both the front and back faces of the photoemissive window.

Measurements were made while the cell was open to air at bias voltage 250 V and electrode separation about 4.9 mm. After three background waveforms were collected with the laser blocked, three 100-acquisition average waveforms were collected at each of several wavelengths

between 248 and 273 nm. The triplicate waveforms were averaged, and the mean background waveform was subtracted from each mean ion current waveform. Corrected waveforms were integrated to compute the total charge registered by the detector at each wavelength. Each integral was divided by the average maximum of the pyroelectric response to normalize for laser energy variations during waveform acquisition. Normalized charge and a second-order exponential fit to the charge data are plotted in Figure 53, as a function of laser wavelength. As anticipated, Figure 53 shows that oxygen anion production decreases as laser wavelength increases, or, equivalently, as photon energy declines. The data appear to include the approach to the work function of the gold photoemissive film and therefore could be used to calculate the work function through established means not undertaken here. In view of the results of such calculations, these data suggest that the work function of the film lies near 265 nm, or about 4.685 eV, in air.

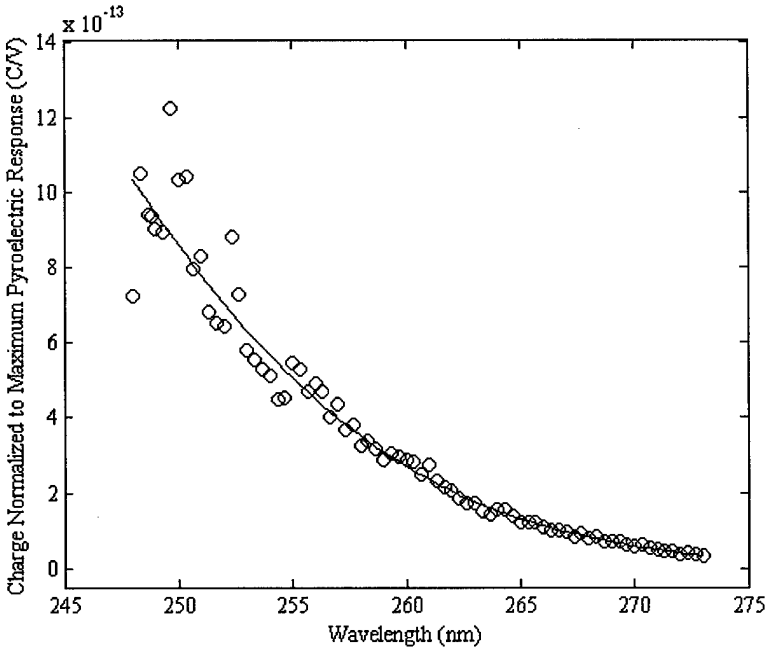

Figure 53. Charge as a function of wavelength of perpendicularly polarized UV radiation, normalized to laser energy reaching the photoemissive window. The plot shows charge data, *o*, and a second-order exponential fit to the data, *solid line*.

PE-ECD Conclusions

An initial small-volume PE-ECD cell was designed and used to demonstrate the feasibility of downhole PE-ECD detection of chlorinated species, using a xenon flashlamp as the ultraviolet source for photoelectrons. This pin-in-cup design was used to investigate flashlamp focusing, gas flow rate, and bias voltage parameters. Two techniques were used to supply varying concentrations of PCE to the PE-ECD: exponential dilution in nitrogen and a permeation tube. Both indicated similar detection limits for this design of approximately 350 ppbv by the free-electron absorption measurement and 640 ppbv by measuring the chloride anion charge.

Detection limits of 1000 ppbv by electron absorption measurements and 2050 ppbv by chloride anion charge measurements were established for TCE in nitrogen. A conditioning of the photoemitter surface by exposure to cyclohexane or PCE vapors was also found to reduce the photoemitted current by 8-9%. The emission stabilized after the conditioning and indicates that, for a gold film emitter, the detector should be "conditioned" with a non-attaching vapor such as cyclohexane before use. Further experimentation is warranted to evaluate conditioning that is

probably due to the adsorption of monolayers of hydrocarbons, or other emitter materials. The sensitivity of the pin-in-cup design was not satisfactory and a new design was developed that gave over an order of magnitude improvement.

The second design used a miniature parallel plate configuration with the gold thin film photoemitter as one plate and the smaller diameter flat end of the collection pin as the other plate. The improved design demonstrated a detection limit below 30 ppbv for PCE in nitrogen. The ultimate sensitivity was limited by our inability to deliver a lower concentration accurately to the PE-ECD. When coupled with a gas chromatograph, sensitivities of 2 ppbv PCE in P-5 carrier gas were demonstrated.

Photoemission measurements were made in three non-attaching gases that showed that, for the same conditions, free electrons were produced in the ratio 6:4.5:1 for P-5, argon, and nitrogen, respectively. Oxygen was found to have a peak attachment rate at an applied bias of 18 V in nitrogen and near 9 V in P-5.

Efficient detection of the nitroaromatic p-nitrotoluene was demonstrated in nitrogen and P-5. Due to time limitations and the concentration delivery system to the PE-ECD, a detection limit was not established. Since the nitroaromatic molecules are not expected to dissociate upon electron attachment, the oxygen interference should be avoidable by designing a counterflowing air or nitrogen drift tube similar to those used in commercial ion mobility spectrometry, the industry standard for field measurements of nitroaromatic explosives. The application of PE-EDC to this area definitely warrants further study.

Another promising application of the PE-ECD is as a very sensitive gas chromatograph detector. Coupled with a commercial GC, PCE detectability appears to lie below 2 pg/s PCE in P-5 based on the free-electron loss by electron capture. Commercial electron capture detectors attain minimum detectable levels for chlorinateds between 0.05 and 1 pg/s, depending upon molecular structure. Use of a diode-pumped microlaser as the ultraviolet source, instead of the xenon flash lamp, could likely decrease the detection limit to below current commercial limits while keeping the cost down.

Limited additional measurements were made on the effects of bias voltage and pump wavelength on photoemission efficiency. Measurements on polarization effects were also attempted but were inconclusive due to limited time. The photoelectric effect literature indicates that parametric studies of thin film thickness, thin film material, applied bias, and ultraviolet wavelength and polarization would have high payoff toward making the PE-ECD even more attractive.

APPENDIX A – HARDWARE

Halogen Specific Detector (XSD)

Design and construction

The main difference between OI Analytical's XSD [Simon et al., 1996] and our XSD is the method by which the XSD temperature is regulated. Both systems use an active feedback mechanism to control the reactor core temperature. OI Analytical's system actively regulates the temperature by monitoring the resistance of the platinum wrappings of the reactor core. It automatically regulates the current supplied to the platinum wraps accordingly. The power supply sold with the XSD allows the user to set the temperature at one of four settings (800, 900, 1000, and 1100 °C).

We could not use this active feedback mechanism because the long wires used to supply current to the XSD introduced significant error into the resistance readings. Rather, our system uses a thermocouple embedded near the reactor core to monitor temperature. The temperature outside the reactor core is somewhat lower than the temperature inside the reactor core. However, before the XSD is completely assembled, a temperature probe is placed inside the reactor core and a correlation between the inside reactor core and the outer thermocouple is found. Once this relationship has been found, the outer temperature can be used to actively control the XSD temperature. The XSD temperature is actively controlled with an Omega temperature controller and a precision power supply.

LEMO Connectors

Attaching the umbilical cable to the XSD and the XSD to the MIP initially proved challenging. Simply hardwiring the three caused twisting and pinching problems as the assembly was placed into the outer pipe. These problems were solved with the addition of LEMO® connectors at junctions between the umbilical cable, the XSD, and MIP (Figure 54). The connectors consist of two parts that snap together in a linear motion, eliminating twisting problems. Two types of LEMO connectors were used: a 16-pin version for attaching the umbilical cable to the XSD, and a 6-pin version for attaching the XSD to the MIP. Figure 55 and Table 7 show the 16-pin LEMO connector and its connections. Since several of the connections end in the XSD, fewer pins are required for the MIP. Therefore, a 6-pin version is used to attach the XSD to the MIP, as shown in Figure 56 and Table 8.

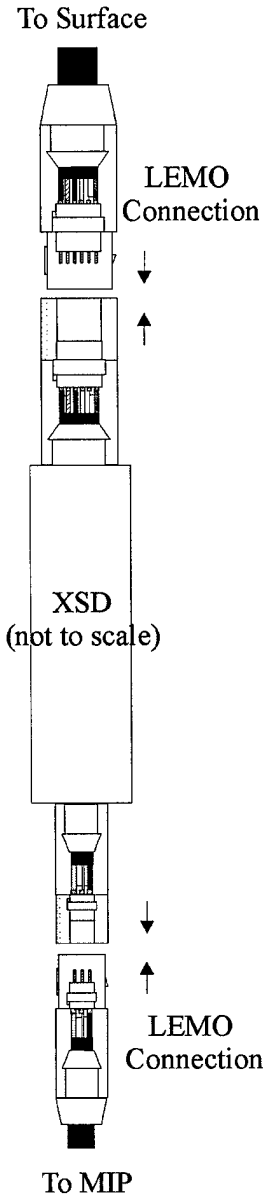

Figure 54. Schematic of XSD subassembly

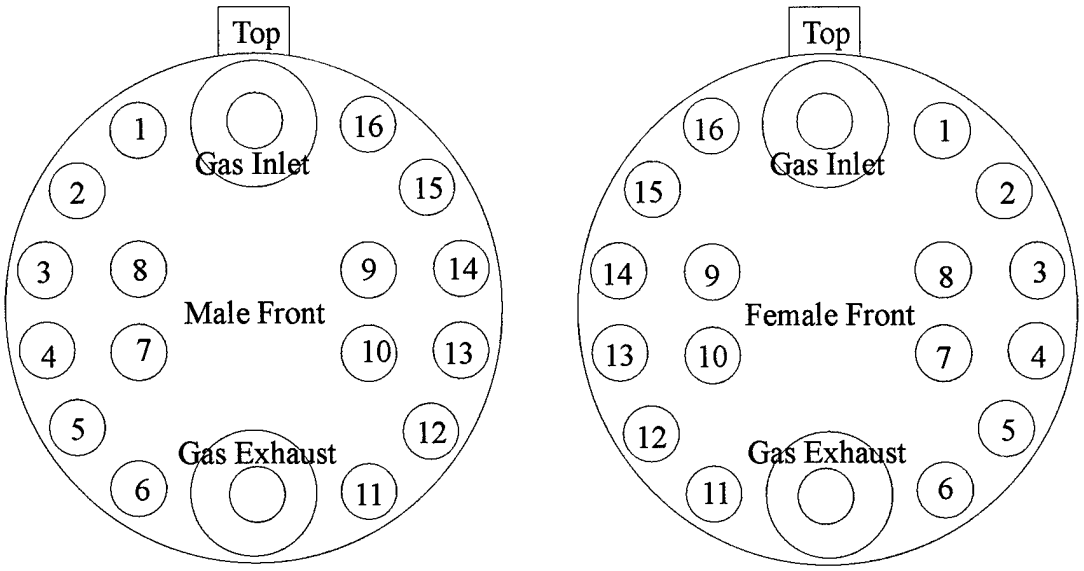

Figure 55. 16-pin LEMO connector wiring scheme attaches umbilical cable to XSD

Table 7: 16-Pin LEMO Connector Wires

Wire	Connection
1 & 6	MIP wires
3 & 4	MIP thermocouples
2, 8, 5,7	Reactor core heating wires
9	Ground
11	Signal
13 & 14	**Thermocouples**
16	Bias
10, 12, & 15	Not used

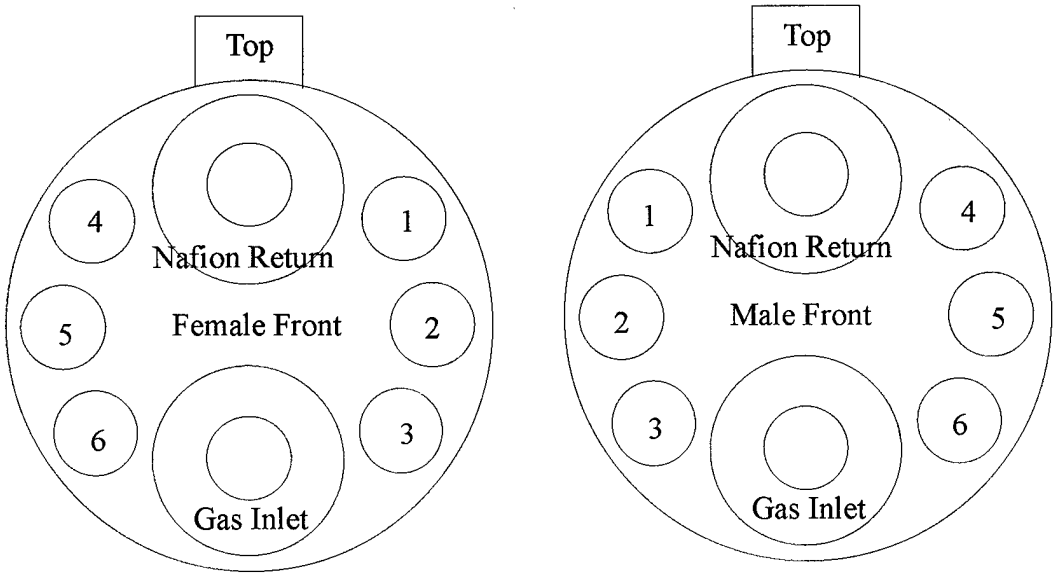

Figure 56. 6-pin LEMO connector wiring scheme attaches XSD to MIP

Table 8: 6-Pin LEMO Connector Wires

Wire	Connection
1 & 4	MIP wires
3 & 6	MIP thermocouples
2 & 5	Not used

Membrane Interface Probe (MIP)

Power supplies
The MIP power supply delivers 7 Amps at 50 VAC to the MIP. An Omega temperature controller is used to switch a solid-state relay to maintain the correct temperature for the MIP.

The XSD power supply delivers a maximum of 10±0.005 Amps at 20±0.005 VDC. Another Omega temperature controller regulates the current delivered from the power supply to the XSD via a 0-10 V analog output from the temperature controller to the power supply. This arrangement can control the temperature of the XSD to ±0.5 °C around the setpoint during a push.

Electronics
The electronics packet downhole consists simply of an RC circuit that removes any noise greater than 12 Hz. The circuit also converts the small currents generated by the XSD to a voltage, which is converted to a digital signal uphole.

The uphole electronics consist of a 12-bit A/D converter with a range of 0 to 5 Volts (0.0012 V per division). Prior to digital conversion, the voltage from the XSD is divided by 2 to give an effective range for the A/D converter of 10 volts. The signal from the A/D converter is multiplied by 2 by the software to give the correct reading.

Software
The software package that controls and collects the XSD data is multifaceted. It allows the user to control the rate at which the probe is advanced and what data is saved for each run. The software collects the MIP and XSD temperatures, the probe advancement rate, probe depth, and the XSD signal. Data are collected every second and stored in text format.

The software is organized to allow for dual displays of operator-chosen data. Most commonly, the XSD signal vs. depth is plotted on one display and the MIP temperature vs. depth is plotted on the second display. By doing this, the operator can continuously monitor the MIP temperature and slow probe advancement as necessary to keep the MIP above 100°C.

Umbilical Cable
To operate the XSD, several gas and electrical lines must be passed to the downhole sensor. An armored umbilical cable is used to protect these lines from damage while maintaining flexibility. The cable is comprised of a 100-foot length of 5/8-inch stainless steel interlocked tubing coated with polyurethane. The coating ensures that no water passes through the tubing and into the sensor.

The cable is constructed by passing a steel cable through the entire length of the steel tubing. Once this has been done, all the appropriate lines [11 electrical and 2 gas for the XSD (see Figure 57)] are bonded to one end of the steel cable. The steel cable is then drawn back through the umbilical cable until the wires have come out the other side. One end of the umbilical cable

is terminated with a LEMO connector (discussed in the next section) while the other (uphole) end is terminated with the appropriate connections for the various power supplies, temperature controllers, A/D converters, etc. Figure 57 shows the proper terminations for each line.

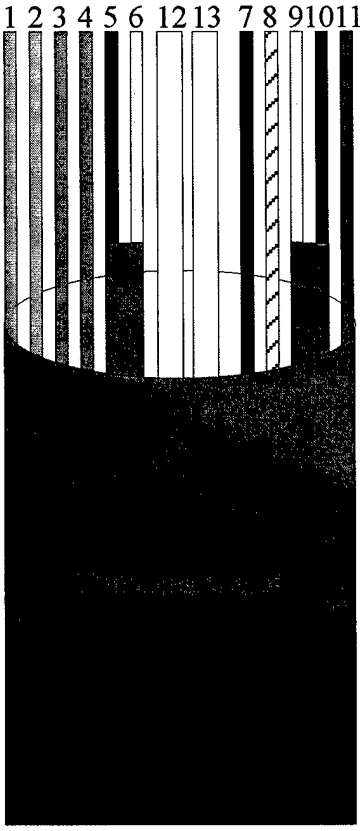

Wire	Connection
1 & 2	MIP wires
3 & 4	Reactor core heating wires
5 & 6	MIP thermocouples
7	Ground
8	Signal
9 & 10	Thermocouples
11	Bias
12	Gas inlet
13	Gas exhaust

Figure 57. Umbilical wire diagram

Water Block

Water intrusion is a constant concern with the downhole XSD sensor especially at the junction of the XSD pipe-push rod. Water entering here can flow into the XSD and destroy the assembly. We designed a water block to prevent such damage. The water block (Figure 58) consists of two stainless steel pieces that screw together and compress a rubber o-ring, making a positive seal around the polyurethane coated flexible stainless steel tubing. This seal effectively prevents water from flowing past the umbilical cable into the XSD assembly. This water block has been used on more than 20 pushes to depths of more than 40 feet with no water intrusion problems.

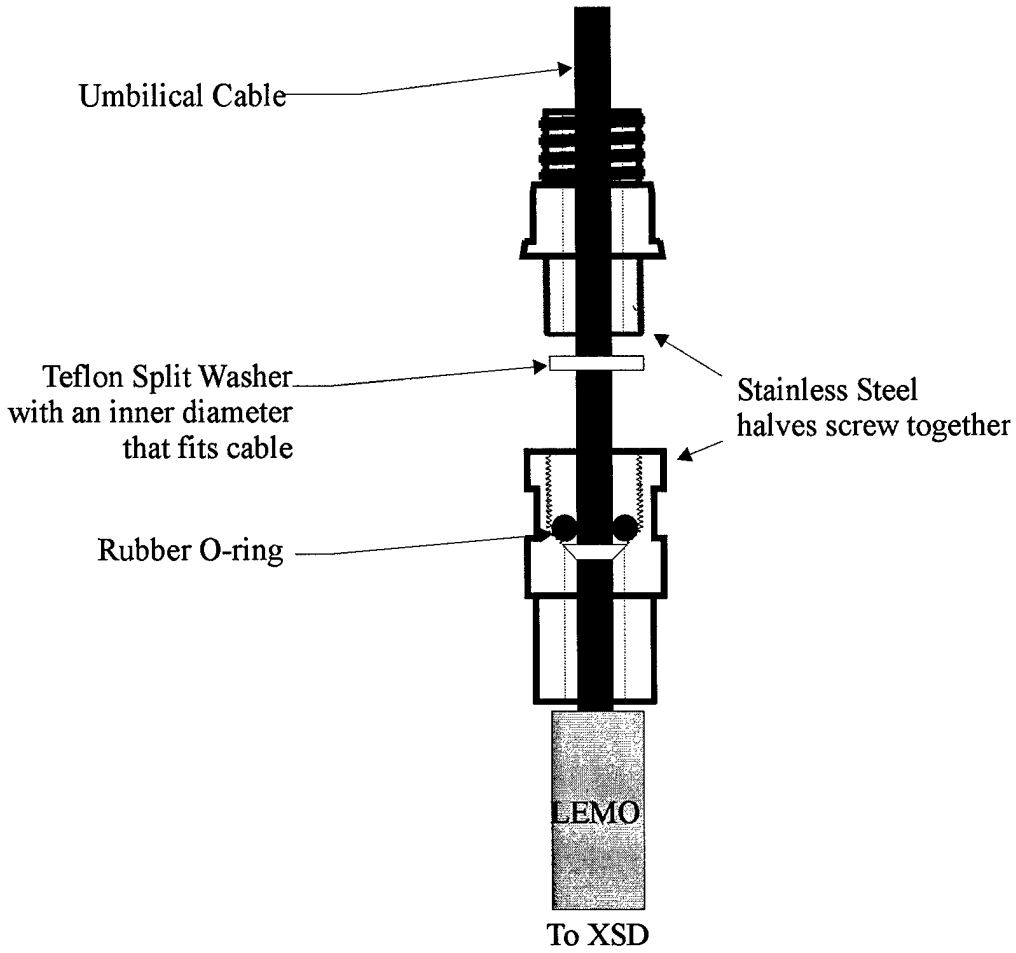

Figure 58. Schematic diagram of water block

APPENDIX B – OFFUTT DATA

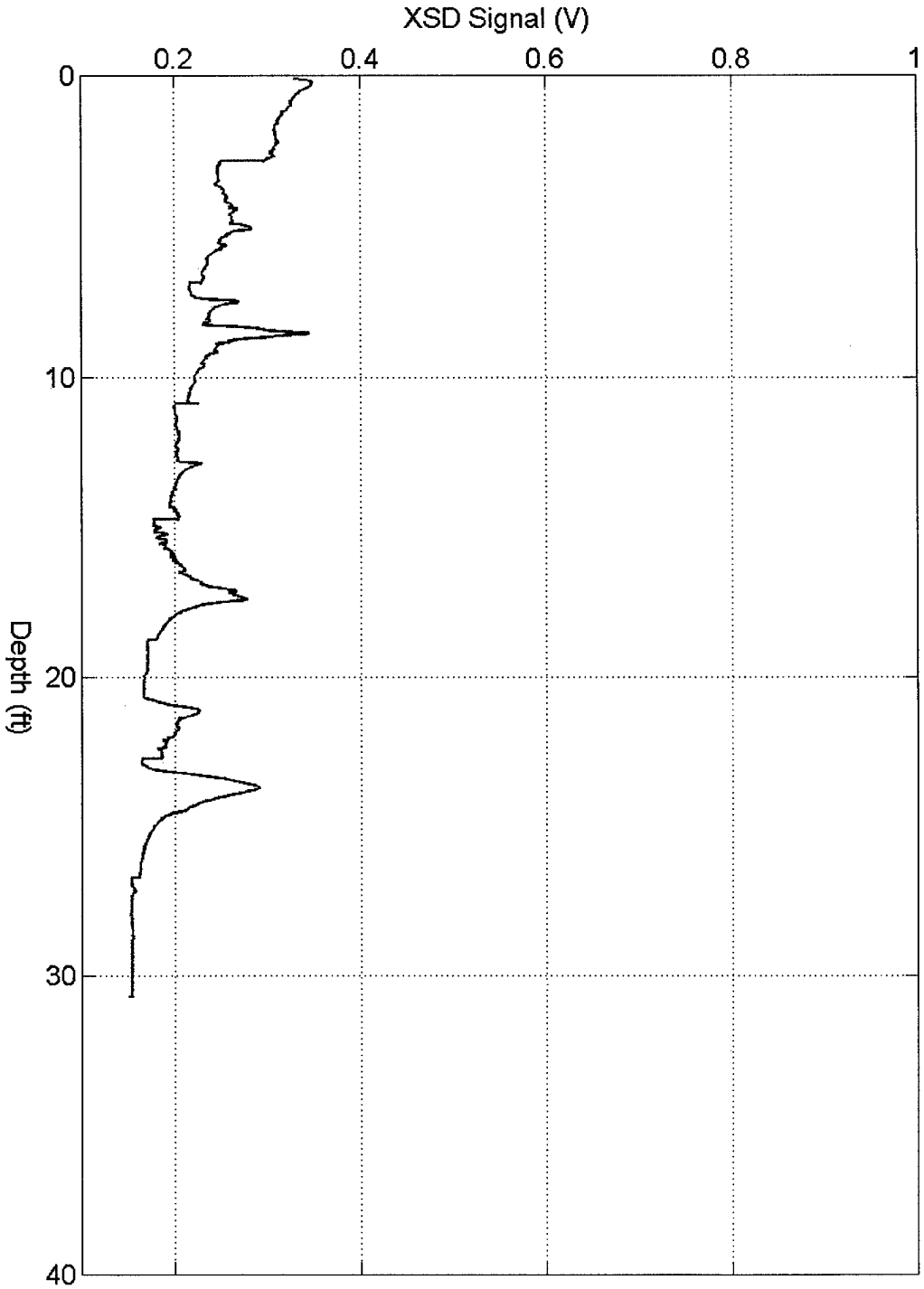

Figure 59. Push 1: Contamination areas at 9, 18, 21, and 23 feet

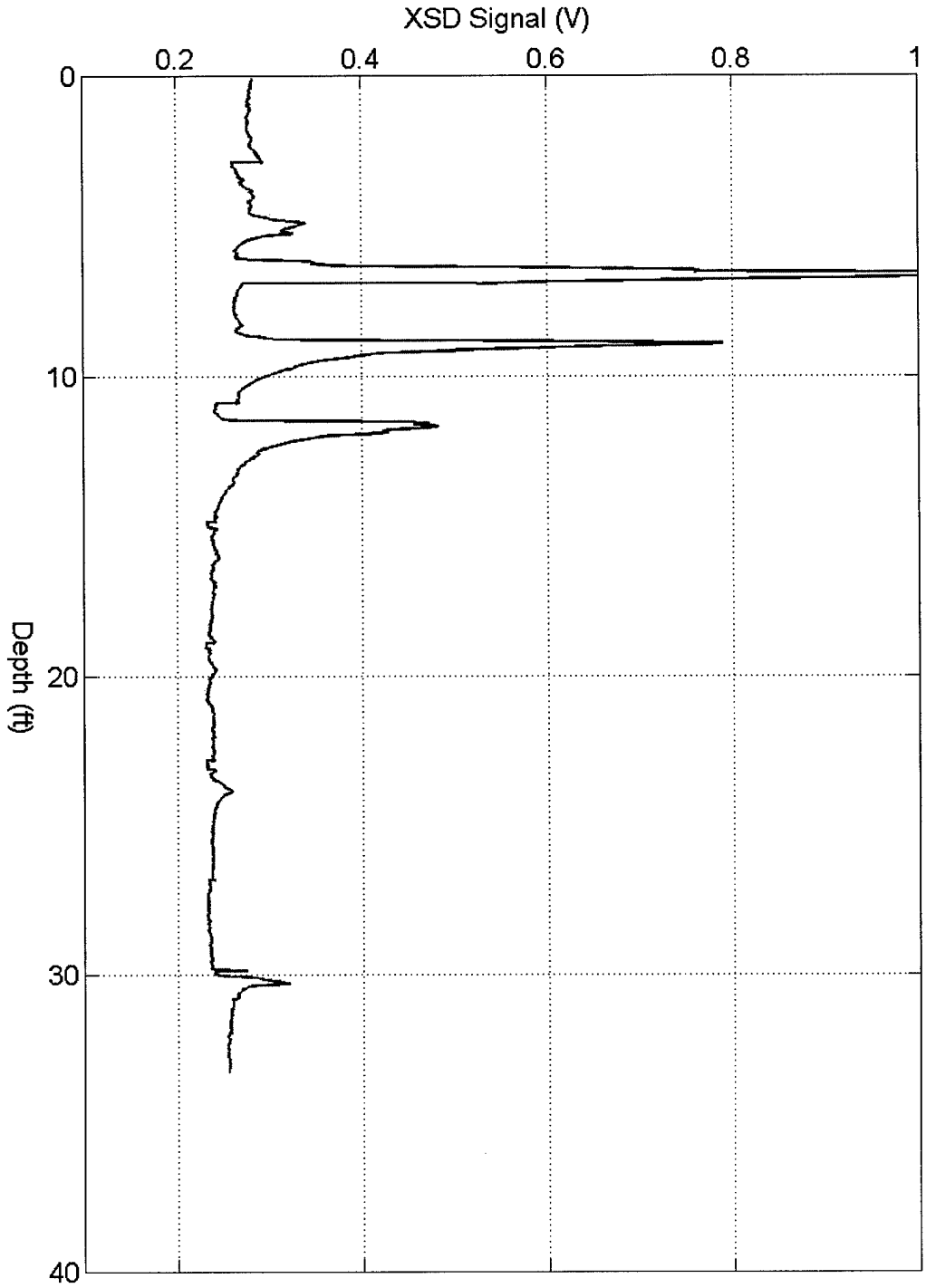

Figure 60. Push 2: Strong contamination region from 7 to 11 feet. Minor area of contamination at 30 feet

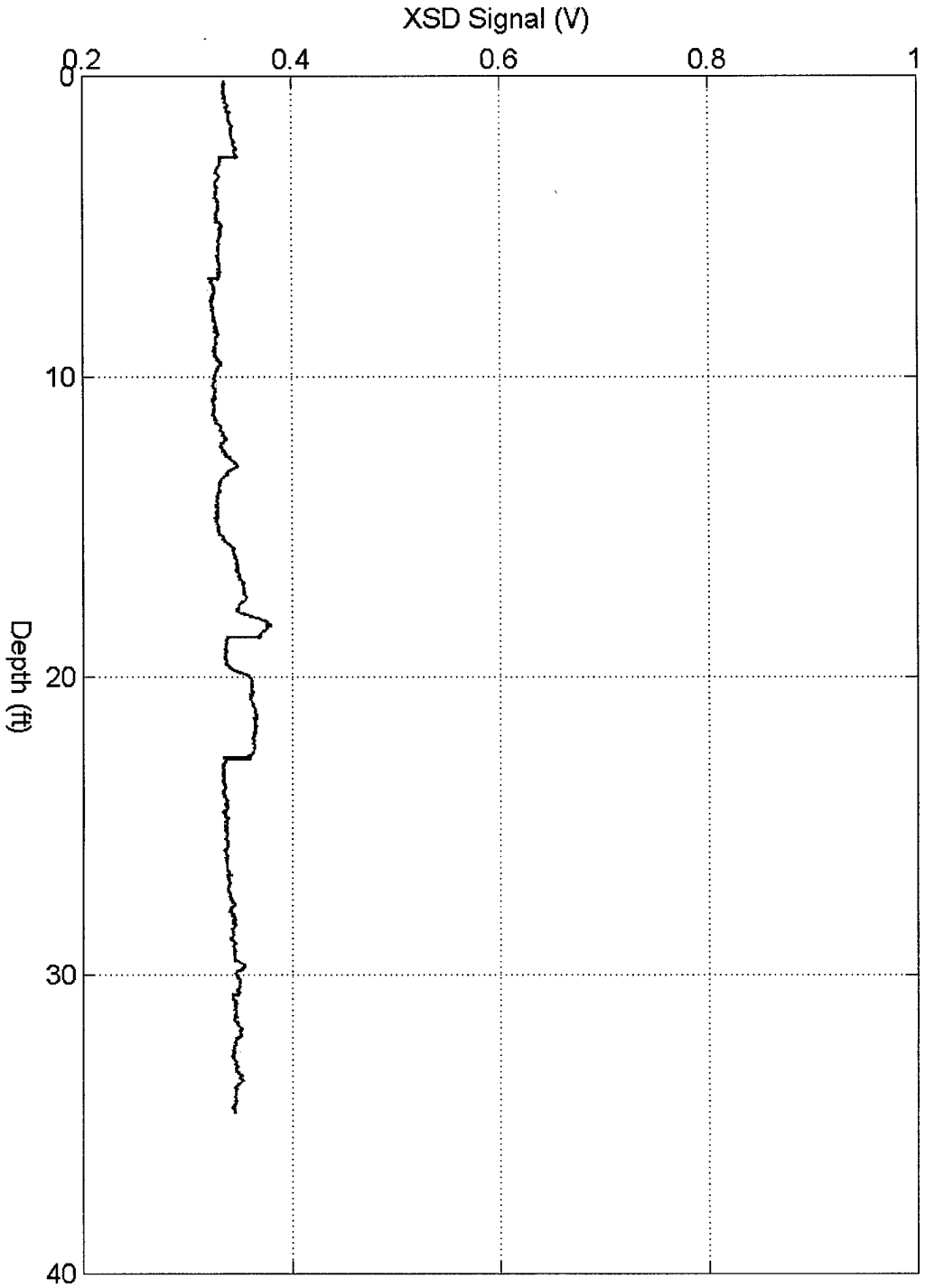

Figure 61. Push 12: Very low levels of contamination from 13 to 23 feet

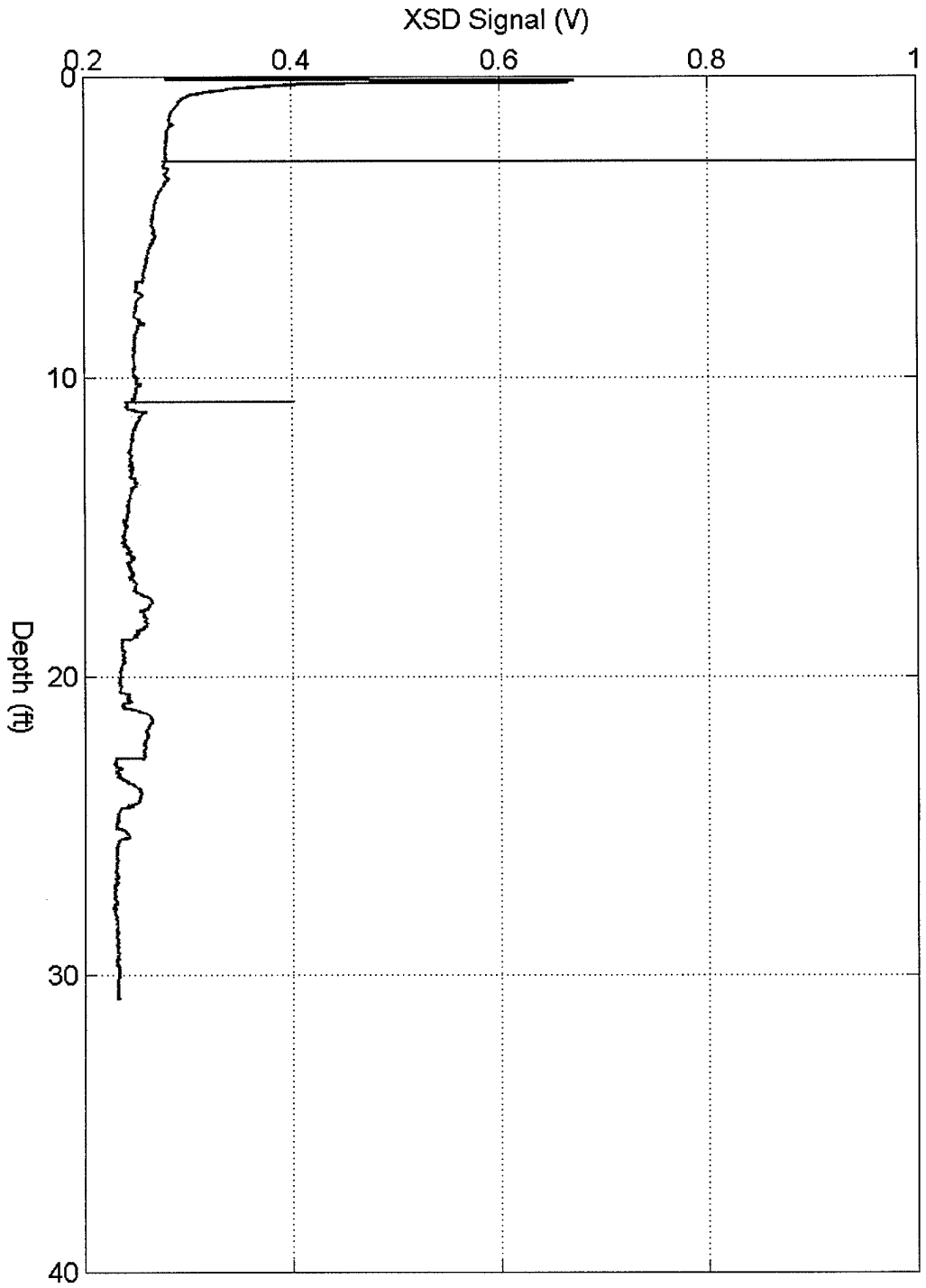

Figure 62. Push 3: Minor contamination between 16-18 feet and again between 20-25 feet. The sharp features at ground surface, 2.5 feet, and again at 11 feet are attributed to noise spikes due to residual instability of the XSD due to the accidental pounding.

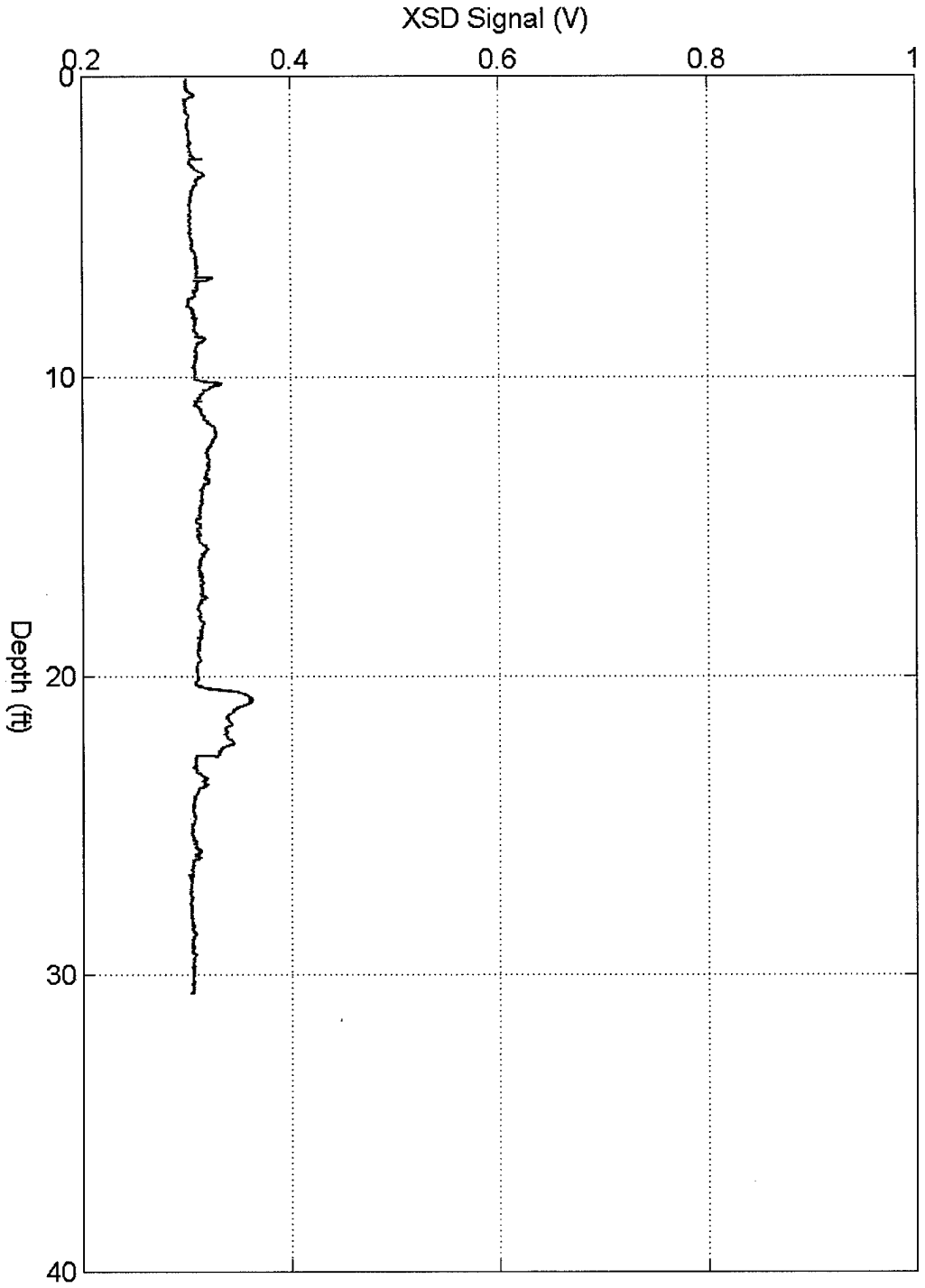

Figure 63. Push 4: Very low concentrations of contamination at 3, 10, 11, 16, & between 20-23 feet bgs.

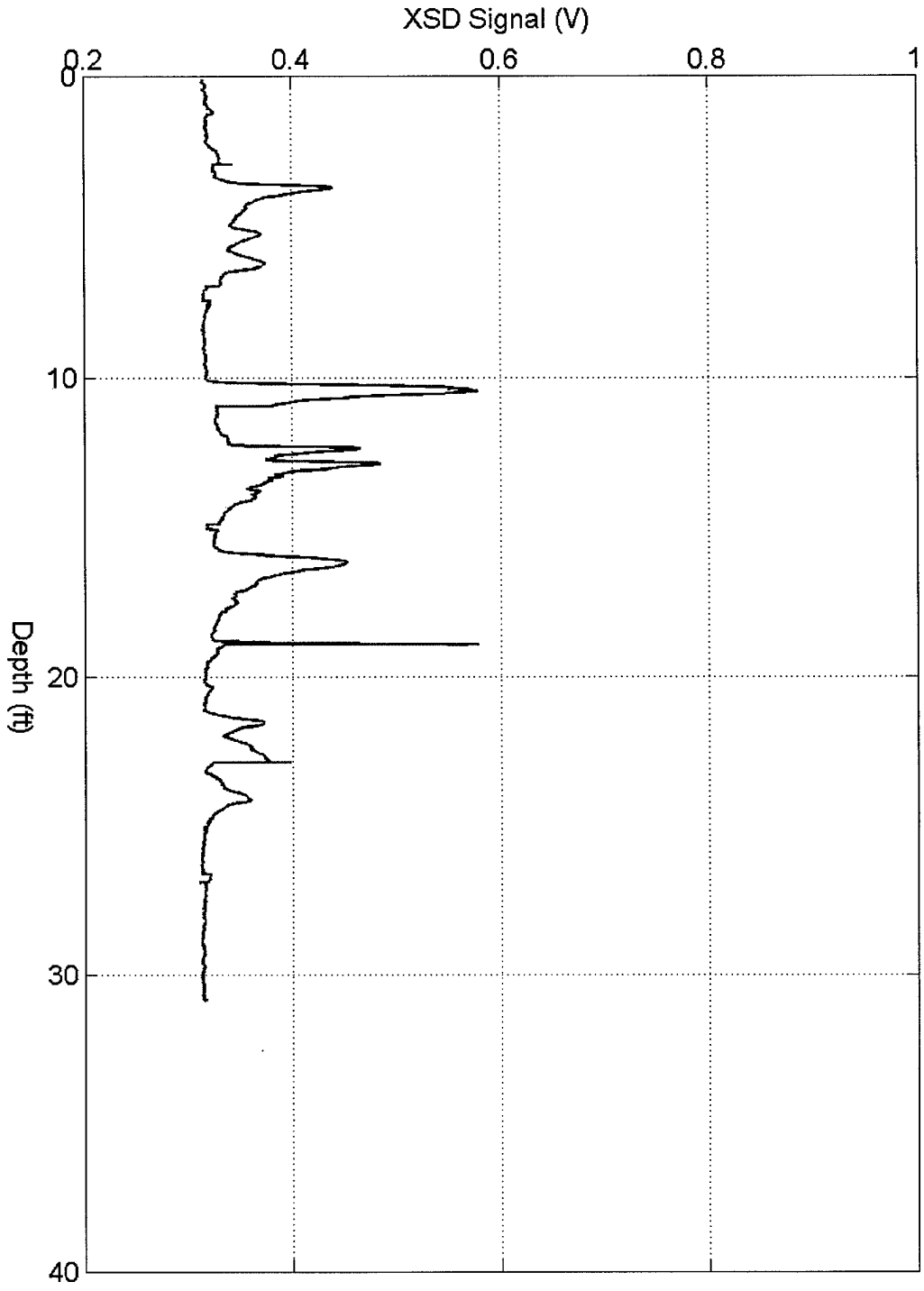

Figure 64. Push 5: Several contamination regions at 3-7, 10-11, 12-14, 16-18, 19, and 21-25 feet

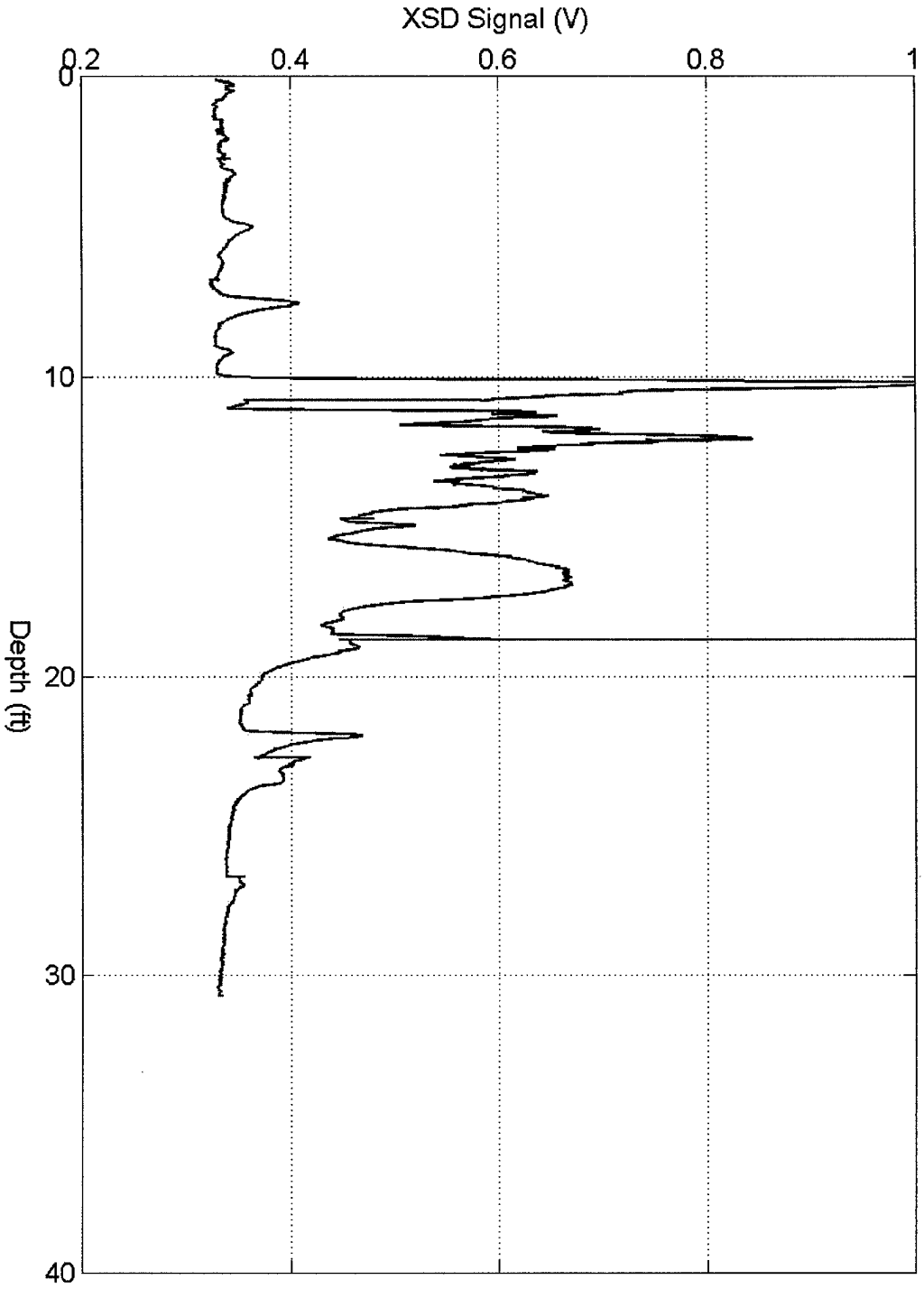

Figure 65. Push 6: The most significant contamination region lies between 10 to 20 feet bgs with smaller contamination regions at 4, 7, and between 21-23 feet

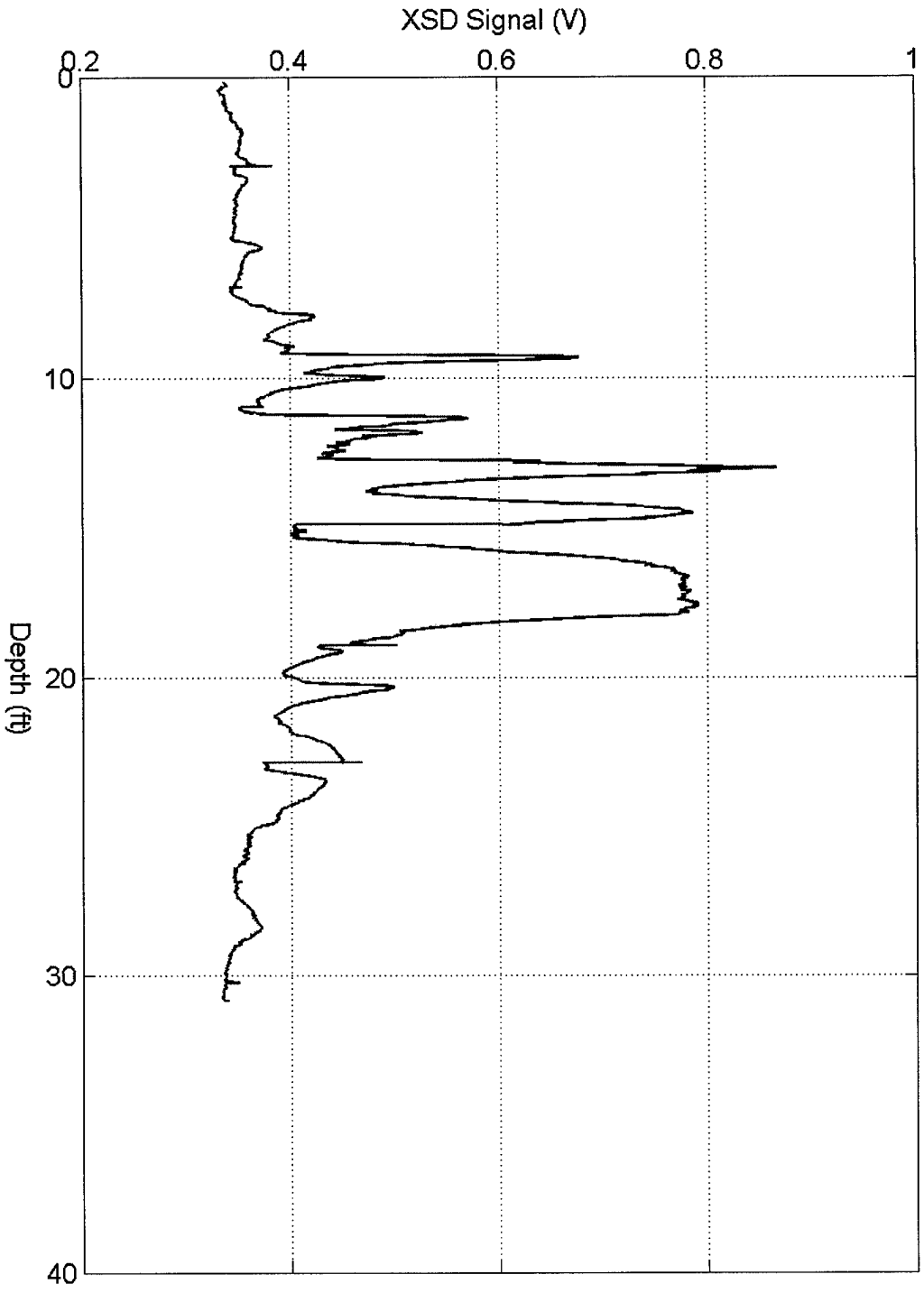

Figure 66. Push 7: Significant contamination region lies between 7 to 20 feet with smaller areas of contamination at 20 to 24 and 27 to 29 feet

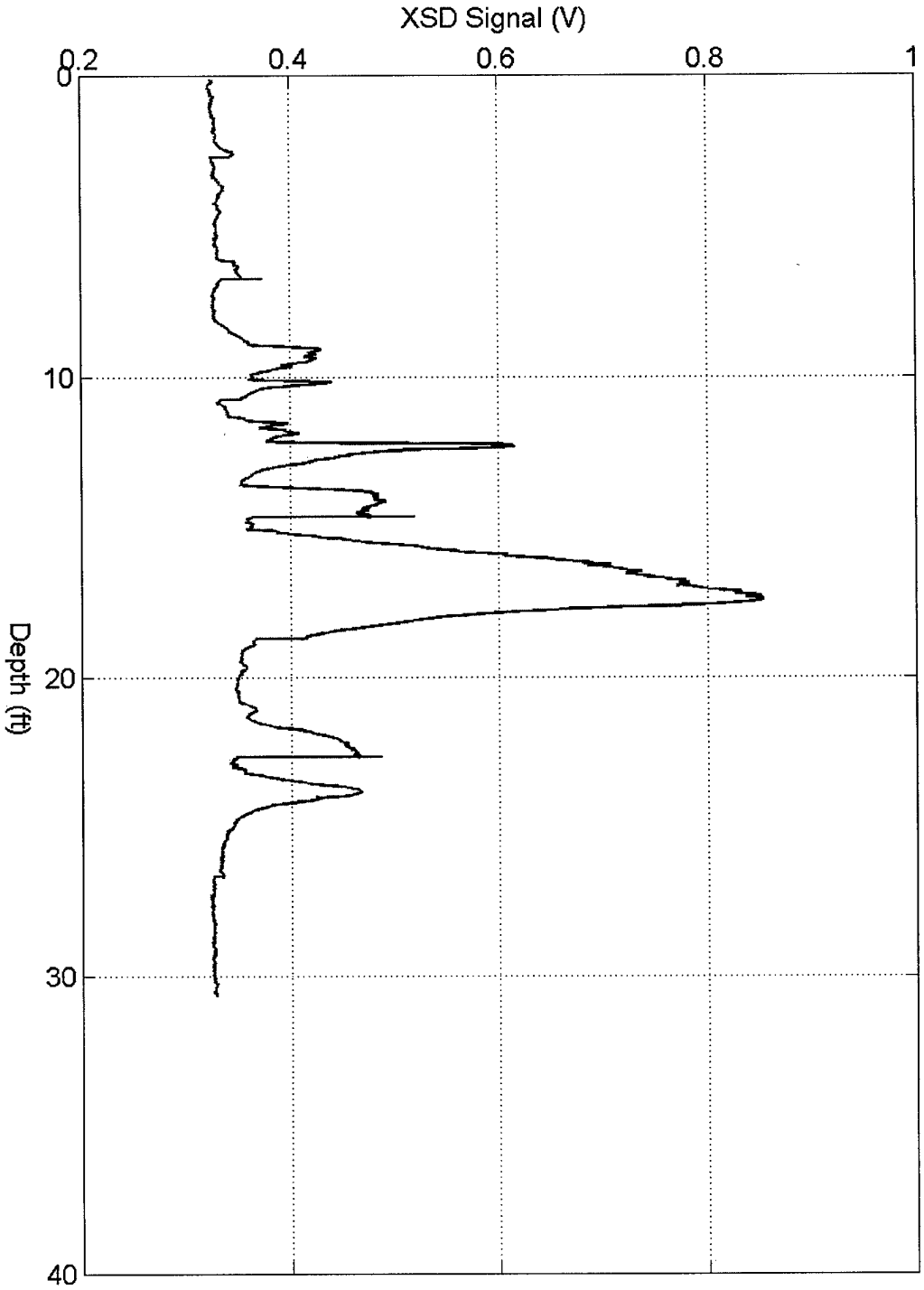

Figure 67. Push 8: Significant contamination region lies between 15 to 18 feet with smaller areas of contamination between 9 to 11, 12 to 14, and 21 to 25 feet

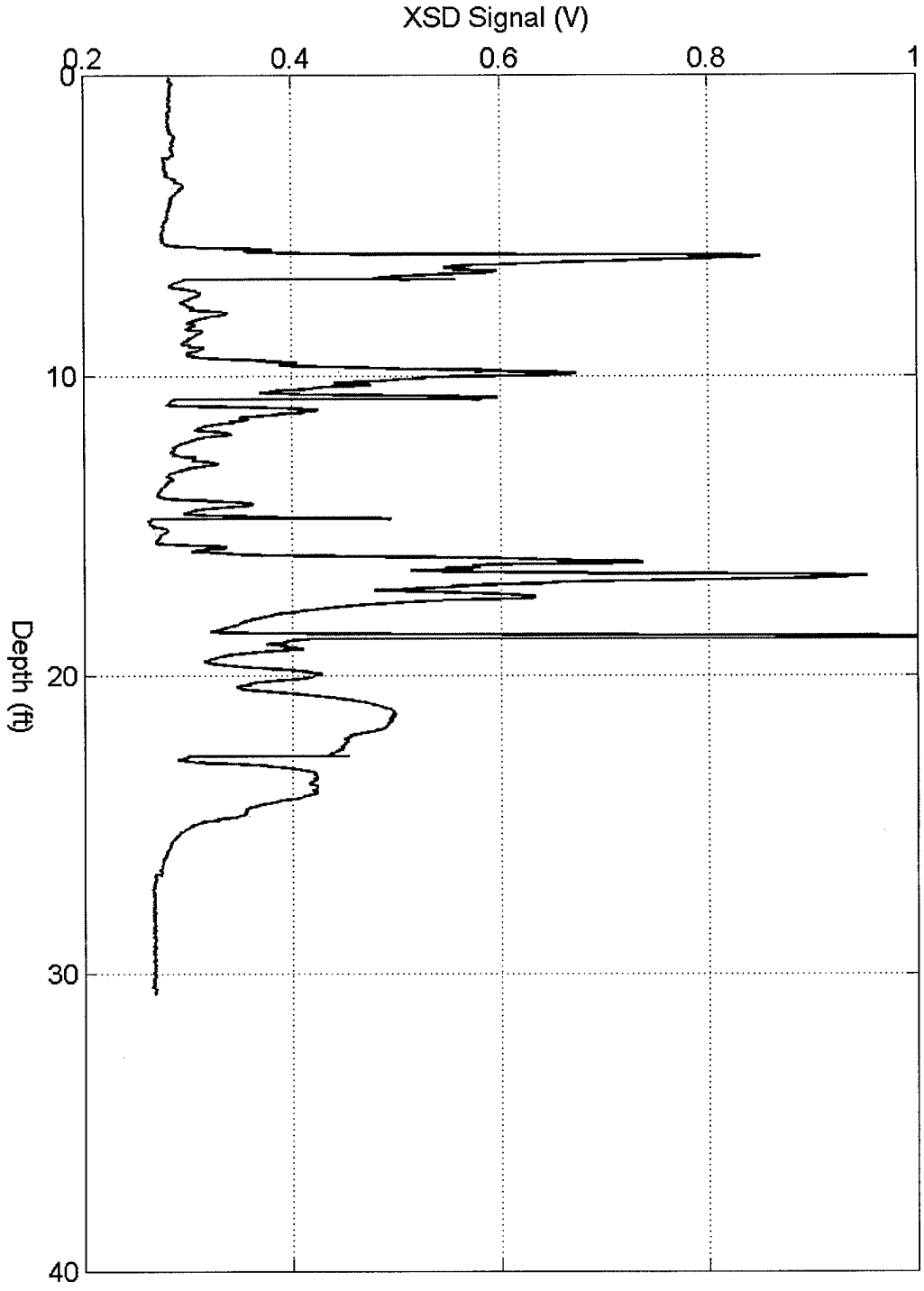

Figure 68. Push 9: Significant contamination regions lies between 6-7, 9 to12, 15.5 to 25 feet

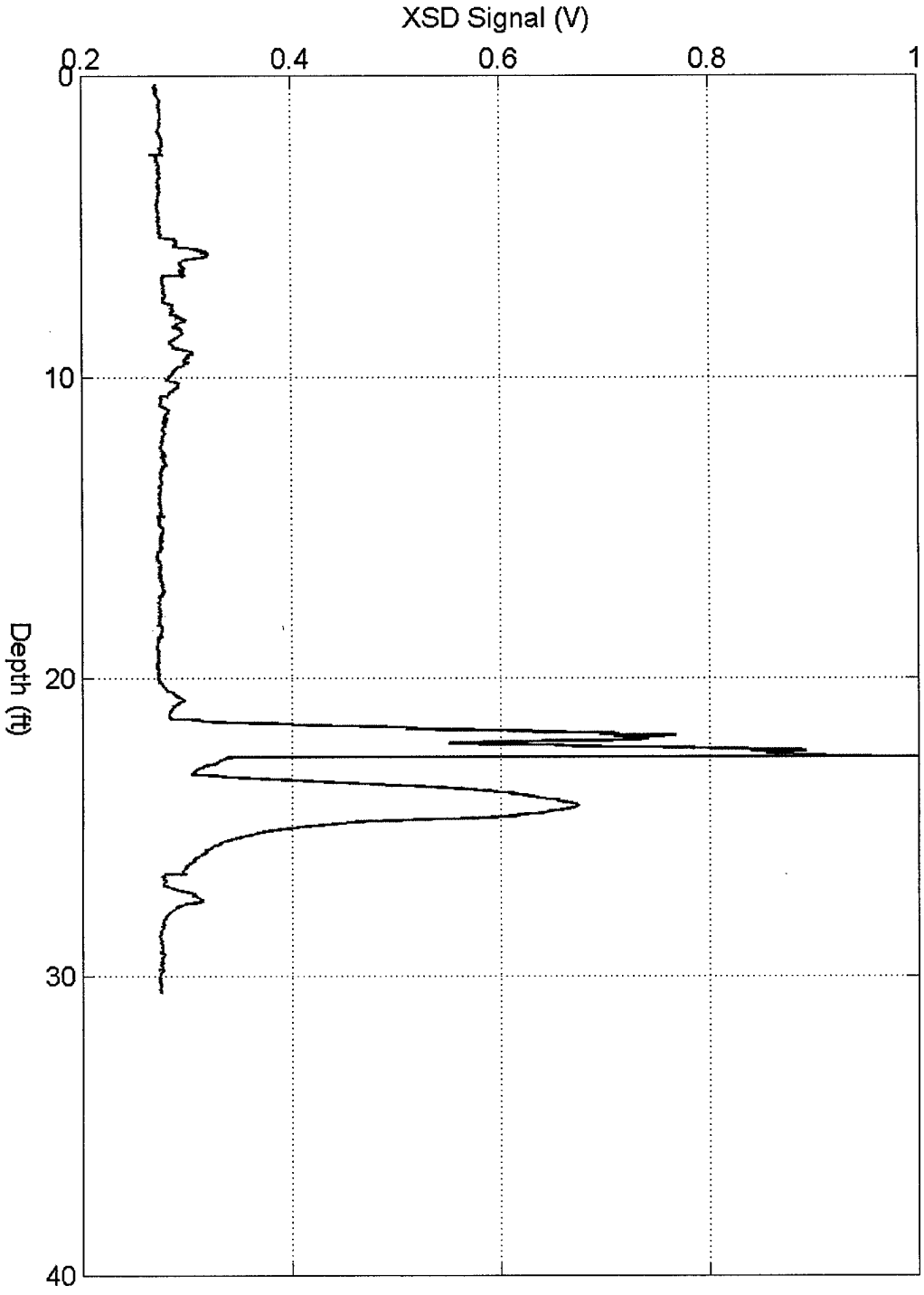

Figure 69. Push 10: Low levels of contamination between 5-10 feet. The most significant area of contamination occurred from 21 to 25 feet with another smaller area of contamination at 27 feet

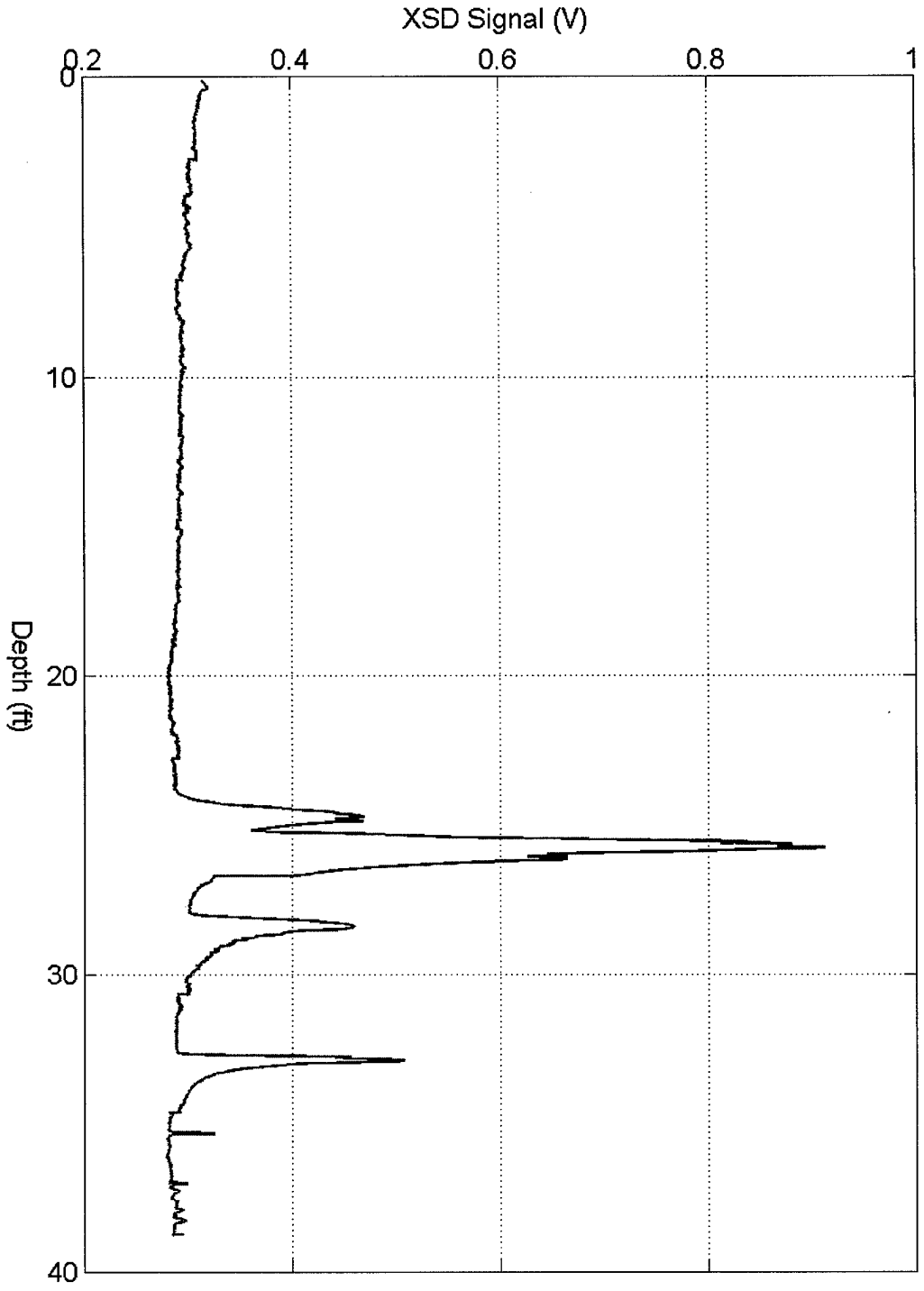

Figure 70. Push 11: Very low levels of contamination from 3 to 22 feet. However, the largest levels of contamination occurred from 24 to 30 feet with another slightly smaller area of contamination at 32 feet. This was the furthest southerly point taken

REFERENCES

Christy, T. M., "Permeable Membrane Soil Probe," U.S. Patent 5,639,956, 1997.

Feenstra, S., J. A. Cherry, and B. L. Parker, "Conceptual Models for the Behavior of Dense Non Aqueous Phase Liquids (DNAPLs) in the Subsurface." In: *Dense Chlorinated Solvents and other DNAPLs in Groundwater: History, Behavior, and Remediation*, Waterloo Press, 1996.

Fountain, J, "Surfactants and Cosolvents for DNAPL Remediation", Partners in Environmental Technology Technical Symposium & Workshop, Arlington, Virginia, 1998.

Hewitt, A. D., J. F. Jenkins, and C. L. Grant, "Collection, handling, and storage: Keys to improved data quality for volatile organic compounds in soil," *American Environmental Laboratory*, pp. 25-28, 1995.

Pankow, J. F. and J. A. Cherry, "Dense Chlorinated Solvents and other DNAPLs in Groundwater: History, Behavior, and Remediation," Waterloo Press, 1996.

Schwille, F; (Translated by J. F. Pankow), "Dense Chlorinated Solvents in Porous and Fracture Media," Lewis Publishers, 1998.

Simon, R. K.; M. L. Duffy, M. J. Tanner, M. N. Barringer, and N. C. Rawls, "Tandem Photoionization Detector and Halogen Specific Detector," U.S. Patent 5,578,271, 1996.

Schweidler, E. *Wien. Ber.* **108**, 273, 1899, as cited in Thomson, J.J and Thomson, G.P., "Conduction of Electricity through Gases, Vol. 1: General Properties of Ions; Ionisation by Heat and Light," Cambridge University Press, 1928.